Implications of dark matter free streaming in the early Universe

Diamanti, R.

IMPLICATIONS OF DARK MATTER FREE STREAMING IN THE EARLY UNIVERSE

Roberta Diamanti

Implications of dark matter free streaming in the early Universe

This work has been accomplished at the Gravity and AstroParticle Physics in Amsterdam (GRAPPA) center of excellence and the Institute for Theoretical Physics (ITFA) of the University of Amsterdam (UvA).

Printed by: Ridderprint BV — www.ridderprint.nl
Cover layout by: Ridderprint BV — www.ridderprint.nl
Cover: Galaxy and Cyclist pass in Autumn Forest. Courtesy of Camilo Sandoval. Pixabay.

Implications of dark matter free streaming in the early Universe

Academisch Proefschrift

ter verkrijging van de graad van doctor

aan de Universiteit van Amsterdam

op gezag van de Rector Magnificus

prof. dr. ir. K.I.J. Maex

ten overstaan van een door het College voor Promoties

ingestelde commissie,

in het openbaar te verdedigen in de Agnietenkapel

op dinsdag 6 juni 2017, te 12.00 uur

door

Roberta Diamanti

geboren te Rome, Italië

Promotiecommissie

Promotor

prof. dr. J. de Boer	Universiteit van Amsterdam

Co-Promotores

dr. S. Ando	Universiteit van Amsterdam

Overige leden

dr. C. Weniger	Universiteit van Amsterdam
dr. O. Mena Requejo	IFIC Instituut van Valencia
prof. P. Ullio	SISSA Instituut van Trieste
prof. dr. M.P. Decowski	Universiteit van Amsterdam
prof. dr. E. Laenen	Universiteit van Amsterdam

Faculteit der Natuurwetenschappen, Wiskunde en Informatica

Publications

This thesis is based on the following publications:

[1] *Cold dark matter plus not-so-clumpy dark relics*
R. Diamanti, S. Ando, S. Gariazzo, O. Mena, C. Weniger
Submitted to JCAP, (January, 2017)
`arXiv:1701.03128`.
Presented in Chapter **3**.

All authors participated in the planning of the project. RD, SG and CW focused on the part of the analysis code. The likelihood code to constrain the number of dwarf spheroidal satellite galaxies was written by RD under the supervision of SA. RD, CW and SG were responsible of the `MultiNest`/`MontePython` *codes, numerical simulations and analyses. All authors contributed to the writing of the paper.*

[2] *Dark matter protohalos in a nine parameter MSSM and implications for direct and indirect detection*
R. Diamanti, S. Ando, M.E. Cabrera
Phys. Rev. D **92**, (Feb., 2015), 065029
`arXiv:1506.01529`.

Presented in Chapter **4**.

All authors participated in the planning of the project. MEC focused both on the direct detection and colliders parts of the analysis code. RD focused on the indirect detection section. MEC and RD were responsible of the `MultiNest` *codes, numerical simulations and analyses. All authors contributed to the writing of the paper.*

Other publications by the author:

[3] *Constraining Dark Matter Late-Time Energy Injection: Decays and P-Wave Annihilations*
R. Diamanti, L. Lopez-Honorez, O. Mena, S. Palomares-Ruiz, A.C. Vincent
JCAP (Oct., 2013)
`arXiv:1308.2578`.

All authors participated in the planning of the project. RD contributed to the analysis codes.

[4] *Dark Radiation and interacting scenarios*
R. Diamanti, E. Giusarma, O. Mena, M. Archidiacono, A. Melchiorri
Phys. Review D **92** (Dec., 2012)
`arXiv:1212.6007`.

All authors participated in the planning of the project. RD contributed to the implementation of the `CAMB` *code and writing of the paper.*

Contents

Preface

In this thesis, we link astrophysics and particle physics aspects in order to study the implications of the nature and properties of different types of dark matter candidates on the observable Universe. The main goal is to understand, depending on the properties of some dark matter particle candidates, different characteristics of the history of structure formation in the Universe. From one side, the structures on large scales are rather insensitive to the nature of the dark matter particles while, on the other side, the sub-galactic scales strongly depend on the microphysics involving the dark matter species. The main property which connects the works on which this manuscript is based is *free-streaming*. This is the phenomenon for which the dark matter particles can *free-stream*, that is propagate out of density perturbations, depending on their nature. As a consequence, we see this effect on the observable Universe through the suppression of the matter power spectrum at scales smaller than a characteristic free-streaming length. This phenomenon is related to the so called *small-scale crisis* of the standard cosmological model in which the prediction of gravitationally bound structures of dark matter seems to be lower both in their mass and in their number, with respect to those computed in numerical simulations based on the same model. Free-streaming is also highly relevant for the first gravitationally bound dark matter structures: after the dark matter particles end to oscillate with the rest of the thermal bath, finally, they decouple kinetically, and this sets the size of those first structures. The free-streaming leads to a cold dark matter (CDM) power spectrum with a cutoff around a scale which is of the order of the Earth mass, namely $10^{-6} M_{\odot}$.

First, in Chapter 1, we give a condensed description of our present understanding of the Universe. Out of a very simple picture – as a whole, the Universe that can be observed looks the same anywhere and in every direction –, and a surprising property – it is expanding, "everything" is speeding away from us –, an elaborate account of its past history and current characteristics can be developed and tested. Starting with the basic equations that govern its evolution, we travel in time visiting the consecutive epochs in which the evolution of the Universe was ruled by radiation, then matter

and finally dark energy. Milestones like baryogenesis, the annihilation of electrons and positrons, the primordial synthesis of nuclei, the emission of the Cosmic Microwave Background or the formation of gravitationally bound structures, guide our way.

In Chapter 2, we continue to give an overview of our Universe but focusing our attention on the dark matter. We firstly explore some of the most popular particle physics candidates for dark matter. To address where and how dark matter *is*, we present the properties of dark matter halos. Finally, we describe the three different dark matter detection methods: direct detection of the energy recoil of nuclei scattering off DM particles; indirect detection of the final stable products of DM annihilation or decay, as for example gamma rays; and colliders which aim to reproduce new particles beyond the Standard Model, in particular at the Large Hadron Collider (LHC) at CERN (the European Laboratory for Particle Physics).

Chapter 3 is based on [1], and deals with a phenomenological study of a mixed dark matter model, where dark matter consists of a standard cold fraction plus a fraction given by another component non-cold. By varying both the mass and the fraction of the non-cold dark matter candidate in a sufficiently wide range, we cover a considerable parameter space, allowing us to explore, in one time, consequences of more than a single particle physics model. By using the most recent data from the Planck satellite on the Cosmic Microwave Background (CMB), the Baryonic Acoustic Oscillations (BAO) measurements, and deriving constraints from the number of dwarf spheroidal satellite galaxies in the Milky Way, we set bounds on the fraction of the non-cold dark matter component with respect to the total dark matter, as a function of its mass.

In Chapter 4, based on [2], we present a forecast on the mass of the first and smallest dark matter bound systems – commonly referred to as *protohalos* – within a supersymmetric model realized with 9 independent parameters. In this scenario, we explore a cold dark matter power spectrum with a cutoff around a scale much smaller than the reference minimum mass of $10^{-6} M_{\odot}$ estimated for supersymmetric dark matter scenarios. We first analyse the kinetic decoupling temperature and the resulting protohalo masses, which set the power spectrum cutoff. Then, we study correlations among the temperature of kinetic decoupling and direct detection signatures of dark matter, such as the spin-dependent and the spin-independent cross-sections. We address the implications for indirect detection and the search of dark matter at colliders. We find that, depending on the nature of the lightest supersymmetric dark matter particle (the lightest neutralino), the values of annihilation cross sections and protohalo masses can change significantly. We also cover scenarios where neutralinos co-annihilate with other supersymmetric particles, and that could be potentially tested by the Large Hadron Collider. We perform this work in the light of recent data coming from particle physics experiments and relic density constraints.

Acronyms

- **CMB**: Cosmic Microwave Background
- **FLRW**: Friedmann-Lemaître-Robertson-Walker
- **DM**: Dark Matter
- **CDM**: Cold Dark Matter
- **WIMPs**: Weakly Interacting Massive Particles
- **BAU**: Baryon Asymmetry of the Universe
- **CP**: Charge conjugation combined with Parity
- **LSS**: Last Scattering Surface
- **FIRAS**: Far Infrared Absolute Spectrophotometer
- **COBE**: Cosmic Background Explorer
- **IGM**: Intergalactic Medium
- **SN Ia**: Supernovae Type Ia
- **DE**: Dark Energy
- **BAO**: Baryonic Acoustic Oscillations
- **SDSS**: Sloan Digital Sky Survey
- **2dFGRS**: Six-Degree Field Galaxy Survey
- **QCD**: Quantum Chromodynamics
- **SM**: Standard Model
- **SUSY**: Supersymmetry

- **MSSM**: Minimal Supersymmetric Standard Model
- **LSP**: Lightest Supersymmetric Particle
- **ΛCDM**: Lambda Cold Dark Matter
- **NFW**: Navarro, Frenk, White
- **PS**: Press and Schechter
- **LHC**: Large Hadron Collider
- **SI**: Spin Independent
- **SD**: Spin Dependent
- **MDM**: Mixed Dark Matter
- **PDF**: Probability Density Function
- **ACT**: Atacama Cosmology Telescope
- **SPT**: South Pole Telescope
- **ESA**: European Space Agency
- **MGS**: Main Galaxy Sample
- **BOSS**: Baryon Oscillation Spectroscopic Survey
- **EPS**: Extended Press and Schechter
- **MCMC**: Markov Chains Monte Carlo
- **GUT**: Grand Unification Theory
- **RGE**: Renormalization Group Equations
- **EWSB**: Electroweak Symmetry Breaking
- **pMSSM**: Phenomenological Minimal Supersymmetric Standard Model
- **LUX**: Large Underground Xenon
- **LZ**: LUX-Zeppelin
- **CMSSM**: Constrained Supersymmetric extension of the Standard Model

1 Introduction

The ultimate physical system that we can dream of describing scientifically is the Universe itself. Cosmology addresses the study of its origin, evolution and structure. Cosmology is a field in constant and fast progress, owing to the improvement in the available observational techniques of the last decades. The discovery of the recession of galaxies – supporting the idea of an expanding Universe –, the discovery of the Cosmic Microwave Background radiation, understanding the synthesis and the resulting abundances of the light elements, understanding the formation of bound structures, all add up to prove that the standard model of Big Bang Cosmology provides indeed a good description of the Universe in which we live. This Chapter is devoted to that account.

1.1 The expansion of the Universe

Our present understanding of the Universe, Big Bang cosmology, rests on two central ideas:

- the evidence that on large scales it is homogeneous,
- the fact that it is expanding.

The idea that the Universe is smooth on large scales is both powerful and simple, since it condenses two important properties: homogeneity and isotropy. Indeed the place we occupy in the Universe is in no way special. This is known as the *Cosmological Principle*. Homogeneity means that the Universe looks the same at each point

while isotropy means that it looks the same in all directions. Cosmological observations, such as the Cosmic Microwave Background (CMB), sustain the validity of the Cosmological Principle.

The second key ingredient is the fact that the Universe is expanding. The evidence is based on the observation that almost everything in the Universe appears to be moving away from us, and further away something is, faster its recession appears to be. Velocities are measured via the *redshift*, which is basically the Doppler effect applied to light waves. Galaxies have a set of absorption and emission lines identifiable in their spectra, whose characteristic frequencies are well known. If a galaxy is receding from us, the characteristic lines move towards the red end of the spectrum, and the effect is known as a *redshift*. On the other hand, if a galaxy is moving towards us, the lines we observe are shifted towards higher frequencies, and this effect is known as *blueshift*. In the late 1920's, one of the most famous cosmologists, Edwin Hubble, observed that the spectral lines of the chemical elements in the galaxies were shifted from their normal positions towards the red part of the electromagnetic spectrum, [5] (that is towards lower frequencies with respect to those obtained in the laboratory). This is expressed in terms of a parameter z defined by[1]:

$$z = \frac{\lambda_{obs} - \lambda_{em}}{\lambda_{em}}\,, \tag{1.1}$$

where λ_{em} and λ_{obs} are the wavelengths of light at the points of emission (the galaxy) and observation (us). He concluded, for small redshift, that the velocity of recession was proportional to the distance to the galaxy, according to the linear relation between the redshift z and the distance D:

$$z = H_0\, D\,, \tag{1.2}$$

known as *Hubble's law*. The proportionality constant H_0 is known as *Hubble's constant*, usually rewritten

$$H_0 = 100\, h\, \mathrm{Km\,s^{-1}\,Mpc^{-1}}\,, \tag{1.3}$$

where h is the dimensionless reduced Hubble constant. The best recent measurements of the Hubble parameter H_0 given by the Planck temperature data combined with Planck lensing [6] is:

$$H_0 = 67.8 \pm 0.9\, \mathrm{Km\,s^{-1}\,Mpc^{-1}}\,. \tag{1.4}$$

It describes the average behaviour of galaxies extremely well, leading to the general consideration that the redshift increases with the distance, or equivalently, as we observe back to the past, the redshift increases.

[1] In first approximation, if a nearby object is receding at a speed v, then its redshift is $z = \frac{v}{c}$, where c is the speed of light.

Homogeneity, isotropy and expansion determine the large scale structure of spacetime, the Friedmann-Lemaître-Robertson-Walker (FLRW) model of the Universe, encoded in the Robertson-Walker metric that we introduce in equation (1.5). In order to analyse an expanding Universe, it is convenient to use *comoving coordinates*, in which, by definition, the coordinate system follows the expansion, in such a way that a galaxy with no peculiar velocity keeps its coordinates constant. Then, the most general line element has the following form:

$$ds^2 = g_{\mu\nu} dx^\mu dx^\nu = \\ dt^2 - dR^2(t) = dt^2 - a^2(t) \left(\frac{dr^2}{1 - Kr^2} + r^2 d\theta^2 + r^2 sin^2\theta \, d\phi^2 \right) , \quad (1.5)$$

where (t, r, θ, ϕ) are the comoving (spherical) coordinates and the scale factor $a(t)$ describes the expansion. The spatial curvature K describes the geometry, it assumes the value $+1$ for an open Universe, 0 for a flat Universe, and -1 for a closed Universe. If two galaxies are separated by a coordinate distance r_0, the corresponding *physical* distance $R(t)$ is:

$$R(t) = a(t)\, r_0 \, . \quad (1.6)$$

In this way, if we derive equation (1.6) with respect to time, we find that:

$$V_r = \dot{a}\, r_0 = \frac{\dot{a}}{a} R(t) = H\, R(t) \, , \quad (1.7)$$

which is in fact the *recession* velocity among both galaxies. The relation above is indeed Hubble's law, (1.2) (a dot denotes a derivative with respect to cosmic time t). We have also defined the Hubble parameter as:

$$H(t) = \frac{\dot{a}}{a} \, , \quad (1.8)$$

whose present value is given by the Hubble constant in equation (1.3). Having dimension of $(\text{Time})^{-1}$, it offers a natural scale for the age of the Universe:

$$H_0^{-1} = 9.778\, h^{-1}\, \text{Gyr} \, . \quad (1.9)$$

1.2 The Equations of the Universe

General Relativity provides the classical framework that describes the dynamics of spacetime. *Einstein equation* relates geometry to matter content:

$$G_{\mu\nu} \equiv R_{\mu\nu} - \frac{1}{2} \mathcal{R}\, g_{\mu\nu} = 8\pi G\, T_{\mu\nu} \, . \quad (1.10)$$

In this set of tensor equations, $G_{\mu\nu}$, Einstein's tensor, describes geometry: $R_{\mu\nu}$ is the so-called Ricci tensor and $\mathcal{R}$ is the Ricci scalar curvature, both functions of the metric $g_{\mu\nu}$. On the other hand, $T_{\mu\nu}$ is the energy-momentum tensor describing the matter content. The energy-momentum tensor of a perfect fluid is

$$T^{\mu\nu} = (\rho + p)u^\mu u^\nu - p g^{\mu\nu}\,, \tag{1.11}$$

where u^μ is the 4-velocity of the fluid, and ρ and p are the energy density and pressure measured by a comoving observer. Furthermore, the symmetry properties of the Robertson-Walker metric reduce the ten coupled differential Einstein equations to only two of them, the so-called *Friedmann equations*, which only depend on the scale factor $a(t)$. They are:

$$\frac{\dot{a}^2}{a^2} + \frac{K}{a^2} = \frac{8\pi G}{3}\,\rho\,, \tag{1.12}$$

$$2\frac{\ddot{a}}{a} + \frac{\dot{a}^2}{a^2} + \frac{K}{a^2} = -8\pi G\, p\,, \tag{1.13}$$

where we recall that the dot denotes the derivative with respect to the cosmic time t, and $H = \dot{a}/a$ is the Hubble parameter, defined in equation (1.8).
The energy density, ρ, should be thought as a sum running over all the forms of matter that fill the Universe; the same applies to p.
In both Friedmann equations the left-hand sides are given by the left-hand side of the Einstein equation (1.10), in other words the geometry of a homogeneous and isotropic Universe is fully characterized by the scale factor $a(t)$, whereas the right-hand sides of Friedmann equations directly come from the energy-momentum tensor $T^{\mu\nu}$ of equation (1.11); at a cosmological level, following Einstein's equation, geometry is related to matter.

It is convenient to introduce two important quantities:

- the so-called *critical density* ρ_c, defined as

$$\rho_c \equiv \frac{3\,H^2}{8\pi G}\,, \tag{1.14}$$

- and the *density parameter* Ω, defined as

$$\Omega \equiv \frac{\rho}{\rho_c} = \frac{8\pi G}{3\,H^2}\,\rho\,. \tag{1.15}$$

In particular, the *current critical density* $\rho_{c,0}$ is:

$$\rho_{c,0} = \frac{3\,H^2}{8\pi G} = 1.879\,h^2\,\times\,10^{-29}\,\mathrm{g\,cm^{-3}} = 8.099\,h^2\,\times\,10^{-11}\,\mathrm{eV}^4\,. \tag{1.16}$$

The first Friedmann equation (1.12) can then be rewritten as:

$$H^2 = \frac{8\pi G}{3}\,\rho - \frac{K}{a^2} \longrightarrow \frac{K}{H^2 a^2} = \Omega - 1\,. \tag{1.17}$$

That is, the matter content, given by Ω, determines the spatial geometry of the Universe:

- **open Universe:** $K = -1 \implies \rho < \rho_c \implies \Omega < 1$;
- **flat Universe:** $K = 0 \implies \rho = \rho_c \implies \Omega = 1$;
- **closed Universe:** $K = +1 \implies \rho > \rho_c \implies \Omega > 1$.

Recent measurements of CMB radiation have shown that the Universe is spatially flat ($\Omega = 1$ or $K = 0$) to within a few percent (see, e.g., Ref. [7]).

We can rewrite equations (1.12) and (1.13) to obtain a more convenient form for the second Friedmann equation:

$$\frac{\ddot{a}}{a} = -\frac{4\pi G}{3}\,(\rho + 3p) = -\frac{4\pi G}{3}\,\rho(1 + 3\omega)\,, \tag{1.18}$$

where $\omega = p/\rho$ is the fluid *equation of state parameter*. This fully characterizes the fluid, in such a way that, for the case of a fluid composed by relativistic matter (that we collectively call *radiation*), $\omega_r = 1/3$, while for regular baryons, in general any non-relativistic, or *cold* matter, whose temperature is much smaller than its mass, $\omega_m = 0$.

Deriving the first Friedmann equation with respect to time

$$\frac{d}{dt}(\dot{a}^2 + K) = \frac{d}{dt}\left(\frac{8\pi G}{3}\,\rho\, a^2\right) \implies 2\dot{a}\ddot{a} = \frac{8\pi G}{3}\,(\dot{\rho} a^2 + 2\rho\, a\dot{a})\,, \tag{1.19}$$

and using equation (1.18), we obtain the fluid equation

$$-\,(\rho + 3p)\, a\dot{a} = \dot{\rho}\, a^2 + 2\rho\, a\dot{a} \implies \dot{\rho} = -3H\,(\rho + p)\,. \tag{1.20}$$

Notice that it can be analogously obtained using the conservation of the energy-momentum tensor of a perfect fluid:

$$T^{\mu}_{\nu;\mu} = 0\,, \tag{1.21}$$

where $_{;\mu}$ represents the covariant derivative.

Equation (1.20) describes the dependence of the energy density on the scale factor, for an equation of state $p = \omega\rho$:

$$\dot{\rho}a = -3\rho\,(1+\omega)\dot{a}\,, \tag{1.22}$$

from which:

$$\frac{1}{3\,(1+\omega)}\int\frac{d\rho}{\rho} = \int\frac{da}{a}\,, \tag{1.23}$$

and therefore,

$$\rho \propto a^{-3(1+\omega)}\,. \tag{1.24}$$

Following equation (1.24), the behaviours of matter and radiation energy densities are

- $\rho_r \propto a^{-4}$, for radiation;
- $\rho_m \propto a^{-3}$, for matter.

These behaviours can also be understood from a more intuitive point of view. In the case of matter density, the density is falling as the volume of the Universe increases, i.e., with the scale factor to the third power, since the number of particles is constant. In the case of radiation there is an additional a^{-1} factor coming from the fact that the wavelength also increases with the expansion, in such a way that the energy density scales inversely with the fourth power of the scale factor.

We can also analyse the behaviour of the scale factor as a function of time[2]

$$\frac{\dot{a}}{a} \propto a^{-3(1+\omega)/2}\,, \tag{1.25}$$

which, integrated,

$$\int da\, a^{3(1+\omega)/2}\, a^{-1} \propto \int dt \tag{1.26}$$

leads to:

$$a(t) \propto (t-t_0)^{\frac{2}{3(1+\omega)}}\,, \tag{1.27}$$

where t_0 is a constant. An analytical expression for the Hubble parameter can be found as:

$$H(t) = \frac{2}{3(1+\omega)(t-t_0)}\,. \tag{1.28}$$

[2]Here and in the following, we assume $K = 0$ unless otherwise stated.

Equations (1.27) and (1.28) are valid for all values of ω except $\omega = -1$. When ω is -1, i.e. $p = -\rho$, it follows from equation (1.24) that the energy density ρ is constant. This corresponds to the cosmological constant, denoted by Λ.

Through equation (1.27) we can understand the behaviour of the scale factor $a(t)$ depending on the dominant contribution to the energy density of the Universe:

- for a radiation dominated Universe $a(t) \propto t^{1/2}$,
- for a matter dominated Universe $a(t) \propto t^{2/3}$,
- finally, in the case of a cosmological constant dominated Universe, the scale factor evolves as $a(t) \propto \exp(H\,t)$, that is, it has an exponential expansion.

In order to analyse the dominant component at different epochs, one needs to know what the values that the observed densities of the different components of the Universe assume nowadays.
The current densities of the baryonic matter and the total matter (dark plus baryonic), neutrinos, and photons are:

$$\begin{aligned} \rho_{b,0} &= 0.857 \times 10^{-30}\,\Omega_{b,0}\,h^2\,\mathrm{g\,cm^{-3}} \\ &\approx 1.62 \times 10^{-12}\,\mathrm{eV}^4 \\ \Omega_{b,0} &= 0.02205 \pm 0.00028\,; \end{aligned} \tag{1.29}$$

$$\begin{aligned} \rho_{m,0} &= 0.502 \times 10^{-29}\,\Omega_{m,0}\,h^2\,\mathrm{g\,cm^{-3}} \\ &\approx 1.21 \times 10^{-11}\,\mathrm{eV}^4 \\ \Omega_{m,0} &= 0.315 \pm 0.017\,; \end{aligned} \tag{1.30}$$

$$\begin{aligned} \rho_{\nu,0} &= 3.194 \times 10^{-34}\,\mathrm{g\,cm^{-3}} \\ &= 8.69 \times 10^{-13}\,\mathrm{eV}^4 \\ \Omega_{\nu,0} &\simeq 1.7 \times 10^{-5}\,; \end{aligned} \tag{1.31}$$

$$\begin{aligned} \rho_{\gamma,0} &= 4.64 \times 10^{-34}\,\mathrm{g\,cm^{-3}} \\ &= 3.37 \times 10^{-15}\,\mathrm{eV}^4 \\ \Omega_{\gamma,0} &\simeq 2.5 \times 10^{-5}\,. \end{aligned} \tag{1.32}$$

The value of the baryonic density comes from the limits on the light element production in the early Universe, the so-called *Nucleosynthesis epoch*, which requires $\Omega_{b,0}h^2 \approx 0.02$, a result in agreement with other observational results, like CMB anisotropies. The total matter density, $\Omega_{m,0} \approx 0.3$, is mainly measured gravitationally via the rotation curves of galaxies, gravitational lensing, X-ray emission from hot gas in clusters of galaxies, and via measurements of peculiar velocities in the large scale structure distribution. An upper limit on the neutrino density is obtained using the limits on the sum of the total masses of the three mass eigenstates [8]. The photon density is measured via the temperature of the CMB radiation.
As we can see, the matter density is currently at least five orders of magnitude larger than the radiation density. Radiation energy density falls off more rapidly than matter energy density, therefore, there was a time in which both densities contributed equally to the energy density of the Universe. This time, the so-called *equality epoch*, separates the early radiation dominated epoch from the subsequent matter domination. Notice that while $\Omega_{m,0} \approx 0.3$, baryonic matter only provides $\Omega_{b,0} \approx 0.04$: *dark matter* accounts for that difference. In addition, as anticipated previously, the total energy density is quite closely the critical one, i.e. $\Omega = 1$, but the contributions (1.29) to (1.32) do not sum up to 1! The missing piece is attributed to *dark energy*, which would then be the current dominant contribution: we thus live in a dark energy, or cosmological constant dominated, epoch.

1.3 The Age of the Universe

We devote this Section to what probably was one of the first indications of the existence of dark energy: the age of the Universe [9, 10, 11].
As we have discussed in Section 1.1, referring to equation (1.9), the inverse of the Hubble parameter gives roughly the age of the Universe.

We rewrite the first Friedmann equation:

$$H^2 = \frac{8\pi G}{3}\,\rho - \frac{K}{a^2}\,, \tag{1.33}$$

where the energy density has to be thought of as the sum over all the components, namely relativistic matter, non-relativistic matter and the cosmological constant,

$$\rho = \sum_i \rho_{i,0} \left(\frac{a}{a_0}\right)^{-3(1+\omega)} = \sum_i \rho_{i,0}(1+z)^{3(1+\omega)}\,. \tag{1.34}$$

Using equation (1.34), for a flat Universe ($K = 0$), the Hubble parameter reads:

$$H^2(z) = H_0^2 \sum \Omega_{i,0}(1+z)^{3(1+\omega)}\,, \tag{1.35}$$

where we have considered, besides the relativistic and non-relativistic matter, an extra component coined dark energy and $\Omega_{i,0} = \frac{\rho_{i,0}}{\rho_{c,0}} = \frac{3H_0^2\rho_{i,0}}{8\pi G}$. That is,

$$H(z) = H_0 \left[\Omega_{r,0}(1+z)^4 + \Omega_{m,0}(1+z)^3 + \Omega_{r,0}(1+z)^{3(1+\omega_{DE})}\right]^{1/2} . \tag{1.36}$$

The total energy density is:

$$\rho_0 = \rho_{m,0} + \rho_{r,0} + \rho_{\Lambda,0} \, , \tag{1.37}$$

or

$$1 = \Omega_{m,0} + \Omega_{r,0} + \Omega_{\Lambda,0} \, . \tag{1.38}$$

Let us consider a Universe filled only with non-relativistic matter, $\omega = 0$, and a cosmological constant, $\omega = -1$. Then, the Hubble parameter becomes:

$$H^2(z) = H_0^2[\Omega_{m,0}(1+z)^3 + \Omega_{\Lambda,0}] \, . \tag{1.39}$$

Using the relation

$$dt = -\frac{dz}{(1+z)\,H} \, , \tag{1.40}$$

the age of the Universe is:

$$t_0 = \int_0^\infty \frac{dz}{(1+z)\,H(z)} \, . \tag{1.41}$$

We compute the integral in equation (1.41) making some assumptions. We have neglected relativistic matter since it plays a small role in the late Universe; in addition the radiation dominated epoch is much shorter than the total age of the Universe or, in other words, the integral in equation (1.41) is not particularly affected by redshifts $z > 1000$. The age of the Universe is then

$$t_0 = \frac{1}{H_0} \int_0^\infty \frac{dz}{(1+z)[\Omega_{m,0}(1+z)^3 + \Omega_{\Lambda,0}]^{1/2}} \, . \tag{1.42}$$

Integrating equation (1.42), and using $\Omega_{m,0} + \Omega_{\Lambda,0} = 1$, we obtain:

$$t_0 = \frac{1}{3\,H_0} \frac{1}{\sqrt{1-\Omega_{m,0}}} \log\left[\frac{1+\sqrt{1-\Omega_{m,0}}}{1-\sqrt{1-\Omega_{m,0}}}\right] . \tag{1.43}$$

In the limit $\Omega_{\Lambda,0} \to 0$, $\Omega_{m,0} \to 1$, we find that:

$$t_0 = \frac{2}{3\,H_0} \, . \tag{1.44}$$

A Universe without a cosmological constant would have, approximately, an age within the range 8 Gyr $< t_0 <$ 10 Gyr (1 Gyr $= 10^9$ years), where we have put $h = 0.68$. However, different groups have estimated the age of globular clusters [12] to be within the range 12.7 Gyr $< t_0 <$ 13.5 Gyr. In most cases, globular clusters seem to be older than 11 Gyr, being inconsistent with the age of a matter dominated Universe. The age of the Universe increases by including dark energy with an equation of state with ω close to -1.
On the other hand, if we consider an open Universe, $\Omega_{K,0} > 0$ and the cosmic age increases but still remains low compared to the age of the globular clusters mentioned above. As an example, let us consider a Universe with $\Omega_{m,0} + \Omega_{K,0} = 1$ (and hence zero cosmological constant). Then, the age of the Universe would be:

$$t_0 = \frac{1}{H_0} \frac{1}{1-\Omega_{m,0}} \left[1 + \frac{\Omega_{m,0}}{2\sqrt{1-\Omega_{m,0}}} \log \left(\frac{1+\sqrt{1-\Omega_{m,0}}}{1-\sqrt{1-\Omega_{m,0}}} \right) \right] , \tag{1.45}$$

where, in the limit $\Omega_{K,0} \to 1$, $\Omega_{m,0} \to 0$, the age of the Universe becomes $t_0 = \frac{1}{H_0} = 13$ Gyr. However, the curvature of the Universe has been constrained by the recent Planck measurements [6], to be much smaller than unity. An open Universe without dark energy is inconsistent with the age of the oldest stars present in the Universe, while a flat Universe with a cosmological constant is consistent with the Planck constraints, for a matter density value of $\Omega_{m,0} = 0.3089$, and for a dark energy density of $\Omega_{\Lambda,0} = 0.6911$.

In the following Sections, we will explore the most salient features of the three eras that have characterized the history of the Universe: the radiation, the matter and the dark energy epochs.

1.4 Radiation Dominated Epoch

Since expansion of the Universe dilutes densities, the conditions in the past must have corresponded to higher densities and thus, to higher temperatures. This points back to the initial dense and hot state from which the Universe has evolved. In this Big Bang picture, the evolution of the Universe is essentially a thermal history of expansion and cooling. To describe it, thermodynamics is required.

1.4.1 Thermodynamics of the Early Universe

The most relevant quantities associated to a weakly interacting gas of identical particles with g internal degrees of freedom are given in terms of its phase space distribution function $f(\vec{p})$. The number density n, the energy density ρ, and the pressure p are:

$$n = \frac{g}{(2\pi)^3}\int_0^\infty d^3p\, f(\vec{p})\,, \tag{1.46}$$

$$\rho = \frac{g}{(2\pi)^3}\int_0^\infty d^3p\, E(\vec{p})\, f(\vec{p})\,, \tag{1.47}$$

$$p = \frac{g}{(2\pi)^3}\int_0^\infty d^3p\, \frac{|\vec{p}|^2}{3E}\, f(\vec{p})\,, \tag{1.48}$$

where $E^2 = |\vec{p}|^2 + m^2$. For a species in thermal equilibrium, the phase space distribution function f is given by the familiar Fermi-Dirac $(+)$ or Bose-Einstein $(-)$ distributions (for fermions or bosons, respectively):

$$f(\vec{p}) = \frac{1}{\exp\left(\frac{E-\mu}{T}\right) \pm 1}\,, \tag{1.49}$$

where μ is the chemical potential of the species. If the species is in chemical equilibrium, then its chemical potential μ is related to chemical potentials of the other species with which it interacts.
From the equilibrium distributions, it follows that the number density n, the energy density ρ, and the pressure p of a species of mass m, with chemical potential μ, at temperature T are:

$$n = \frac{g}{(2\pi)^3}\int_m^\infty \frac{(E^2-m^2)^{1/2}}{\exp[(E-\mu)/T] \pm 1}\, E\, dE\,, \tag{1.50}$$

$$\rho = \frac{g}{(2\pi)^3}\int_m^\infty \frac{(E^2-m^2)^{1/2}}{\exp[(E-\mu)/T] \pm 1}\, E^2\, dE\,, \tag{1.51}$$

$$p = \frac{g}{(2\pi)^3}\int_m^\infty \frac{(E^2-m^2)^{1/2}}{\exp[(E-\mu)/T] \pm 1}\, dE\,. \tag{1.52}$$

In a situation of local thermodynamic equilibrium, the number density, the energy density and the pressure of relativistic species ($T \gg m$) are given by:

$$n = \begin{cases} \frac{\zeta(3)}{\pi^2}\, g\, T^3\,, & \text{for bosons,} \\ \frac{3}{4}\frac{\zeta}{\pi^2}\, g\, T^4\,, & \text{for fermions.}\,, \end{cases} \tag{1.53}$$

$$\rho = \begin{cases} \frac{\pi^2}{30}\, g\, T^4\,, & \text{for bosons,} \\ \frac{7}{8}\frac{\pi^2}{30}\, g\, T^4\,, & \text{for fermions.}\,, \end{cases} \tag{1.54}$$

$$p = \frac{\rho}{3}\,. \tag{1.55}$$

Here $\zeta(n)$ is the Riemann zeta function, and $\zeta(3) = 1.20206....$
In the case of non-relativistic particles ($T \ll m$), these thermodynamical quantities are given by:

$$n = g\left(\frac{mT}{2\pi}\right)^{3/4} \exp[-(m-\mu)/T]\,, \tag{1.56}$$

$$\rho = m\,n\,, \tag{1.57}$$

$$p = n\,T \ll \rho\,. \tag{1.58}$$

and the distribution function, n, converges to a Maxwell-Boltzmann distribution.

When relativistic species give the main contribution to ρ and p, i.e. during the radiation dominated epoch that we are describing in this Section, the above expressions simplify to:

$$\rho = \frac{\pi^2}{30}\,g_*\,T^4\,, \tag{1.59}$$

$$p = \frac{\rho}{3} = \frac{\pi^2}{90}\,g_*\,T^4\,, \tag{1.60}$$

where g_* counts the total number of degrees of freedom of relativistic[3] fermions and bosons i (i.e. those species with mass $m_i \ll T$):

$$g_* = \sum_{i=bosons} g_i \left(\frac{T_i}{T}\right)^4 + \frac{7}{8}\sum_{i=fermions} g_i \left(\frac{T_i}{T}\right)^4\,. \tag{1.61}$$

Furthermore, when $g_* \simeq$ constant, $p = \frac{\rho}{3}$ (i.e. $\omega = 1/3$) and $a(t) \propto t^{1/2}$. Then, we have (the Planck mass is $M_P = 1/\sqrt{G}$):

$$H = \sqrt{\frac{8\pi^3}{90}}\,g_*^{1/2}\,\frac{T^2}{M_P} \simeq 1.66\,g_*^{1/2}\,\frac{T^2}{M_P}\,, \tag{1.62}$$

$$t = \frac{1}{2H} \simeq 0.301\,g_*^{-1/2}\,\frac{M_P}{T^2}\,. \tag{1.63}$$

In the evolution of the Universe, when the reaction rates Γ_{int} (which in general depend on the temperature) of particles in the thermal bath are much larger than the expansion rate, H, local thermal equilibrium is maintained. In this case, the entropy

[3]Since g_* is related to the number of relativistic species in the Universe, and massive species change from relativistic to non-relativistic when $T \sim m$, it is a function of the cosmological temperature T.

per comoving volume element remains constant. The entropy in a comoving volume provides a very useful fiducial quantity during the expansion. On the contrary, when the rate of interactions coupling a species to the expanding fluid becomes smaller than the expansion rate, this species decouples and evolves independently. In order to estimate the temperatures of the different species after they leave equilibrium, we can use the fact that the expansion is adiabatic.[4] For a given comoving volume V:

$$T\,dS = d(\rho\,V) + p\,dV = V\,d\rho + (\rho + p)dV = d[(\rho + p)V] - V\,dp\,, \tag{1.64}$$

where ρ and p are the equilibrium energy density and pressure, respectively. Using:

$$dS = \left(\frac{\partial S}{\partial \rho}\right)\left(\frac{d\rho}{dT}\right)dT + \left(\frac{\partial S}{\partial V}\right)dV\,, \tag{1.65}$$

we obtain:

$$\frac{\partial S}{\partial T} = \left(\frac{\partial S}{\partial \rho}\right)\left(\frac{d\rho}{dT}\right)dT = \frac{V}{T}\,\frac{d\rho}{dT}\,, \tag{1.66}$$

$$\frac{\partial S}{\partial V} = \frac{\rho + p}{T}\,. \tag{1.67}$$

From the integrability condition,

$$\frac{\partial^2 S}{\partial T\,\partial V} = \frac{\partial^2 S}{\partial V\,\partial T}\,, \tag{1.68}$$

we have:

$$\frac{\partial}{\partial T}\left(\frac{\rho + p}{T}\right) = -\frac{1}{T^2}(\rho + p) + \frac{1}{T}\frac{d\rho}{dT} + \frac{1}{T}\frac{dp}{dT} = \frac{\partial}{\partial V}\left(\frac{V}{T}\frac{d\rho}{dT}\right) = \frac{1}{T}\frac{d\rho}{dT}\,, \tag{1.69}$$

and therefore:

$$dp = \frac{\rho + p}{T}\,dT\,. \tag{1.70}$$

If we substitute equation (1.70) into equation (1.64), we can obtain the entropy:

$$dS = \frac{1}{T}\,d[(\rho + p)\,V] - \frac{(\rho + p)\,V}{T^2}\,dT\,, \tag{1.71}$$

[4] We recall that the second law of thermodynamics results in the formula $dS \geq \frac{dQ}{T}$. In an adiabatic transformation we have $dQ = 0$, since there is no heat exchange with the outside, and then $dS \geq 0$. The Universe, by definition, is thermally isolated, then $dS_{Universe} \geq 0$.

from which:

$$dS = d\left[\frac{(\rho + p)\,V}{T} + constant\right]. \tag{1.72}$$

Therefore, beside an additive constant, the entropy per comoving volume is given by:

$$S = \frac{(\rho + p)\,V}{T}. \tag{1.73}$$

Rewriting the first law (energy conservation) as:

$$d[(\rho + p)\,V] = V\,dp\,, \tag{1.74}$$

we substitute equation (1.70) into (1.74), obtaining:

$$d\left[\frac{(\rho + p)\,V}{T}\right] = 0\,. \tag{1.75}$$

This result implies that, in thermal equilibrium, the entropy per comoving volume, S, is conserved.

It is useful to define the *entropy density*, s, as:

$$s \equiv \frac{S}{V} = \frac{\rho + p}{T}\,. \tag{1.76}$$

The entropy is dominated by the contribution of relativistic particles, whose energy density and pressure are given by equations (B.11) and (1.60), respectively; therefore, the entropy density can be written as:

$$s = \frac{2\pi^2}{45}\,g_{*S}\,T^3\,, \tag{1.77}$$

where

$$g_{*S} = \sum_{i=bosons} g_i \left(\frac{T_i}{T}\right)^3 + \frac{7}{8}\sum_{i=fermions} g_i \left(\frac{T_i}{T}\right)^3. \tag{1.78}$$

As long as all particle species have the same temperature, $g_* = g_{*S}$.
Conservation of entropy implies that $S\,V \propto g_{*S}\,a^3\,T^3$ remains constant, and therefore the temperature evolves as:

$$T \propto g_{*S}^{-1/3}\,a^{-1}\,. \tag{1.79}$$

In fact, when g_{*S} is constant, the known result $T \propto a^{-1}$, is obtained.
When one of the species becomes non-relativistic or annihilates, its entropy is transferred to the other relativistic particles still present in the thermal plasma; g_{*S} becomes smaller, and the decrease of the temperature T is slower (notice however that it still scales with a^{-1}, but with a different coefficient).
An important cosmological quantity is the so-called *baryon-photon ratio*, $\eta = n_B/n_\gamma$. To obtain it, we make use of the fact that the number of photons, n_γ, is proportional to the entropy density:

$$s = \frac{2\pi^4}{90\zeta(3)}\, g_{*S}\, n_\gamma \simeq 1.8\, g_{*S}\, n_\gamma\,. \tag{1.80}$$

Then, the baryon-photon density ratio is given by:

$$\eta = \frac{n_b - \bar{n}_b}{n_\gamma} \simeq 1.8\, g_{*S}\, \frac{n_b}{s}\,, \tag{1.81}$$

where n_b and $\bar{n}_b$ are the densities of baryons and antibaryons, respectively.
As long as interactions that do not conserve baryon number occur very slowly, the baryon number in a comoving volume is conserved (except in the very early period where baryogenesis is supposed to take place). Conservation of both baryon number and entropy, implies that the ratio η varies only with g_{*S}.

1.4.2 The relic density

In the previous Sections we have seen that the history of the Universe can been understood through the evolution of the scale factor $a(t)$. What General Relativity provides through the Hubble rate $H(t) = \dot{a}/a$, is the connection between this evolution and the energy density of the Universe. Now we see that in order to understand the thermal history of the Universe we must compare particle interaction rates, Γ's, and the expansion rate, H. For $T \propto a^{-1}$, the rate of change for the temperature is set by the expansion rate $\dot{T}/T = -H$. As already mentioned, a good criterion to identify if a species is in equilibrium or not with the plasma in the Universe, is to compare its interaction rate, Γ, with the expansion rate H: if $\Gamma < H$, interactions with the plasma are not sufficient to keep that species in equilibrium, i.e. with the same (plasma) temperature. That species *decouples*.

1.4.2.1 Chemical and kinetic decoupling

A first example of that decoupling phenomenon concerns the amount of dark matter (DM) left over in the evolution of the early Universe. We focus on a popular class of

plausible cold dark matter (CDM) candidates, *Weakly Interacting Massive Particles* (WIMPs) [13, 14], stable particles, having rather weak interactions with standard model (SM) particles, which can yield the correct abundance to reproduce the observed DM density. In early times, at high temperatures, they are coupled with the rest of the plasma in such a way that processes of pair–annihilation and pair–creation,

$$X + \bar{X} \rightleftarrows l + \bar{l}\,, \tag{1.82}$$

mantained WIMPs in equilibrium. X stands for WIMP and $\bar{X}$ is its anti-particle,[5] while l and $\bar{l}$ denote generic components of the primordial plasma. It is important to stress that WIMPs are not only in thermal equilibrium, but in *chemical equilibrium*: although pair–annihilation and pair–creation do change the amount of dark matter, at that stage both reactions are balanced, they proceed with the same rate. As the Universe expands and the average distance between particles increases, both processes slow down. In a very simplistic picture, they just "stop", and the DM population, not interacting anymore with the plasma, *freezes-out*: the WIMP number density per comoving volume remains practically constant until today. A more detailed description involves a proper treatment of the dynamical evolution of the DM density: this is given by the Boltzmann equations. In Appendix B additional details can be found, for the moment let us concentrate on a simple derivation of the dark matter relic density. In a generic WIMP scenario, two DM particles X can annihilate producing two light particles l – (1.82) –. If n_X and n_l are the number densities of X and l (respectively), the Boltzmann equation reads:

$$a^{-3}\frac{d(n_X a^3)}{dt} = n_{X,eq}^2\langle\sigma v\rangle\left\{\frac{n_l^2}{n_{l,eq}^2} - \frac{n_X^2}{n_{X,eq}^2}\right\}, \tag{1.83}$$

where $\langle\sigma v\rangle$ is the averaged annihilation cross section times the relative velocity of the DM particles, while $n_{l,eq}$ and $n_{X,eq}$ correspond, respectively, to the number densities of light and WIMP particles at thermal equilibrium. Since the light particles are assumed to be part of the cosmic plasma (or equivalently in equilibrum with it), then $n_{l,eq} = n_l$, and the Boltzmann equation becomes:

$$a^{-3}\frac{d(n_X a^3)}{dt} = \langle\sigma v\rangle\left\{n_{X,eq}^2 - n_X^2\right\}. \tag{1.84}$$

Introducing the number of WIMPs per coming volume N_X and the entropy density in (1.77), we have

$$\frac{dN_X}{dt} = s\,\langle\sigma v\rangle\left\{N_{X,eq}^2 - N_X^2\right\}. \tag{1.85}$$

Changing to a more convenient variable for the time evolution, $x = m_X/T$,

$$\frac{dN_X}{dx} = \frac{2\pi^2}{45}g_{*S}(T)\frac{m_X^3\langle\sigma v\rangle}{H(m_X)}\frac{1}{x^2}\left\{N_{X,eq}^2 - N_X^2\right\}. \tag{1.86}$$

[5] In case the WIMP is its own anti-particle, we have $X = \bar{X}$.

This differential equation is a Riccati equation, which does not have an analytic solution (of course, numerical solutions can be obtained). However, some simple considerations are sufficient to obtain a good estimate of the relic density. First, since $N_{X,eq}$ will drop with the temperature, we neglect it:

$$\frac{dN_X}{dx} = -\frac{2\pi^2}{45} g_{*S}(T) \frac{m_X^3 \langle \sigma v \rangle}{H(m_X)} \frac{1}{x^2} N_X^2 \,. \tag{1.87}$$

Next, one can integrate from the freeze out time (or temperature), x_f to a much later instant $x \to \infty$, to obtain

$$\frac{1}{N_X^\infty} - \frac{1}{N_X^f} = \frac{2\pi^2}{45} g_{*S}(T) \frac{m_X^3 \langle \sigma v \rangle}{H(m_X)} \frac{1}{x_f} \,. \tag{1.88}$$

Since $N_X^\infty \ll N_X^f$, we are left with

$$\frac{1}{N_X^\infty} \simeq \frac{2\pi^2}{45} g_{*S}(T) \frac{m_X^3 \langle \sigma v \rangle}{H(m_X)} \frac{1}{x_f} \,. \tag{1.89}$$

It is important to stress that the abundance of WIMPs after freeze out, the relic density N_X^∞, is inversely proportional to the annihilation cross section $\langle \sigma v \rangle$: larger annihilation cross sections give later decoupling times and smaller relic densities. In order to reproduce the relic density as measured by Planck, $\Omega_{DM} h^2 = 0.1197$, the required annihilation cross section is

$$\langle \sigma v \rangle \sim 3 \times 10^{-26} \, \mathrm{cm}^3 \, \mathrm{s}^{-1}. \tag{1.90}$$

This cross section value coincides with typical weak interaction cross sections, hence the interest and popularity of WIMPs: WIMPs will typically have the right cross sections to reproduce the correct relic density of DM.

Chemical decoupling set the relic abundance of DM, but it may not signal the end of DM interactions. Indeed, after the freeze-out, WIMPs can still undergo elastic scattering processes with other particles of the primordial plasma:

$$X \, l \to X \, l \,. \tag{1.91}$$

This process does not change the amount of X's, but can still keep WIMPs in equilibrium with the plasma: in this case one refers to *kinetic equilibrium*. When the rates of these processes drop below the expansion rate of the Universe, WIMPs finally decouple and we have *kinetic decoupling*. The idea of *kinetic decoupling* is relevant for considerations related to the formation of DM structures under the influence of gravity (as we will address later): before kinetic decoupling, interaction with the plasma can inhibit the formation of DM structures below a certain scale through the process of the collisional damping [15, 16].

Summarizing, the chemical decoupling of WIMPs in the early universe determines their relic density today. Kinetic decoupling, on the other hand, happens only considerably later and sets a scale that can directly be translated into a small-scale cutoff in the spectrum of matter density fluctuations, corresponding to the least massive protohalos that can form, an argument that will be taken on in Chapter 4.

1.4.3 Decoupling of Neutrinos and $e^{\pm}$ annihilation

As we have seen before, to maintain a species in local thermodynamical equilibrium, it is necessary that the interaction rate Γ is larger than the expansion rate of the Universe, H. In the early Universe, massless neutrinos are kept in equilibrium via electroweak interactions whose cross section is approximately given by $\sigma \simeq G_F^2 T^2$, where $G_F^2 = (292.80 \text{ GeV})^{-2}$ is the Fermi constant. For relativistic neutrinos the number density is $n \propto T^3$, so that the interaction rate (per neutrino) is:

$$\Gamma_{int} = n\sigma|v| \simeq G_F^2 T^5 \,, \tag{1.92}$$

where $|v| \approx 1$. Comparing Γ_{int} in equation (1.92) with the expansion rate in equation (1.62),

$$\frac{\Gamma_{int}}{H} \simeq \frac{M_P G_F^2 T^5}{T^2} \simeq \left(\frac{T}{0.8\,MeV}\right)^3 , \tag{1.93}$$

and thus, at temperatures below 0.8 MeV, the electroweak interaction rate is not able to keep the neutrinos in thermodynamical equilibrium. At temperatures of order 1 MeV, neutrinos species (adequately assumed relativistic) decouple from the primordial plasma. Just after neutrino decoupling, the temperature decreases below the electron-positron mass whose annihilation transfers entropy to the photons, but not to the already decoupled neutrinos. It is then possible to estimate the difference in the temperature of photons and neutrinos using equation (1.79). Because of the annihilation of $e^{\pm}$ pairs, the number of degrees of freedom of the primordial plasma decreases from $g_* = 2 + \frac{7}{2} = \frac{11}{2}$ to $g_* = 2$ (just photons). As discussed before, a decrease in g_* does not lead to an actual increase in T_γ, but rather causes the T_γ decrease to slow down. This is the reason why aT_γ in equation (1.79) is larger by a factor $\left(\frac{11}{4}\right)^{1/3}$, while aT_ν remains constant. After $e^{\pm}$ annihilation, aT_γ remains constant too. Therefore, the present ratio of T_γ and T_ν is:

$$\frac{T_{\gamma,0}}{T_{\nu,0}} = \left(\frac{11}{4}\right)^{1/3} \simeq 1.40 \,. \tag{1.94}$$

Since we measure $T_{\gamma,0} = 2.728$ K (we just anticipate the result of the CMB measurements in Section 1.5.1), the current expected neutrino temperature is $T_{\nu,0} \simeq 1.94$ K.

It is then possible to calculate the number of degrees of freedom g_* and g_{*S} today (assuming 3 massless neutrino species), both constant after $e^{\pm}$ annihilation:

$$g_* = 2 + \frac{7}{8} \times 2 \times 3 \times \left(\frac{4}{11}\right)^{4/3} = 3.36\,, \tag{1.95}$$

$$g_{*S} = 2 + \frac{7}{8} \times 2 \times 3 \times \frac{4}{11} = 3.91\,. \tag{1.96}$$

With $T_{\gamma,0} = 2.728$ K, the present number densities of photons and neutrinos are

$$n_{\gamma,0} = \frac{2\zeta(3)}{\pi^2}\, T^3 \approx 420\,\mathrm{cm}^{-3}\,, \tag{1.97}$$

$$n_{\nu,0} = \frac{2\zeta(3)}{\pi^2}\, T^3 = \frac{3}{11}\, n_{\gamma,0} \approx 115\,\frac{\mathrm{cm}^{-3}}{\mathrm{flavor}}\,. \tag{1.98}$$

The corresponding energy density of photons is:

$$\rho_{\gamma,0} = \frac{2\pi^2}{30} T^4 = 4.64 \times 10^{-34}\,\mathrm{g\ cm}^{-3}\,, \tag{1.99}$$

or, in terms of the critical density:

$$\Omega_{\gamma,0}\, h^2 = \frac{\rho_{\gamma,0}}{\rho_{c,0}} \simeq 2.5 \times 10^{-5}\,. \tag{1.100}$$

In this way, we can estimate the entropy of the Universe:

$$s = \frac{2\pi^2}{45}\, g_{*S}\, T^3 \equiv 2970\,\mathrm{cm}^{-3}\,, \tag{1.101}$$

as well as the baryon-photon ratio:

$$\eta_b = 7.04 \frac{n_b}{s} = \frac{\rho_b}{M_P\, s} \approx 2.75 \times 10^{-8}\,\Omega_{b,0}\, h^2 \approx 5.5 \times 10^{-10}\,, \tag{1.102}$$

that is, there are $\sim 10^{10}$ photons per baryon!

A key question in particle physics addressing the early Universe concerns the baryon asymmetry problem, whose name is *baryogenesis*.

1.4.4 Baryogenesis

One of the outstanding challenges of the interface between particle physics and cosmology is the explanation of the observed baryonic asymmetry in the Universe.
All astrophysical observations indicate that our visible Universe is dominated by matter and there is very little antimatter. This matter dominance in our Universe is crucial for our existence, but an understanding of why there is more matter than antimatter is difficult.

The so-called baryon asymmetry of the Universe (BAU) is characterized by the ratio of the baryon number density to the photon entropy density η_b that we have presented in equation (1.102). We know from studies of the Cosmic Microwave Background and Big Bang nucleosynthesis that η_b is of the order of 10^{-10}.

In this baryon asymmetry problem, called *baryogenesis*, all antibaryons, or more generally speaking, antimatter, annihilate with baryonic matter producing radiation and only a relatively small amount of antibaryons can survive up to the present day. Such an annihilation has made the asymmetry much greater today than in the early Universe. Indeed, at high temperature, during the first instants of the Universe life, there were large numbers of thermal quark-antiquark pairs. Kolb and Turner [17], estimated 30 million antiquarks for every 30 million and 1 quarks during this epoch, in such a way that there is a tiny asymmetry!

There is currently insufficient observational evidence to explain why the Universe contains far more baryons than antibaryons. A candidate explanation for this phenomenon must allow the Sakharov conditions to be satisfied at some time after the end of cosmological inflation.

In 1967, Andrei Sakharov [18] enunciated the three conditions necessary to account for the baryon-antibaryon asymmetry of the Universe. *Sakharov's conditions* for the creation of non-zero baryon number from an initially baryon symmetric state are:

- the *baryon number* must be violated;
- C (charge conjugation) and CP (charge conjugation combined with parity) must be violated;
- the asymmetry must be created under *non-equilibrium conditions*.

Concerning the first condition, it is evident that, if the baryon asymmetry developed from a symmetric high temperature state, the baryon number must have been vio-

lated at some stage. Baryon number violation is a generic feature of grand unified theories which unify the strong and the electroweak interaction.
The second condition is necessary in order to ensure that a net baryon number is created, even in the presence of interactions which violate baryon conservation. C and CP violation have been observed in the weak interactions of several systems (for example kaons and B mesons).
The third condition is necessary because baryons and antibaryons have the same mass and so, thermodynamically, they would have the same abundances in thermodynamic equilibrium, despite the violation of the baryon number and C and CP invariance.
This last condition states that the rate of a reaction which generates baryon-asymmetry must be less than the rate of expansion of the Universe. In this situation the particles and their corresponding antiparticles do not achieve thermal equilibrium due to rapid expansion decreasing the occurrence of pair annihilation.

In principle, the Standard Model of elementary particle physics contains all of these ingredients, but they are not present with an amount sufficient to produce the observed abundance of baryonic matter. Consequently, we must look for physics beyond the Standard Model in order to find a successful baryogenesis mechanism, and this open problem is beyond the scope of our discussion.

The next step after baryogenesis is the much better understood *primordial nucleosynthesis*, during which light atomic nuclei began to form.

1.4.5 Primordial Nucleosynthesis

Our next milestone is *primordial nucleosynthesis*. According to detailed calculations (see e.g. [17]), nucleosynthesis might have occurred at energies around $T \approx 0.1$ MeV. A priori one would expect that nucleosynthesis occurs at higher temperatures, since the binding energies of nucleons in nuclei have, typically, values in the range of several MeV. Since the complete treatment is well beyond the scope of this Section, we just comment some of the basic features underlying the full picture.
The main factor responsible for this low temperature is the extremely large entropy of the Universe. When the temperature drops below some typical nuclear binding energy, most photons do not have enough energy to reverse the binding of nucleons. Nevertheless, in the thermal distribution of photons, because of their overabundance, the absolute number of them having energies higher than this typical binding energy is indeed sufficient to block the process. This fact holds the nucleosynthesis process until lower temperatures.

The ratio of neutrons to protons is of particular importance to the outcome of primordial nucleosynthesis. When the weak interaction rate drops below the Hubble

rate and neutrinos leave equilibrium, the weak reactions that convert protons into neutrons, and viceversa,

$$\nu_e + n \quad \rightleftarrows \quad p + e^- \,, \tag{1.103}$$

$$e^+ + n \quad \rightleftarrows \quad p + \bar{\nu}_e \,, \tag{1.104}$$

stop, freezing the neutron to proton ratio.

Therefore, considering the Maxwell-Boltzmann distribution in equation (1.56), with a temperature $T = 0.8$ MeV, and in the case in which $\Gamma_{int} < H$, we obtain:

$$\frac{n_n}{n_p} \approx e^{-(m_n - m_p)/T} \approx 0.2 \approx \frac{1}{5} \,, \tag{1.105}$$

where $m_n = 939.565$ MeV and $m_p = 938.272$ MeV. Furthermore, this fraction does not remain constant, because neutrons are still converting into protons via β-decay. When the temperature reaches 0.1 MeV, the ratio has the value:

$$\frac{n_n}{n_p} \approx \frac{1}{7} \,. \tag{1.106}$$

It is then possible to give a very rough estimate of the mass fraction corresponding to ^{4}He, Y_P. Since ^{4}He is composed by 2 neutrons and 2 protons, assuming that all neutrons are used to form helium nuclei, and the excess of protons are, instead, hydrogen nuclei, we obtain:

$$Y_P = \frac{4 n_{He}}{n_N} = \frac{4(n_n/2)}{n_n + n_p} = \frac{2(n_n/n_p)}{1 + (n_n/n_p)} \approx 0.25 \,. \tag{1.107}$$

Obviously, a complete treatment should be formulated in terms of thermal distributions, etc. We refer the reader to ref. [17] for further details and just review the main results in the following.
The only isotopes that are predicted to be produced in significant amounts ($A/H > 10^{-12}$) during the epoch of primordial nucleosynthesis are: D, ^{3}He, ^{4}He, and ^{7}Li. These primordial abundances are sensitive, as anticipated, to several physical quantities: the neutron half-life $\tau_{1/2}$(n) (and thus the ratio between neutrons and protons after weak interactions stop), the number of degrees of freedom g_*, which directly affects the Hubble parameter, and the baryon to photon ratio, η, which constrains the present baryon density ($\Omega_{b,0}\, h^2 \approx 0.02$) through the abundance of light nuclei.

Primordial nucleosynthesis is the earliest clear test of the Standard Model. Nuclear reactions that took place from $t \simeq 0.01$ s to 100 s (corresponding to $T \simeq 10$ MeV to 0.1 MeV) resulted in the production of substantial amounts of D (D/H $\simeq 10^{-5}$),

^{3}He (^{3}He/H $\simeq 10^{-5}$), ^{4}He (mass fraction $Y \simeq 0.25$) and ^{7}Li (^{7}Li/H $\simeq$ 1 to 2 $\times$ 10^{-10}). D and ^{4}He are of particular importance, because there are no contemporary astrophysical processes that can account for their observed abundances. Ordinary stars produce ^{4}He. Nevertheless, even in regions where there has been significant stellar processing, the stellar contribution to Y_P is only about $\simeq 0.05$. While the observed Deuterium abundance is very small, even this small contribution is difficult to account for, because almost all astrophysical processes destroy the weakly-bound deuteron, which burns at a relatively low temperature 0.5×10^6 K.
At present there is concordance between the predicted and the observed abundances for these four isotopes, provided that the baryon to photon ratio is approximately $\eta \sim 5 \times 10^{-10}$, corresponding to $\Omega_{b,0}\, h^2 \sim 0.02$.

1.5 Matter Dominated Epoch

After primordial nucleosynthesis we are left with a plasma consisting of photons and ionized nuclei in thermal equilibrium in a radiation dominated Universe. Temperature and energy densities decrease as the Universe expands, but as analysed before, matter and radiation evolve differently, since

$$\frac{\rho_r}{\rho_m} = \frac{\rho_{r,0}}{\rho_{m,0}} \left(\frac{a_0}{a}\right) = \frac{\rho_{r,0}}{\rho_{m,0}} (1+z)\,, \tag{1.108}$$

where ρ_r and ρ_m are the radiation and matter energy densities, respectively (the subindex 0 refers to the present epoch). Thus it is possible to calculate the equality time, that is the time when ρ_m became the dominant component of energy density:

$$1 + z_{eq} = \frac{\rho_{m,0}}{\rho_{r,0}} = 2.4 \times 10^4\, \Omega_{m,0}\, h^2 \approx 3600\,, \tag{1.109}$$

which corresponds to a temperature

$$T_{eq} = T_0(1+z_{eq}) = 65472\, \Omega_{m,0}\, h^2\, \mathrm{K} \approx 9800\, \mathrm{K} \approx 0.85\, \mathrm{eV}\,. \tag{1.110}$$

Although the process of decoupling between matter and radiation is not instantaneous, for temperatures below 0.85 eV, matter is the dominant component in the right hand side of the Friedmann equation.

1.5.1 Recombination and the Cosmic Background Radiation

Equilibrium in the plasma formed by matter and radiation is maintained through Thomson scattering. However, this situation will only last until ionized nuclei capture the remaining electrons, becoming then neutral atoms which decouple from radiation: this is the so-called *recombination* process. Afterwards, radiation can travel freely in the form of the *Cosmic Microwave Background* (CMB) radiation.

Since a detailed description is much more involved than the previous outline, we will just present a qualitative overview of the recombination process that brings us to the release of the CMB. The hydrogen binding energy is the difference between the free proton plus electron masses and the bound state mass:

$$Q = m_H - (m_p - m_e) = -13.6\,\mathrm{eV}\,. \tag{1.111}$$

Therefore, a priori, neutral atoms could be formed below this temperature. For the reaction

$$p + e^- \rightleftarrows H + \gamma\,, \tag{1.112}$$

to be in equilibrium, the number densities of the species involved should follow

$$\frac{n_H}{n_e\, n_p} = \left(\frac{2\pi}{m_e\, T}\right)^{\frac{3}{2}} \exp(Q/T)\,. \tag{1.113}$$

Assuming overall charge neutrality, $n_p = n_e$, we can introduce the ionization fraction $X = \frac{n_p}{n_p + n_H}$ to obtain

$$\frac{1-X}{X} = n_p \left(\frac{2\pi}{m_e\, T}\right)^{\frac{3}{2}} \exp(Q/T)\,. \tag{1.114}$$

Using $n_p = \eta\, n_\gamma$, together with $n_\gamma = \frac{2\zeta(3)}{\pi^2} T^3 \simeq 0.24\, T^3$,

$$\frac{1-X}{X^2} = 3.84\,\eta \left(\frac{T}{m_e}\right)^{\frac{3}{2}} \exp(Q/T)\,. \tag{1.115}$$

For a reference value $X \sim 0.5$, solving for the temperature gives $T \sim 4000$ K (~ 0.3 eV), corresponding to $z \simeq 1500$: almost *two* orders of magnitude below the naive expectation. As happened with primordial nucleosynthesis, the huge amount of photons per baryon delays recombination until lower temperatures are reached. A complete

derivation yields a lower temperature, placing the *last scattering surface* (LSS) at $z \approx 1100$, when the Universe is $\sim 300,000$ years old. Photons, distributed according to a blackbody equilibrium spectrum, can then freely propagate.

The confirmation of the blackbody spectrum came only in the 90's, when it was measured by the FIRAS (Far Infrared Absolute Spectrophotometer) instrument on board of the COBE (Cosmic Background Explorer) satellite[6], which gave the 2006 Nobel prize to John Mather[19] together with George Smoot, who received it for the discovery of the anisotropies of the Cosmic Background Radiation [20].
In Fig. 1.1, the COBE curve shows an incredible agreement with a blackbody curve of the CMB radiation spectrum. In the figure, the error bars have been multiplied by a factor of 400 in order to be visible. While FIRAS measured the temperature of CMB of $T_0 = 2.725$, the recent result is [21]:

$$T_0 = 2.72548 \pm 0.00057\,\mathrm{K}. \tag{1.116}$$

The COBE observations were crucial for cosmology. From the point of view of the structure of the Universe on the very largest angular scales, they show that the cosmic radiation is homogeneously and isotropically distributed in all directions (and this is in agreement with the Cosmological Principle), with fluctuations of the order of 10^{-5}. On the other hand, such observations also show that this radiation is the cooled remnant of the very hot early phases of the Big Bang.

As stated above, the CMB presents temperature fluctuations $\delta T/T$, *anisotropies*, at the level of one part in $\sim 10^5$: the study of these anisotropies requires further understanding of the physics of the early Universe. They can be classified according to their origin:

- *primary* anisotropies are related to phenomena at the LSS and before,
- *secondary* anisotropies are related instead to effects occuring between the LSS and the observer, for example the interaction of the CMB with hot gas or with gravitational potentials.

Let us briefly describe the physical origin of them.

There are two types of effects involved in primary anisotropies: (1) acoustic oscillations and (2) collisionless damping.

[6]The only satisfactory approach for determining the detailed spectrum and the isotropy of the Cosmic Background Radiation over the whole sky was to place the receiver system in a satellite above the Earth's atmosphere,and this was achieved by the Cosmic Background Explorer (COBE) of NASA, which was launched in November 1989. The mission was dedicated to studies of the background radiation, not only in the millimetre and submillimetre, but also throughout the infrared waveband from 2 to 1000 μm.

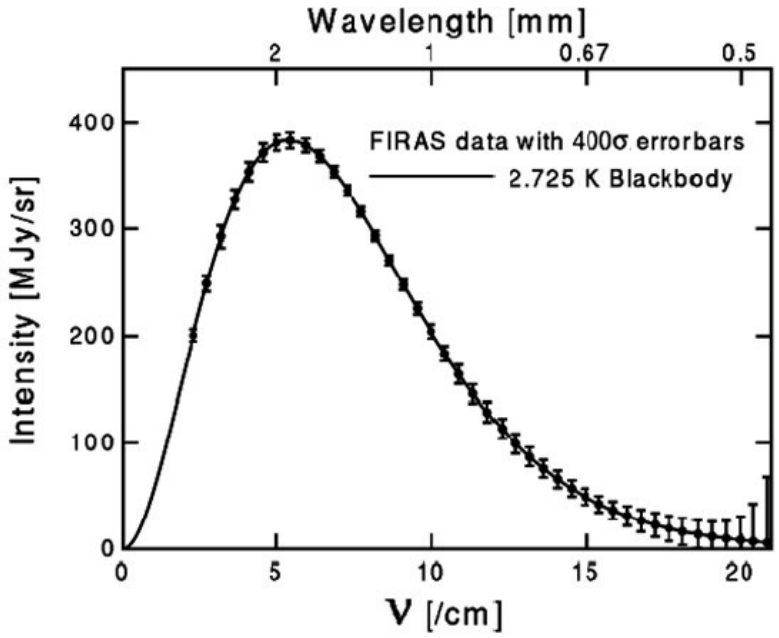

Figure 1.1: Data from the FIRAS instrument on the COBE satellite plotted over a temperature spectrum of a blackbody with a temperature of 2.725 K. The error bars have been increased by a factor of 400 to be visible. From http://planck.caltech.edu

(1) Within the photon-baryon plasma two effects compete: gravitational attraction favors condensation of baryons while photon pressure tends to homogenize densities. The interplay of both effects creates oscillations (like sound waves, hence the label *acoustic*). When photons decouple at recombination, a characteristic peak structure is imprinted in the spectrum of anisotropies. The (angular) location of the peaks gives significant information on different aspects: on the curvature, on baryon density or on the nature of the primordial density perturbations[7] (isocurvature or adiabatic).

(2) Collisionless or diffusion damping is the diffusion of photons from hot, overdense regions, to cold, underdense ones, which tends to smooth out density variations. The finite depth of the LSS (recombination is not instantaneous) also contributes to this phenomenon.

Secondary, or late-time anisotropies, have a different origin. While one expects, after recombination, that CMB photons propagate undisturbed in the resulting neutral medium, observations of galaxies indicate that the intergalactic medium is, on the contrary, ionized. This is due to a *reionization* period, that we will address in Section 1.5.3. Scattering of photons with the charges in this medium (a) erases anisotropies (on small scales) and (b) introduces polarization. Two additional effects may also cause anisotropies, the Sunyaev-Zel'dovich effect (scattering of CMB photons by high energy electrons) and the Sachs-Wolfe effect (gravitational redshift/blueshift in varying gravitational fields); a detailed description of them is beyond the scope of this summary.

The pre-galactic gas was very strongly coupled to the background radiation by Thomson scattering. Indeed, because of the Thomson scattering of the background radiation, we cannot obtain any direct information on what was going on at early epochs, we can only observe the very surface layers at which the Universe became transparent to radiation, that is the LSS, whose fluctuations, observed by COBE, are interpreted as the very low intensity "small waves" present on that surface on angular scales of 7° and larger. These "small waves" grow under gravity and will eventually define some of the very largest scale structures in the local Universe. Figure 1.2 shows the current CMB radiation temperature sky map obtained by the Planck collaboration.

[7]The origin of density perturbations, in other words, the fact that there are primordial perturbations at all, and their characteristics, is a different question. In Section 1.7 we will mention how inflation, which initially addresses other problems of the standard cosmological model, can also accommodate primordial perturbations.

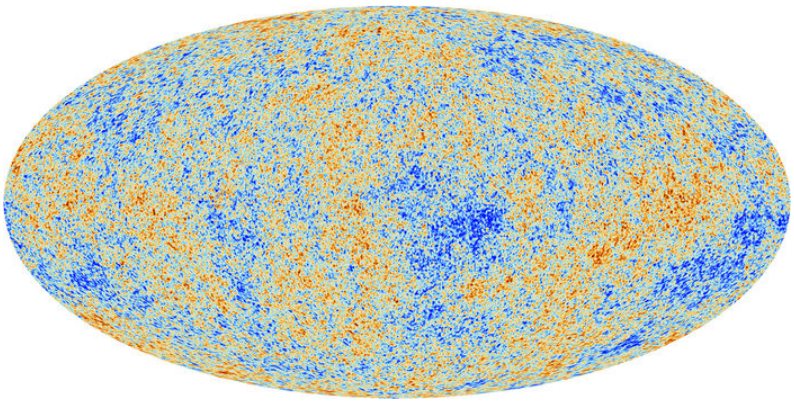

Figure 1.2: Cosmic Microwave Background seen from Planck. From http://www.esa.int/

1.5.2 The Structure Formation

As the Cosmological Principle states, the Universe is homogeneous on sufficiently large scales; nevertheless, on small scales, it is rather inhomogeneous, for example, in clusters of galaxies the average density is about 10^2-10^3 times the cosmic average density, while in single galaxies the average density is even larger, about 10^5 times the average density of the Universe. Even though galaxies and clusters of galaxies are complex systems, cosmology describes their arisal through two ingredients: (1) primordial inhomogeneities typically coming from the inflationary period (that we address in Section 1.7), (2) evolution of such inhomogeneities, at a later stage, depending on the interplay between gravitational attraction and pressure. In other words, the primordial inhomogeneities in (1) provide the initial conditions for the dynamical evolution given by (2). In particular, if in some region there is a small overdensity $\delta\rho$ over the average background density ρ, $\delta\rho \ll \rho$, it may grow to $\delta\rho \sim \rho$ and evolve towards bound structures in which star formation and other astrophysical processes lead to formation of galaxies and clusters of galaxies as we know them.

The isotropy of the CMB radiation implies a very smooth Universe at recombination, with energy density perturbations $\frac{\delta\rho}{\rho} \ll 1$. This justifies adopting a linear, perturbative approach, to describe a significant part of their evolution.

In Appendix A, we review the classical Newtonian treatment of gravitational instabilities due to Jeans, including its extension to an expanding Universe. This classical picture illustrates much of the physics relevant to understand the evolution of density perturbations.

The dark matter component is the protagonist of structure formation: following a

process known as *hierarchical structure formation model*, small pieces of DM start to conglomerate and build larger structures. That is, smaller clumps begin to merge and become larger. Ordinary (baryonic) matter follows. This hierarchical structure of conglomerations of DM is a non-linear process and it needs to be simulated using N-body simulations: numerical dynamical simulations where systems with a large number of clumps evolve under the influence of gravity. The results of N-body simulations suggest that, in the Universe, dark matter condenses in large filaments and haloes which have an intricate structure similar to a web.

The formation of these structures sets limits on the nature of DM. The scale of the structures is controlled by the collisional damping, by the kinetic decoupling and by the free-streaming length, $\lambda_{\rm fs}$, the mean distance particles travel between interactions. For example, a DM particle with a larger free-streaming length can stream out of regions with overdensities and erase structures smaller than a given scale. Light particles, as for example Standard Model neutrinos with mass $m_\nu < 6$ eV,[8] are characterized by a free-streaming length of the order of $\lambda_{\rm fs} \sim 100$ Mpc. It means that if all DM in the Universe had been formed by only Standard Model neutrinos, the typical size of the resulting structures would correspond to galaxy superclusters. In that kind of scenario, the hierarchical structure formation, rather than bottom-up, would be *top-down*: supercluster-scale structures would form first and then, by fragmentation, smaller objects as galaxies would form later. On the contrary, a WIMP DM, like for example a supersymmetric neutralino, has a small $\lambda_{\rm fs}$ and, consequently, can form smaller bound objects. In this case, the minimum size of the DM bound structure is within 10^{-11} to $10^2 {\rm M}_\odot$, and it is set by the collisional damping and free-streaming [23, 24],[9] as we will see in Chapter 4.

1.5.3 Reionization

The dark ages of the Universe end when the first stars and galaxies start to form. These objects begin to emit ultraviolet radiation building up ionized regions in the surrounding environments. The amount of ionized gas in the Universe increases until the hydrogen is completely ionized. The period is known as the epoch of Reionization. Observations of the CMB, spectra of distant quasars, the studies of the 21-cm line in hydrogen, and other cosmological probes, indicate that the intergalactic medium

[8] The most stringent limit on the neutrino mass, is related to the anti-electron neutrino mass from Tritium decay experiment, gives $m_{\bar{\nu}_e} < 2.0$ eV [22]. If combined with the largest of the mass difference between the three neutrinos, i.e. $\Delta m_\nu \sim 0.05$ eV [22], it is possible to derive an upper bound on the sum of the neutrino masses of $m_\nu \lesssim 6$ eV.

[9] The primordial spectrum of density fluctuations in neutralino CDM has a sharp cut-off due to two damping mechanisms: collisional damping during the kinetic decoupling of the neutralinos and free streaming after last scattering of neutralinos.

(IGM) went towards a phase, at redshift $z \approx 10$, in which most of the atomic hydrogen of the Universe was reionized. By studying the Gunn-Peterson effect, that is the absorption trough observed in the spectra of quasars at frequencies higher than those Lyman-α [26], it has been possible to know that the fraction of ionized hydrogen between redshifts $z = 5.5$ and $z = 6$, has experienced a rapid increase. On the other hand, CMB measurements indicate that 9%, approximately, of the CMB photons were scattered by free electrons after the recombination epoch, confirming that the reionization of the Universe happened at $z \approx 10$.

1.6 Λ (or Dark Energy) Dominated Epoch

In the two last decades a set of cosmological observations led to a new cosmological scenario. There was an improvement in the measurement of the anisotropies of the CMB, and the expansion rate of the Universe was measured using distant *Supernovae Type Ia* (SN Ia). In 1998, two independent groups [27, 28] observing the luminosity of Supernovae type Ia, reported that the Universe is in a phase of accelerated expansion, indicating the presence of a cosmological constant that contributes about 70% of the present energy density. Supernova data, combined with other different cosmological datasets, lead to a a description in which there is a negative pressure fluid, coined *Dark Energy* (DE), that is the dominant component in the energy density of the Universe, driving its dynamics nowadays.
The cosmological constant, Λ, is the simplest candidate for the dark energy because it is characterized by a constant energy density in both space and time, and has an equation of state with $\omega = -1$.

In Section 1.2 we have seen the Einstein equations, where $G_{\mu\nu}$ is the Einstein tensor that satisfies the Bianchi Identities $G^{\mu}_{\nu\,;\mu} = 0$, in such a way that the conservation of the energy-momentum tensor $T^{\mu}_{\nu\,;\mu} = 0$ is automatically verified. Since the metric tensor $g_{\mu\nu}$ is constant with respect to covariant derivation, there is freedom to add terms proportional to $g_{\mu\nu}$ without violating that conservation law. Then, the Einstein equation given in equation (1.10) can be modified to:

$$R_{\mu\nu} - \frac{1}{2}\mathcal{R}\, g_{\mu\nu} + \Lambda\, g_{\mu\nu} = 8\pi G T_{\mu\nu}\,, \tag{1.117}$$

where Λ is a constant. For a FLRW metric, the modified Einstein equation gives:

$$H^2 = \frac{8\pi G}{3}\,\rho - \frac{K}{a^2} + \frac{\Lambda}{3}\,, \tag{1.118}$$

$$\frac{\ddot{a}}{a} = -\frac{4\pi G}{3}(\rho + 3p) + \frac{\Lambda}{3}\,. \tag{1.119}$$

Equation (1.119) shows that Λ acts as a repulsive force, opposing gravity.

1.7 A short digression: Inflation

The standard Big Bang model sketched to this point, suffers from problems related to its initial conditions.

- The *horizon problem*: even if different regions of the Universe were not in causal contact with each other, at some point in the very early Universe, they had the same temperature.
- The *flatness problem*: observations indicate that the current total energy density in the Universe is $\Omega_0 = 1$, but, if the Universe was closed or open during its early stages, it should have departed from $\Omega_0 \sim 1$ rapidly, since:

$$(\Omega - 1)_{RD} = (\Omega_i - 1)\left(\frac{t}{t_i}\right)^{2/3}, \tag{1.120}$$

$$(\Omega - 1)_{MD} = (\Omega_i - 1)\frac{t}{t_i}, \tag{1.121}$$

  during radiation (RD) and matter (RM) domination, respectively, and for an open or a closed Universe.

In 1981, Alan Guth understood that the horizon and flatness problems could be solved by an early phase of exponential expansion of the Universe called *inflation*. The original model had problems in yielding an homogeneous and isotropic Universe, reheating and a radiation dominated epoch. Nevertheless, an accelerated expansion phase was soon recognized to be useful to explain the initial conditions of the Universe. Models without the problems of the original proposal followed (see e.g., [30, 31, 32]).
Inflation would explain the homogeneity and isotropy of the Universe starting from the fact that it has expanded from a small region that was in causal contact before inflation. We present some of the basic ideas, as a detailed account is beyond our scope. Initially particles were in causal contact with each other. Before the beginning of the inflationary expansion, the physical scale was smaller than the particle horizon, and the particles could be in a homogeneous state. With the exponential expansion due to inflation, the causally connected regions were threw out of their particle horizons. After the inflationary epoch, there was a release of a big amount of energy (phenomenon known as "reheating"), and the Universe entered the radiation dominated epoch, expanding as $a \propto t^{1/2}$. The exponential expansion drew the geometry of the inflated Universe towards flatness, $\Omega_k = 0$, yielding to the flatness problem.

The issue related to inflation is the question of primordial anisotropies mentioned in Section 1.5.1: the inflationary picture gives rise to primordial anisotropies due to tiny quantum fluctuations of the inflaton field

1.8 The Power Spectra of Fluctuations

1.8.1 The Angular Power Spectrum

Perturbations in the photons phase space distribution correspond to fluctuations in the cosmic microwave background radiation. In order to have information on how these anisotropies appear on the sky, we should obtain the *angular power spectrum*:

$$C_\ell = \langle |a_{\ell m}|^2 \rangle \,, \tag{1.122}$$

where $a_{\ell m}$ are the expansion coefficients of the temperature anisotropies in spherical harmonics and $\langle \ldots \rangle$ stands for an average. Since the CMB temperature fluctuations that we observe are defined on the last scattering surface, it is convenient to expand them in spherical harmonics; this is the analogue of a Fourier expansion for functions that live on the surface of a sphere.
The spherical harmonics are defined as:

$$Y_{\ell m}(\theta, \phi) = \sqrt{\frac{(2\ell+1)(\ell-m)!}{4\pi\,(\ell+m)!}}\, P_\ell^m(\cos\theta)\, e^{im\phi} \,, \tag{1.123}$$

where P_ℓ^m are the associated Legendre polynomials, and ℓ and m are integers such that $\ell \geq 0$ and $|m| \leq \ell$, and (θ, ϕ) are the usual spherical angles. These functions provide a complete orthonormal set on the unit sphere, where the orthonormality is

$$\int Y_{\ell m}(\theta, \phi)\, Y^*_{\ell' m'}(\theta, \phi)\, d\Omega = \delta_{\ell \ell'} \delta_{m m'} \,, \tag{1.124}$$

and completeness means that we can expand any square-integrable function Δ as

$$\Delta(\theta, \phi) = \sum_{\ell=0}^{\infty} \sum_{m=-\ell}^{\ell} a_{\ell m}\, Y_{\ell m}(\theta, \phi) \,. \tag{1.125}$$

The expansion coefficients $a_{\ell m}$ are defined as

$$a_{\ell m} \equiv \int Y^*_{\ell m}(\theta, \phi)\, \Delta(\theta, \phi)\, d\Omega \,. \tag{1.126}$$

In our case $\Delta(\theta, \phi)$ will be the temperature fluctuation:

$$\Delta(\theta, \phi) \equiv \frac{T(\theta, \phi) - \langle T(\theta, \phi) \rangle}{\langle T(\theta, \phi) \rangle} \,. \tag{1.127}$$

In terms of the unit vector $\hat{n} = (\sin\theta, \cos\phi, \sin\theta \sin\phi, \cos\theta)$, equation (B.14) can be rewritten as

$$\Delta T(\hat{n}) \equiv \frac{T(\hat{n}) - \langle T(\hat{n}) \rangle}{\langle T(\hat{n}) \rangle} \,, \tag{1.128}$$

where $T(\hat{n})$ is the CMB temperature observed in the sky in the direction $\hat{n}$.
Experimentally, observing the sky in two directions $\hat{n}$ and $\hat{n}'$, separated by an angle θ (that is $\hat{n} \cdot \hat{n}' = \cos\theta$), and averaging over all pairs $(\hat{n}, \hat{n}')$ with the same $\hat{n} \cdot \hat{n}' = \cos\theta$, we obtain the *two point correlation function*, $C(\theta)$,

$$C(\theta) = \langle \Delta T(\hat{n}) \, \Delta T(\hat{n}') \rangle \,. \tag{1.129}$$

Using the expansion in spherical harmonics of $\Delta T(\hat{n})$, together with

$$\langle a_{\ell m} \, a_{\ell' m'} \rangle = \delta_{\ell \ell'} \, \delta_{m m'} \, C_\ell \,, \tag{1.130}$$

and the addition theorem

$$\sum_{m=-\ell}^{\ell} Y^*_{\ell m}(\hat{n}) Y_{\ell m}(\hat{n}') = \frac{2\ell + 1}{4\pi} \, P_\ell(\hat{n} \cdot \hat{n}') \,, \tag{1.131}$$

equation (1.129) can be rewritten as:

$$C(\theta) = \sum_\ell \frac{2\ell + 1}{4\pi} \, C_\ell \, P_\ell(\cos\theta) \,. \tag{1.132}$$

C_ℓ is known as the *angular power spectrum.*

During the last decade, a large amount of experiments have measured the small and the large angular temperature fluctuations of the CMB, detecting a series of acoustic peaks in the anisotropy power spectrum, that are relevant before recombination.

The characteristics of such peaks are sensitive to the value of the cosmological parameters, in particular to Ω_{tot}, Ω_b and the scalar spectral index n_s. Therefore, the CMB power spectrum provides information on combinations of fundamental cosmological parameters.

As mentioned previously, before recombination, the baryons in the Universe were coupled to the photons of the CMB via Thomson scattering. Photon pressure, opposing the gravitational collapse of matter, produced sound waves in the plasma (composed by these two coupled fluids: baryons and photons). After recombination, baryons and photons separated, but the effects of the acoustic oscillations remained imprinted in the spatial structure of the baryons and, eventually, on dark matter. This phenomenon is known as *Baryonic Acoustic Oscillations* (BAO), and was seen in 2005 by the Sloan Digital Sky Survey (SDSS) [33] and 2dFGRS [34], and later was detected by other surveys (see, e.g. [35, 36, 37]). The typical lengthscale of the acoustic oscillations depends on the sound horizon of the Universe at the epoch of recombination. The sound horizon is the comoving distance that a sound wave can travel before recombination, and it depends only on the matter density. The relative heights of the acoustic peaks in the CMB anisotropy power spectrum measure this density with excellent accuracy (see [38] for further details).

Figure 1.3 displays the CMB temperature anisotropies $D_\ell = \frac{C_\ell}{2\pi}\ell(\ell+1)$ versus the multipole ℓ, in which the curve represents the theoretical prediction of the angular power spectrum, and the points are data measured by the Planck satellite.

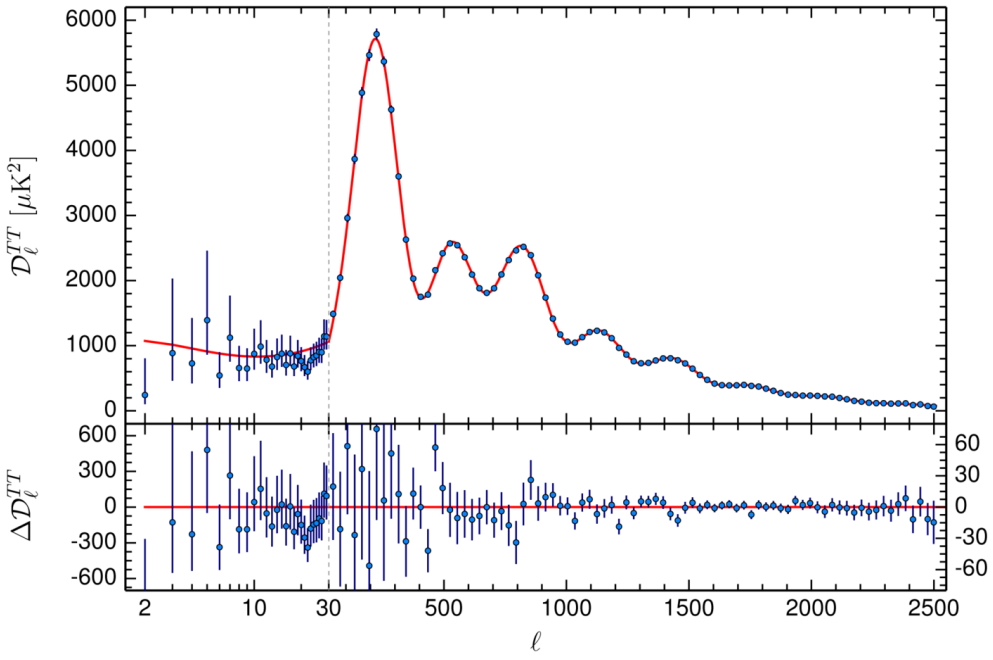

Figure 1.3: Planck CMB temperature anisotropy power spectrum [6].

1.8.2 The Matter Power Spectrum

As discussed in Section 1.5.2, after recombination of the hydrogen atoms and the release of the CMB, the Universe enters a period known as the *dark ages*, in which the potential wells seeded by dark matter start attracting the baryons. Baryonic matter, since Thomson scattering has ceased, can collapse gravitationally, forming what will later become the first galaxies and stars.
The evolution of small density perturbations

$$\delta(\vec{x},t) = \frac{\rho(\vec{x},t)}{\bar{\rho}} - 1\,, \tag{1.133}$$

with $\bar{\rho}$ the average density of the Universe, under the influence of gravity, is described in appendix A. The standard (statistical) study of the properties of these perturbations concentrates on two observables:

- **The correlation function**

  $$\xi(\vec{r}) = \langle \delta(\vec{x}+\vec{r})\delta(\vec{x}) \rangle\,, \tag{1.134}$$

  where the average $\langle \cdots \rangle$ is taken over the entire statistical ensemble of points $\vec{x}$, and $\vec{r}$ is the comoving distance from the point $\vec{x}$.

- **The matter power spectrum**
  It is defined as the Fourier transform of the correlation function $\xi(\vec{r})$:

  $$P(\vec{k}) = \int d^3r\, \xi(\vec{r})\, e^{i\vec{k}\cdot\vec{r}}, \tag{1.135}$$

  that is:

  $$P(\vec{k}) = (2\pi)^{-3} \langle \delta_{\vec{k}} \delta^*_{\vec{k}'} \rangle\,. \tag{1.136}$$

where $\vec{k}$ is the comoving wave number associated with a given mode.

In the case of an isotropic and homogeneous distribution, the correlation function, ξ, is only a function of $r = |\vec{r}|$, in such a way that $\xi(\vec{r}) = \xi(|\vec{r}| = r)$. In the case of a Poissonian distribution, $\xi(r) = 0$; but it is not the case for the distribution of matter in the Universe, because of the clustering effects of gravity.
If the density fluctuations δ follow a Gaussian distribution, the power spectrum gives a complete statistical description of the fluctuations.

The matter power spectrum measured today comes from the time evolution of a primordial power spectrum (typically generated by inflation, as mentioned in Section 1.7). Most (inflation) models predict a simple power law spectrum of perturbations:

$$P(k) = k^n\,, \quad n \approx 1 \quad \text{(primordial)}\,, \tag{1.137}$$

where n is the *scalar spectral index*. For $n = 1$ (Harrison-Zel'dovich spectrum) the power spectrum is said to be scale invariant; it means that the gravitational potential fluctuations have the same amplitude over all scales when they enter the horizon. Nevertheless, this primordial shape changes and develops as the Universe evolves. A particular transition takes place at matter-radiation equality, developing a small-scale shape:

$$P(k) = k^{n-4}\,, \quad \text{(small-scale)}\,. \tag{1.138}$$

In general, physical processes affecting sub-horizon perturbations (like self-gravity, pressure support and damping processes) will determine a modification of the form of the primordial power spectrum, expressed by the transfer function $T(k, z)$, that describes the evolution of perturbations from the inflationary era to the matter-radiation equality, in the following form:

$$P(k, z) = A(z)\, k^n\, T(k, z)\,, \tag{1.139}$$

where the normalization $A(z)$ is determined observationally.

For large scales, the spectrum has the inflationary shape $P(k) \propto k^n$, because large scale modes are observed when they were not in causal contact, or when they entered the horizon during the matter dominated epoch. In each case, only gravitational processes have a role, and the transfer function is approximately $T(k, z) = 1$.
On small scales, the matter power spectrum turns over, because smaller scale modes enter the horizon during the radiation dominated epoch. The large expansion rate determined by photons prevents the growth of structures until the matter dominated epoch is reached. It means that smaller modes enter the horizon earlier, and undergo more suppression. This causes a decrease in the matter power spectrum as, on small scales, the value of k increases.
The turn-over of the power spectrum corresponds to the scale of the horizon at the matter-radiation equality.
The matter power spectrum depends, generally, on various matter components in the Universe which are able to cluster, like cold dark matter, baryons and massive neutrinos, each one with its own transfer function. Cold dark matter starts to grow appreciably after the matter-radiation equivalence, while baryonic and collisional matter are strongly coupled to radiation and oscillate until the decoupling epoch, at $z \sim 1100$, when the baryonic Jeans mass falls by several orders of magnitude, so baryons can follow the same evolution as dark matter. Then, during the recombination epoch, the mean free path of photons increases, determining a smearing of the fluctuations in the baryon distribution. Another relevant quantity is the amount of dark energy.[10]
The large scale structures of the Universe begin to form when the pressure due to

[10] We remind the reader that, working in a flat Friedmann-Lemaître-Robertson-Walker background, the total energy density of the Universe is $\Omega_\Lambda + \Omega_m = 1$. This means that the matter power spectrum also depends on the amount of dark energy today: different values of the density parameter of dark

photons becomes smaller than the gravitational force due to the non-relativistic matter; this occurs after matter-radiation equality. Therefore, matter-radiation equality sets the position of the peak in the matter power spectrum: the wavenumber k_{eq}, where the sub-index *eq* stands for *equality*, separates the "large scale" from the "small scale" modes.

In Figure 1.4 we show illustrative matter power spectrum data.

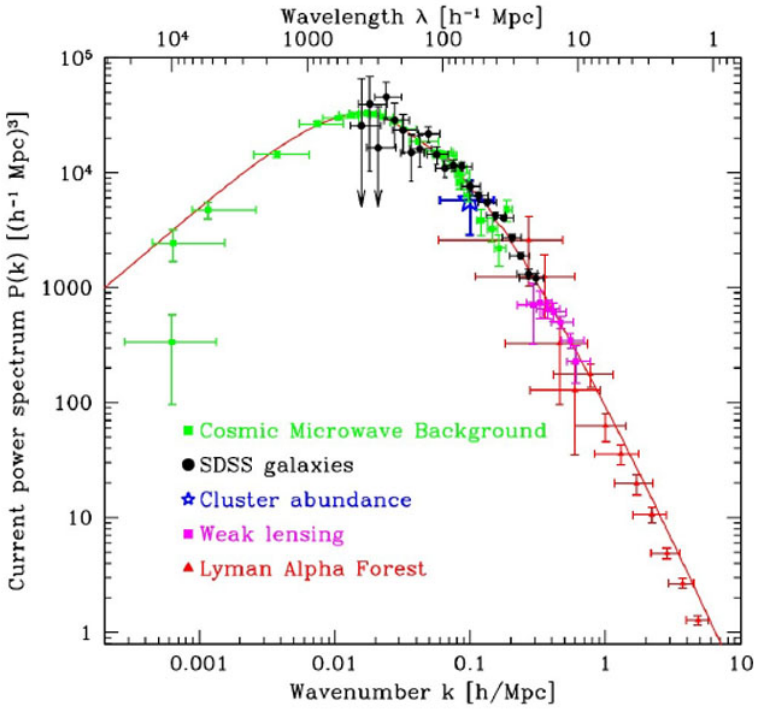

Figure 1.4: Linear matter power spectrum $P(k)$ versus the wavenumber k extrapolated to $z = 0$, from various measurements of cosmological structure. From [39].

energy, Ω_Λ, determine different values for the density parameter of matter, Ω_m, which determines matter-radiation equivalence and thus the turn-over scale of the matter power spectrum.

2 Dark Matter Properties

In the previous Chapter, dark matter has been introduced with no particular emphasis on the empiric motivations supporting its existence. Section 2.1 reviews some of the strongest points that make us *know* that dark matter *exists*. In Section 2.2 we explore some of the most popular particle physics candidates for dark matter. Dark Radiation, that is the possibility that some dark matter is relativistic instead of cold, is discussed in Section 2.3. To address where and how dark matter *is*, the properties of dark matter halos are presented in Section 2.4. To close this Chapter, Section 2.6 is devoted to the different dark matter detection methods.

2.1 Dark matter evidences

The fact that DM does exist is solid and very well motivated by several observations. In the following we present some of the most persuasive cosmological and astrophysical phenomena requiring the existence of DM.

- **Galaxy rotation curves**
  The earliest evidence for DM at galactic scales comes from the observation that luminous objects (stars, gas clouds) have larger velocities than those expected if they only feel the gravitational attraction of other visible matter. This anomalous behavior can be dramatically illustrated with the galactic rotation curves, i.e. representing rotation velocities of bound objects as a function of the distance from the galactic center. The rotational velocity of an object on a Keplerian

orbit with radius r is

$$v(r) \propto \sqrt{M(r)/r}\,, \tag{2.1}$$

with $M(r)$ is the galactic mass enclosed within radius r from the center. Therefore, for objects out to very large radii one would expect $v(r) \propto 1/\sqrt{r}$. Instead, the observations find that v becomes approximately constant out to the largest values of r where the rotation curve can be measured [40]. This implies that the baryonic matter alone cannot explain this result: the presence of unseen (dark) matter in the galaxy can account for it. As an illustrative example, figure 2.1 shows the velocity rotation curve of the galaxy NCG 6503 as a function of radial distance from its galactic center.

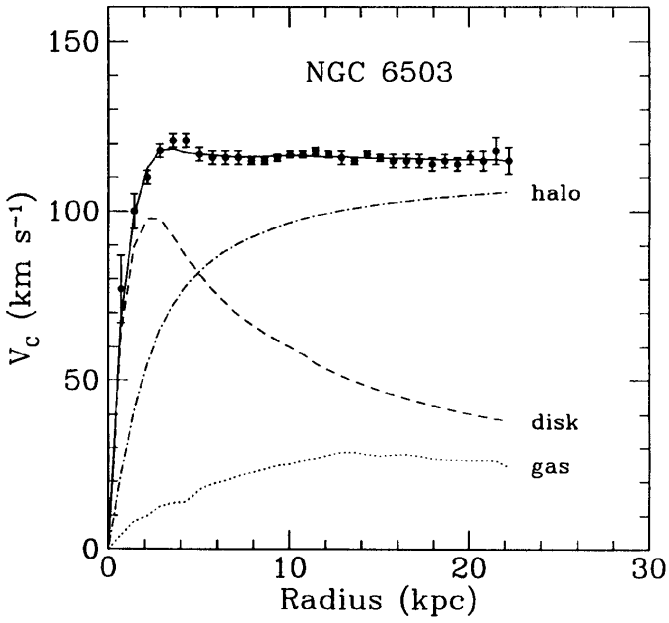

Figure 2.1: The rotation curve of galaxy NGC 6503. The dark matter halo contribution is shown by the dashed–dotted line. Points with error bars come from the 21–cm line of neutral hydrogen while the solid line is a model fitting the data from[40].

- **Cosmic Microwave Background**
  As anticipated in Section 1.8.1, the anisotropies in the Cosmic Microwave Background, in particular the characteristics of the peaks in the angular power spectrum (see Fig.1.3) provide sensitivity to the total energy density of matter: baryonic matter barely accounts for a small fraction of it ($\sim 1/8$).

- **Gravitational lensing**

In General Relativity light rays are deflected by gravity. The deflection of light by massive bodies is referred to as Gravitational Lensing; it solely depends on the projected, two–dimensional mass distribution of the lensing object. Furthermore, it is independent of the luminosity and composition of the lens [41]. Lensing offers an ideal way to detect and study dark matter through the mismatch between the amount of "lensing" matter and the amount of visible matter in the lens. The *Bullet Cluster* provides one of the most striking examples [42, 43]. In Fig. 2.2 the mass distributions reconstructed from Gravitational Lensing and from X–ray emitting hot gas in the Bullet Cluster can be seen: they are completely different.

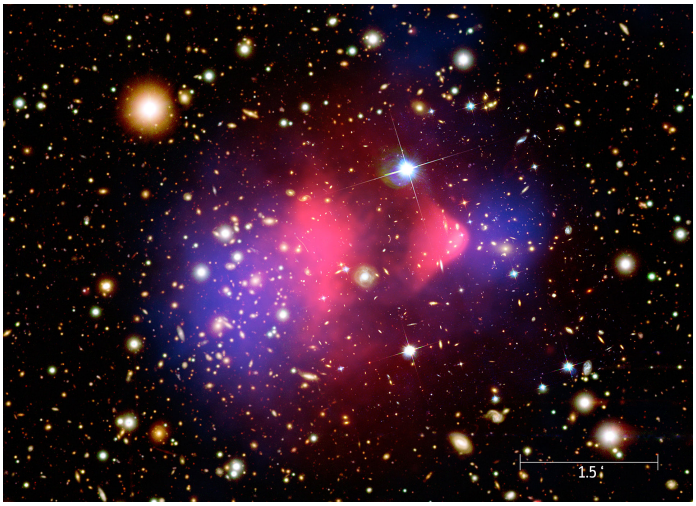

Figure 2.2: Reconstructed mass distributions: lensing (blue) and X–ray (red).

- **Structure formation**
  As anticipated in 1.5.2, the dark matter component has a central role in our understanding of the formation of structures. The pressure and temperature of the baryonic matter would prevent the formation of structures (for example stars) through the Jeans instability. On the other hand, dark matter can collapse gravitationally; with this additional attraction, baryonic matter can collapse as well, to form structures.

- **Velocity dispersion of galaxies**
  At scales of galaxy clusters, a strong evidence comes from the measurements of the peculiar velocities of galaxies. For a virialized cluster, they are a measure of their gravitational potential energy. The first analysis was performed by F. Zwicky in 1933 in the Coma cluster: it pointed to a large amount of inferred

unknown matter (which he labelled for the first time "dark matter").

- **Intracluster hot gas**
  Another evidence for dark matter in galaxy clusters is the existence of enormous amounts of hot gas in the intracluster medium. This implies that there should be a huge amount of non–luminous matter that provides the binding potential to hold on the gas there.

2.2 Dark Matter Candidates

Attending to the impressive amount of evidence in favour of the existence of dark matter, many efforts have been devoted to put forward plausible dark matter candidates with a fundamental particle physics nature. Supersymmetric scenarios, extra dimensions, extended scalar sectors, additional (sterile) neutrinos or axions, provide dark matter candidates with a wide range of characteristics and peculiarities. In this Section we sketch the basic properties of three different DM candidates: sterile neutrinos, axions and neutralinos.

2.2.1 Sterile neutrinos

In the formulation of the Standard Model of particle physics, neutrinos were originally considered massless: only left-handed neutrinos were introduced. Nevertheless, experiments have shown that neutrinos do have a tiny mass which is often interpreted as a motivation for beyond the Standard Model physics. Weak singlet right-handed neutrinos have no standard model charge and are thus called *sterile neutrinos*. Besides their use to provide neutrino masses, including the popular see-saw mechanism [44, 45], or their appearance in grand unification theories, sterile neutrinos could constitute dark matter. A number of constraints apply to this kind of scenario.

1. As a dark matter candidate, sterile neutrinos would not be completely dark: since they could mix with active neutrinos, radiative decays *sterile* $\nu \rightarrow$ *active* $\nu + \gamma$ could produce emission lines. The absence of such signals puts very stringent constraints on the sterile mass and the sterile-active mixing.

2. One can also obtain quite model independent constraints on the absolute mass of sterile neutrinos through their fermionic nature. Requiring that their degeneracy pressure (as a fermionic particle gas) does not give velocities larger than the escape velocity in massive dark matter dominated objects, for example the dwarf spheroidal satellites [46], imposes lower bounds on the sterile mass in the keV ballpark.

3. Since sterile neutrinos with keV masses may act as warm matter, their propagation may suppress the power spectrum below the characteristic free-streaming length. Studies on small scales, in particular analyses of Lyman-α emission lines [47], yield lower mass bounds at the keV level.

2.2.2 Axions

The original motivation for axions came from the strong CP problem. Although perturbative QCD is CP conserving (C stands for charge conjugation and P for parity), a topological "θ" term which violates CP can be added to the QCD Lagrangian. Experimental constraints like limits on the electric dipole moment of the neutron force the parameter controlling that CP violating term to be highly fine-tuned or suppressed. This is the *strong CP problem*. One solution proposed by Peccei and Quinn introduced a global $U(1)$ symmetry of QCD (without the topological "θ" term), spontaneously broken. The axion is the pseudo-Nambu-Goldstone boson linked to the $U(1)$ symmetry breaking; the strong CP problem is solved when the minimum of the effective potential is obtained for the value of θ which naturally produces the mentioned fine-tuning. It was later recognized that axions could be a dark matter candidate. While the original proposal was ruled out by particle experiments (typically through the constraints on the mixing of the axion with other neutral pseudoscalar particles like π^0 or η), there is a variety of axion models with motivations ranging from the strong CP problem (those are QCD-axions) to extensions of the standard model and string theory.

2.2.3 Neutralinos

Supersymmetry (SUSY) is one of the most popular ideas for physics beyond the Standard Model. SUSY is a symmetry which brings together the two basic types (according to their spacetime properties) of elementary particles, bosons and fermions, into multiplets. Many SUSY models have been considered in the literature with the Minimal Supersymmetric Standard Model, the MSSM, being the most widely discussed. Besides aesthetic motivations and its important role in string theories, the main motivations for having SUSY close to the electroweak scale are the following.

- The hierarchy problem: the sensitivity of the mass scale of electroweak symmetry breaking to physics at much larger energy scales through radiative corrections, would drag all the Standard Model particle masses to values of the high energy scale order, unless highly fine-tuned.
- When Supersymmetry is supplemented with an additional symmetry require-

ment, conservation of R-parity, the lightest supersymmetric particle (LSP) could constitute a dark matter candidate.

- Incorporating SUSY to Grand Unification Theories typically improves the unification of gauge couplings in the renormalization group evolution from low to high energies.

Further details on some of these aspects are addressed in Chapter 4; for the moment let us comment on the basics that allow SUSY to provide DM candidates. First, it is important to stress that SUSY should be broken. If it was not, supersymmetric companions of all known SM particles should exist with equal masses like, for example, a "scalar electron" with the same electron mass: there is no evidence of such particles, and SUSY should be broken. For that breaking not to spoil the solution of the hierarchy problem, it has to be introduced through "soft" terms (technically this means that the SUSY breaking terms only involve dimension 2 or 3 operators). SUSY would in principle allow baryon and lepton number violating interactions, leading for example to very fast proton decay, in clear contradiction with experiment. This problematic possibility can be tamed through the introduction of a discrete symmetry, R-parity, which essentially assigns $R = +1$ to SM particles and $R = -1$ to their superpartners. Since it is a discrete symmetry, it is multiplicatively conserved in interactions. Two important consequences follow. First, in production, supersymmetric particles should come in pairs. Second, in decays, heavier supersymmetric particles can only decay to lighter supersymmetric particles; it is then clear that the lightest supersymmetric particle, the *LSP*, has no valid decay mode: it has to be *stable*, providing a first interesting property for a viable DM candidate. Furthermore, among the available superpartners, several are electrically neutral: the sneutrino, the gravitino and neutralinos. The most popular DM candidate among them is the lightest neutralino. Neutralinos are neutral fermions, and there are four of them: the superpartners of the B and W_3 gauge bosons, and the superpartners of the two neutral scalar bosons in the two Higgs doublets (contrary to the SM, SUSY requires two Higgs doublets). They are not mass eigenstates, and which combination of them is the lightest depends on gauge couplings, on the pattern of electroweak symmetry breaking (the ratio of the vacuum expectation values of the two doublets, $\tan\beta$) and on the SUSY breaking gaugino mass terms. As a last comment, it is also clear that the lightest neutralino has weak interactions and thus fits well into the WIMP paradigm.

2.3 Dark radiation

Dark matter particles are non-relativistic at the current epoch. Nevertheless, the possibility that some dark matter fraction is relativistic today, can occur. This leads

to additional relativistic degrees of freedom generically known as *dark radiation*, to which we devote this short section.
The total energy density associated to relativistic degrees of freedom is

$$\rho_{rad} = \left[1 + \frac{7}{8}\left(\frac{4}{11}\right)^{4/3} N_{\rm eff}\right]\rho_\gamma = [1 + 0.227 N_{\rm eff}]\rho_\gamma \,, \tag{2.2}$$

where ρ_γ is the energy density of the CMB photons at temperature $T_\gamma = 2.725$ K and $N_{\rm eff}$ is an effective number of relativistic degrees of freedom. In the standard scenario, the predicted value is $N_{\rm eff} = 3.046$, corresponding to the three active neutrinos; it deviates from $N_{\rm eff} = 3$ due to non–instantaneous neutrino decoupling from the primordial photon–baryon plasma [49, 50].

Deviations of $N_{\rm eff}$ from its standard value may indicate, for example, that the thermal history of the active neutrinos is different from what we expect, or that additional relativistic particles are present in the Universe. A non–standard value of $N_{\rm eff}$ may affect the Big Bang Nucleosynthesis era [51, 52, 53], and the matter-radiation equality. A shift in the matter-radiation equality would cause a change in the expansion rate at decoupling, affecting the sound horizon and the angular scale of the peaks of the CMB spectrum, and altering the CMB spectrum by an increased Silk damping at small scales. Dark radiation models contain, apart from photons and the three standard active neutrinos, additional relativistic degrees of freedom, for example the sterile neutrinos or the axions introduced in Section 2.2. In order to parametrize their presence, it is usual to describe the extra dark radiation component as $\Delta N_{\rm eff} \equiv N_{\rm eff} - 3.046$, that is, the difference between the total dark radiation background and the effective number of light active neutrinos.

The dark radiation component is characterized, in general, by its clustering properties, namely an effective speed of sound and a viscosity (see, e.g. [54]):

- the rest frame sound speed $c^2_{\rm eff}$ which, being analogous to the sound speed of the baryon-photon plasma, controls the Jeans length and therefore the perturbation in the pressure-density of the fluid;
- the viscosity parameter $c^2_{\rm vis}$ of the dark radiation, which controls the relationship between velocity/metric shear and anisotropic stress, i.e. characterizes the degree of anisotropies in the fluid.

Despite the efforts devoted to put bounds in the extra radiation components, current results are compatible with the standard prediction of 3.046 [6, 55]. The most recent measurements from the Planck satellite, using both temperature and polarization, and from the Baryonic Acoustic Oscillations, give as best constraint $N_{\rm eff} = 3.04 \pm 0.18$ [6].

2.4 Dark Matter Halo Properties

As discussed in Section 1.5.2, dark matter has a central role in the formation of structures; gravitationally bound structures of dark matter are known as dark matter *halos*. In the following subsections we briefly describe some quantities characterizing the properties of DM halos: the density profiles, the concentration parameter and the halo mass function.

2.4.1 The density profiles

Numerical N-body simulations provide a trustworthy method of calculating the evolution of the DM distribution; they can provide robust predictions for the clustering of the DM component. Recent numerical simulations of only CDM, seem to indicate that the density distribution in individual halos can be described in the following forms:

$$\rho(r) = \frac{\rho_s}{(r/r_s)^\alpha (1 + r/r_s)^\beta}\,, \tag{2.3}$$

or

$$\rho(r) = \frac{\rho_s}{(r/r_s)^\alpha [1 + (r/r_s)^\beta]}\,, \tag{2.4}$$

where r is the radial coordinate, r_s is the scale radius, and ρ_s is set by the DM density at the scale radius. Setting $\alpha = 1$ and $\beta = 2$ in Eq. (2.3), we obtain the so–called Navarro, Frenk and White (NFW) profile [56, 57]. On the other hand, by setting $\alpha = \beta = 1.5$ in Eq. (2.4), we obtain the Moore profile [58]. The two expressions have the same behavior at large radius and they are both singular towards the center of the halo (the Moore profile, however, diverges faster than the NFW profile, see Fig. 2.3).

Recent works [60, 61, 62, 63, 64] have shown that a spherical Einasto profile as

$$\rho(r) = \rho_s \exp\left\{-\frac{2}{\alpha}\left[\left(\frac{r}{r_s}\right)^\alpha - 1\right]\right\} \tag{2.5}$$

gives a better description of spherical CDM halos with respect to the NFW profile.

In all cases, after fixing the values of the α and β parameters, different choices to characterize the profile are commonly used: one can use either ρ_s and r_s, or use the total halo mass M and the concentration parameter to be introduced in the following. Most studies of the evolution of structural parameters for CDM halos use a NFW profile: this will be, for example, the choice in Chapter 4.

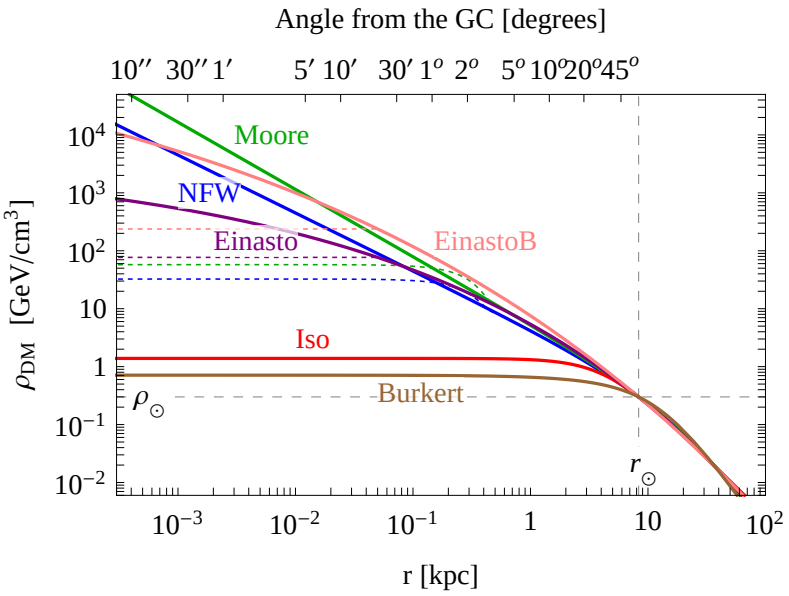

Figure 2.3: Halo dark DM for different halo profiles. (From [59]).

2.4.2 The concentration parameter

The concentration parameter, c, is a parameter that measures the concentration of dark matter in a halo. It depends both on the halo mass and redshift and it is related to the value of the background density when the halo forms: small mass halos have larger values of c than large mass halos since they form earlier [65]. The behavior of c as a function of M has been extensively studied (see, e.g., [65, 66] and references therein).

The concentration parameter can be determined in two ways from N–body simulations:

- By fitting the density profiles of the resolved halos with a given profile and obtaining the virial radius R_Δ and the scale radius r_s: then, the concentration parameter is defined as the ratio between the virial radius and scale radius of a halo (see, e.g., [65, 56, 57]):

$$c_\Delta = \frac{R_\Delta}{r_s}\,. \tag{2.6}$$

- By relating the ratio of the maximal circular velocity $V_{\max}$ and the virial velocity to a concentration parameter dependent expression computed from the density profile, and extracting numerically c from that relation, as in [67, 66].

Even if these methods give similar results at low redshifts, the second gives higher concentrations (at the $\sim 15\%$ level) at high masses and redshifts [66, 63].

2.4.3 The halo mass function

The halo mass function is the differential number density of dark matter halos per unit mass, dn/dM. The halo mass function is determined through N–body simulations and analytical models to interpret them. For example, Press and Schechter (PS) [68] made the first analytical approach assuming that the fraction of mass contained in halos which have larger mass than a given value, is connected with the fraction of the volume over which the background initial density is larger than a given threshold.

In the PS theory, the fraction of the Universe which condenses into objects with mass larger than the halo mass M, can be written in the universal form:

$$\nu f(\nu) = \frac{1}{\sqrt{2\pi}\sigma} \int_{\delta_{sc}}^{\infty} d\delta \exp\left(-\frac{\delta^2}{\sigma^2}\right) = \frac{1}{2}\mathrm{erfc}\left(\frac{\nu}{\sqrt{2}}\right) , \tag{2.7}$$

where $\nu \equiv \delta_{sc}/\sigma(M)$. δ_{sc} is the critical overdensity which corresponds to collapsed regions (the sub-index *sc* stands for *spherical collapse*), and $\sigma(M)$ is the root mean square (rms) density fluctuation, in linear theory, in spheres containing a mean mass M. By differentiating Eq. (2.7) with respect to the mass M, and then by multiplying it by $\bar{\rho}/M$, where $\bar{\rho}$ is the mean density, one obtains the mass function of halos:

$$\frac{dn}{dM} = \frac{\bar{\rho}}{M} f(\nu) \left(\frac{d\nu}{dM}\right) . \tag{2.8}$$

where n is the halo number density. The physics of halo collapse, including the dependence on δ_{sc}, is encoded in the function $f(\nu)$ (see, for example, [69]).

2.5 Dark matter substructures properties

In Section 1.5.2 we have mentioned that structure formation proceeds hierarchically, with low–mass halos forming first and then larger–mass halos resulting from the merging and accretion of those smaller halos. Traditionally, N–body cosmological simulations have also been used to study DM self–bound substructures, also called *subhalos*. The study of both the statistical and structural properties of the subhalo population is of prime importance because subhalos represent important probes of the mass accretion history and dynamics of more massive DM halos, called *host halos*, and thus of the underlying cosmological model. During the last years improved N–body cosmological simulations have been crucial for understanding the properties of substructure within a galaxy (as our Milky Way, for example) in a ΛCDM Universe.

As already mentioned, DM density profiles are fixed in terms of a few parameters. For example, if the DM profile is a NFW, the internal structure of a halo can be determined by the halo mass and the halo concentration. However, for a subhalo, the functional form for the concentration–mass relation, $c_{sub}(M_{sub})$, is not yet known, since it is difficult to define such subhalo concentrations with the simulations. There are two main reasons for which describing the structural properties of a subhalo is not straightforward:

1. the definition of the subhalos virial radius is not well known. The reason is due to the tidal stripping that removes mass from the external parts of subhalos and, as a consequence, with respect to halos of the same mass, subhalos are truncated at smaller values of the radius [70, 71];

2. present simulations are not able to resolve the inner profile at small radius inside the main halo.

For this purpose, if the concentration parameter is derived by the maximum of the circular speed (see Section 2.4.2) instead of the definition in Eq. (2.6), it will not depend on the density profile. So, the concentration parameter can be written [70, 71, 72] as the mean physical density $\bar{\rho}$ in a region of radius R_{max} (such that at R_{max} the peak circular velocity V_{max} is attained), over the critical density of the Universe today ρ_c (as defined in Eq. (1.14)),

$$c = \frac{\bar{\rho}(R_{max})}{\rho_c} \,. \tag{2.9}$$

The numerator in Eq. (2.9) is defined as

$$\bar{\rho}(R_{max}) = \frac{3}{4}\frac{M(R_{max})}{\pi R_{max}^3} = \frac{3}{4}\frac{V_{max}^2}{\pi G R_{max}^2} \,, \tag{2.10}$$

where[1] we have written the mass $M(R_{max}) = V_{max}^2 R_{max}/G$, with G the gravitational constant. Replacing the expressions for ρ_c and $\rho(R_{max})$ in Eq. (2.9), the concentration parameter reads

$$c = 2\left(\frac{V_{max}}{H_0 R_{max}}\right) \,, \tag{2.11}$$

in such a way that c is directly obtained from numerically simulated halos, independently of a given density profile.

On the other hand, it is posible to convert between c_Δ in Eq. (2.6) and c in Eq. (2.11). Since the circular velocity is $V_c^2(r) = GM(r)/r$, for a NFW density profile we have

$$M(r) = \int \rho(r) 4\pi r^2 dr = 4\pi\rho_s r_s^3 f(r) \,, \tag{2.12}$$

[1] We have used $F \propto GM/r^2$, and the centrifugal force, $F_c \propto v^2/r$.

and thus:

$$V_c^2(r) = 4\pi G \rho_s r_s^3 \frac{f(r)}{r}\,, \tag{2.13}$$

with

$$f(r/r_s) = \ln(1 + r/r_s)\frac{r/r_s}{1 + r/r_s}\,. \tag{2.14}$$

The maximum value of V_c, V_{max}, for a NFW halo is at [73]

$$R_{max} = 2.163\, r_s\,. \tag{2.15}$$

From Eq. (2.13), the ratio between the maximum velocity V_{max} and the circular velocity at the virial radius, V_Δ, reads

$$\left(\frac{V_{max}}{V_\Delta}\right)^2 = \frac{f(R_{max}/r_s)}{f(R_\Delta/r_s)}\,\frac{R_\Delta}{R_{max}} = \frac{f(R_{max}/r_s)}{f(c_\Delta)}\,\frac{c_\Delta}{2.163}\,, \tag{2.16}$$

where in the last equality we used Eq. (2.6) and Eq. (2.15). In addition,

$$V_\Delta^2 = \frac{G M_\Delta}{R_\Delta}\,, \tag{2.17}$$

with M_Δ the mass enclosed in a spherical region of radius r_Δ,

$$M_\Delta = \frac{4\pi}{3} R_\Delta^3 \Delta\, \rho_c\,, \tag{2.18}$$

and Δ the overdensity with respect to the critical density ρ_c (or, alternatively, with respect to the mean density $\bar{\rho}$, depending on the chosen convention).[2] Combining Eqs. (2.15) and (2.18), we find that the relation of c_Δ and c for a NWF density profile is given by:

$$c = \left(\frac{c_\Delta}{2.163}\right)^3 \frac{f(2.163)}{c_\Delta}\,\Delta\,. \tag{2.19}$$

2.6 Methods for dark matter detection

In Section 2.1 we have given a short account of the abundant and convincing evidence in favour of the existence of dark matter: gravity is a central ingredient in all cases. On the other hand, as discussed in Section 1.4.2 concerning the dark matter relic density in the WIMP case, interactions in addition to gravity have an important role, more so when particle physics candidates for DM are considered. This opens additional challenging avenues to probe its nature. Figure 2.4 summarises them diagramatically.

[2] It is common to define halos either with a reference value $\Delta = 200$ for the overdensity, or through the virial overdensity assuming spherical collapse [74].

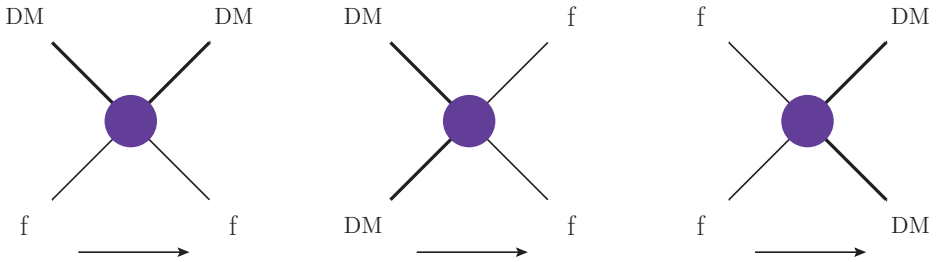

(a) DM Direct Detection (b) DM Indirect Detection (c) DM Production

Figure 2.4: dark matter probes.

In this Section we will briefly present these three different methods to detect DM.

- Direct detection experiments look for signals of scattering of DM off target nuclei, represented in Fig. 2.4(a), like for example energy deposition in underground detectors.
- Indirect detection looks for signatures of DM annihilation, represented in Fig. 2.4(b), such as gamma-ray emission, from dense celestial environments.
- Finally, as represented in Fig. 2.4(c), it could be possible to directly produce DM in facilities such as the Large Hadron Collider (LHC).

2.6.1 Direct detection

Direct DM searches try to detect DM particles by measuring nuclear recoils produced by DM scattering. This would be possible if our own Galaxy was filled with WIMPs as expected, since many of them would pass through the Earth and would weakly interact with ordinary matter, namely with SM particles. The key ingredients for the calculation of the signal in direct detection experiments are: 1) the density and the velocity distribution of WIMPs in the solar neighborhood, and 2) the WIMP–nucleon scattering cross section. From this information we can evaluate the rate of events expected in an experiment (i.e. WIMP–nucleon scattering events) per unit time and per unit detector material mass. The expected number of DM-nucleon scattering events per nuclear recoil energy dN/dE_r, in a given detector is given by [75]:

$$\frac{dN}{dE_r} = \frac{\rho}{m_N m_{dm}} \int_{v_{min}}^{\infty} v f(\vec{v} + \vec{u}_e) \frac{d\sigma}{dE_r} \, d^3v \,, \tag{2.20}$$

where m_N is the mass of the nucleus in the detector, m_{dm} is the DM particle mass, ρ is the local DM density, $v_{min} = \sqrt{E_r m_N / 2\mu_N^2}$ [3] is the minimun velocity necessary to produce a recoil of energy E_r, and $d\sigma/dE_r$ is the differential interaction cross–section. The distribution of DM particle velocities in the Galaxy is given by $f(v)$. Since the velocities in Eq. (2.20) are in the Earth's rest frame, u_e boosts this distribution of galactic DM velocities into the correct frame.

The interaction between WIMPs and the nuclei is divided into two components: *spin-dependent* (SD) and *spin-independent* (SI):

$$\frac{d\sigma}{dE} = \frac{d\sigma_{SD}}{dE} + \frac{d\sigma_{SI}}{dE} \,. \tag{2.21}$$

The SD cross-section is a function of the total nuclear spin of the nucleus J; there is a $J(J+1)$ enhancement from the nuclear spin J.

The SI cross-section is a function of the total mass of the nuclei; for a heavy nuclear target, the scattering increases the cross-section by the square of the atomic number A.

Assuming that the SI scattering cross–section is given by [76, 77]:

$$\frac{d\sigma}{dE_r} = \frac{\sigma_0 m_N F(E_r)}{2\mu_N^2 v^2} \,, \tag{2.22}$$

where σ_0 is the zero–momentum DM–nuclei cross–section and $F(E)$ the nuclear form factor, thus, the DM–nuclei recoil rate simplifies to

$$\frac{dN}{dE_r} = \frac{\sigma\rho}{2\mu^2 m_{dm}} F(E_r) \int_{v_{min}(E_r)}^{\infty} \frac{f(\vec{v}+\vec{u}_e)}{v} \, d^3v \,. \tag{2.23}$$

Assuming that the dark matter couples equally to protons and neutrons, the scattering cross–section between DM and nucleons is given by [76, 77]:

$$\sigma(E) = \sigma_0 \left(\frac{\mu_N}{\mu_p}\right)^2 A^2 \,, \tag{2.24}$$

where σ_0 is the zero–momentum DM–nucleon cross–section, μ_p is the DM–proton reduced mass, and A is the atomic number of the nucleus which DM interacts with.

On the other hand, if the DM–nucleus scattering is SD, i.e., if the DM couples to nuclei via their spin, instead of Eq. (2.22), the expression for the differential cross–section reads [78]:

$$\frac{dN}{dE_r} = \frac{16 m_N}{\pi v^2} \Lambda^2 G_F^2 \, J(J+1) \frac{S(E)}{S(0)} \,, \tag{2.25}$$

[3] μ_N is the DM–nucleus reduced mass defined as $\mu_N = m_\chi m_N / (m_\chi + m_N)$.

where G_F is the Fermi constant, J, as mentioned before, is the total spin of the nucleus, $S(E)$ is the spin form factor and $\Lambda = \frac{1}{J}[a_p\langle S_p\rangle + a_n\langle S_n\rangle]$, with $\langle S_p\rangle$ and $\langle S_n\rangle$ the expectation values for the spin of the proton and neutron, respectively, and a_p and a_n the coupling constants for the proton and neutron, respectively.

Many detection experiments, based on the detection of DM particles through their elastic scattering with nuclei, have produced quite strong limits. In Fig.2.5 we show the current constraints on the spin–independent nuclear scattering cross–section as a function of WIMP mass.

On the other hand, the most relevant direct detection bounds for SD interactions come from Large Underground Xenon (LUX) experiment and are shown in Fig.2.6.

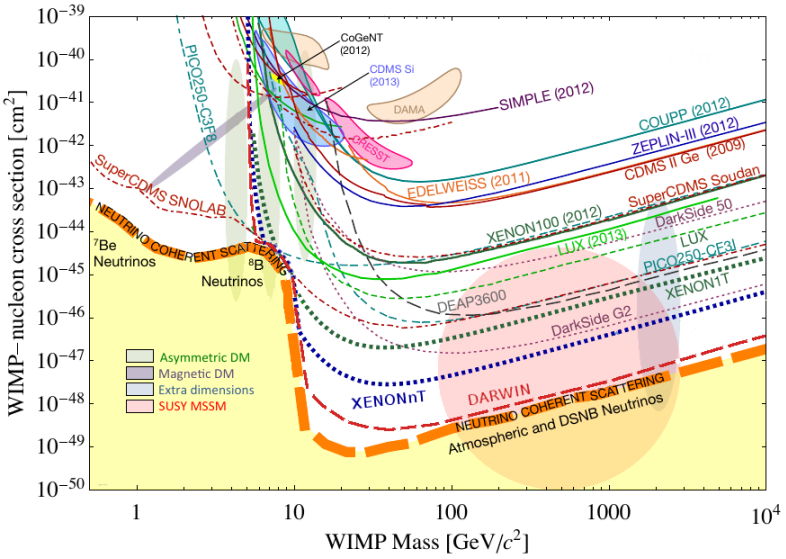

Figure 2.5: Current spin–independent elastic scattering cross section results [79]. The yellow shaded region correspond to a coherent neutrino scattering background.

2.6.2 Indirect detection

Indirect DM searches are complementary to DM direct detection searches. They consist essentially in detecting final states of DM annihilations or decays, i.e. the particles produced when DM particles annihilate or decay. These products appear as fluxes of different types of particles: charged particles (electrons and positrons, protons and antiprotons, deuterium and antideuterium), photons (gamma–rays, X–rays, synchrotron radiation) and neutrinos. For DM annihilation, the flux of this

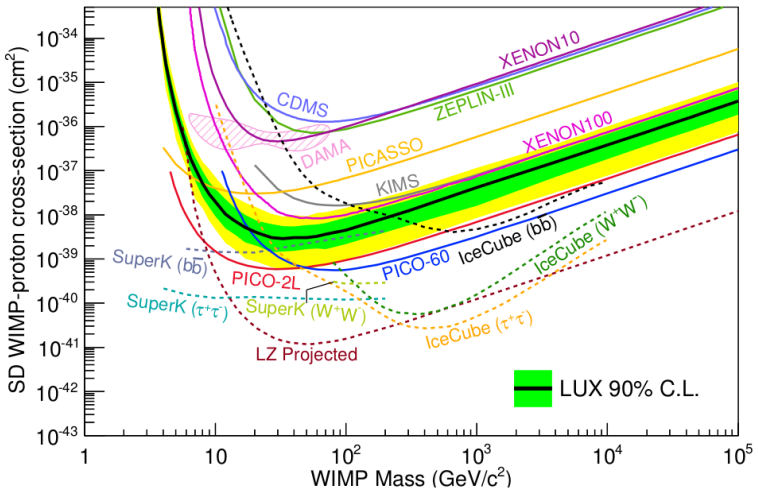

Figure 2.6: Current spin-dependent WIMP–nucleon cross section limits from the LUX experiment [80].

radiation is proportional to the annihilation rate, which in turn is proportional to the squared DM density; for DM decays, it is instead proportional to the DM density. In any case, this means that the best places to look for DM in the Universe indirectly, will be those with the highest DM concentrations.

Attending to the shape of most popular DM density profiles (as described in Section 2.4.1) like, for example, the NFW profile, the center of a galaxy (e.g., the center of our Milky Way) is expected to be the most promising region, having the highest DM density (despite having higher astrophysical backgrounds too). The essential expressions for indirect detection fluxes are shown below, in Section 2.6.2.1, for gamma-rays. However, this picture remains incomplete without the important role of substructures. According to our present understanding of structure formation, relying for example on simulations based on the ΛCDM model, as discussed in Section 1.5.2, structures in the Universe form hierarchically with small halos of DM collapsing first, and then merging and becoming larger. As a consequence, DM halos are populated with smaller, denser halos, the so–called subhalos. Since these substructures correspond to local DM overdensities, they can provide a significant enhancement of the annihilation rate, contributing substantially to the overall gamma-ray emission observed from the Galactic Center [81, 82, 83]. This enhancement of the dark matter indirect signal is often referred to as the *boost* factor, which is discussed in Section 2.6.2.2.

2.6.2.1 Indirect detection fluxes

The calculation of the flux of gamma–rays due to DM particles annihilation reads

$$\frac{d\Phi_i}{dE} = \frac{dN_i}{dE}\frac{\langle\sigma v\rangle}{4\pi m_{DM}^2}\int_{l.o.s.} d\ell\rho^2(\phi,\ell)\,. \tag{2.26}$$

Here, $\frac{d\Phi_i}{dE} \equiv \frac{dN_{ann}}{dA\,dt\,d\Omega\,dE}$ is the number of annihilations per unit time, per unit volume, per energy; dN_i/dE is the spectrum of secondary particles of species i (gamma–rays) from annihilation; σ is the DM particle's pair annihilation cross section, v is the relative velocity of the DM particles, and $\langle\rangle$ denotes the average over the thermal velocity distribution; ℓ is a distance along the line–of–sight (l.o.s), and ρ is the DM density, ϕ is the angle between the line of sight ℓ and the direction of the galactic center. The flux observed is found by integrating the DM density squared ρ^2 along the line–of–sight, connecting the observer on the Earth to the galactic center. If the DM particle is its own anti–particle , Eq. (2.26) is reduced by a factor of 2.

For the case of decaying DM particles in the halo, the differential flux of gamma-rays, the integral along the line of sight reads:

$$\frac{d\Phi_i}{dE} = \frac{dN_i}{dE}\frac{\langle\sigma v\rangle}{4\pi\tau_{DM} m_{DM}}\int_{l.o.s.} d\ell\rho(\phi,\ell)\,. \tag{2.27}$$

where τ_{DM} is the lifetime of the decaying particle, and dN_i/dE is the energy spectrum of i particles emitted per decay.

2.6.2.2 Boost factor for Dark Matter annihilation

As we have seen in precedence, the flux of DM annihilation products (gamma-rays) in different astrophysical regions is proportional to the square of the DM density and thus, regions where the DM density is higher are, in principle, the most promising targets. Hierarchical structure formation in the context of ΛCDM implies that larger halos proliferate of smaller structures, and this clumpy distribution can significantly boost the DM annihilation signal. In order to estimate the boost factor due to DM annihilations, the contribution from the smallest halos has to be included. The minimum subhalo mass depends on the free–streaming of DM particles from high to low density regions [84] and on the effect of acoustic oscillations [85, 86] , which generate an exponential cutoff in the power spectrum and thus, set the cut-off mass. However, these processes depend on the particle physics and cosmological models [24, 87, 88] and hence, the minimum mass is very uncertain, with possible values within $M_{\rm min} = 10^{-11} - 10^{-4}\mathrm{M}_\odot$ (see for example Section 4.5.2 for the analysis corresponding to the supersymmetric scenario to which Chapter 4 is devoted).

The boost factor of the luminosity from dark matter annihilations in a halo of mass M due to its clumpy distribution of matter is given by [89, 90]

$$B(M) = \frac{4\pi}{L_{\rm no-sub}(M)} \int_{M_{\rm min}}^{M} \int_{0}^{R_{\rm vir}} \frac{dn(m,r)}{dm} L(m,r) r^2 \, dr \, dm \,, \tag{2.28}$$

where $L_{\rm no-sub}(M)$ is the luminosity for (smooth) halo distribution without substructures, $L(m,r)$ is the luminosity of a subhalo of mass m at a distance r from the center of the host halo, $M_{\rm min}$ is the minimum mass of the subhalo, $R_{\rm vir}$ is the virial radius and $dn(m,r)/dm$ is the subhalo mass function per unit of volume.

The computation of the boost factor of a given halo of mass M due to the substructure inside it will be undertaken in Chapter 4, where we investigate the impact of different values of $M_{\rm min}$ on the gamma-ray luminosity due to DM annihilation. The luminosity from the smooth distribution, $L_{\rm no-sub}(M)$, is:

$$L_{\rm no-sub}(M) \equiv \int \rho(r)^2 \, 4\pi \, r^2 \, dr = \frac{4\pi}{3} \, r_s^3 \, \rho_s^2 \, \left[1 - \frac{1}{(1 + R_{\rm vir}/r_s)^3} \right] \,, \tag{2.29}$$

where we have assumed an NFW profile.

2.6.3 Accelerator searches

An additional avenue for DM searches is the production of DM particles in laboratory experiments. In the case of massive DM candidates, as in SUSY scenarios, since sparticles are expected to have masses typically above the electroweak scale, they can only be searched at powerful particle colliders, like the Large Hadron Collider (LHC) now in operation.

At colliders such as the LHC, with available center of mass energies at the multi-TeV level, the goal is to look for events where WIMPs are produced. The production of WIMPs and their properties may be inferred by the observation of missing energy-momentum in the reconstructed final states. Many of the DM candidates can be produced copiously at the LHC, either directly or as decay products of other particles. Measurements are then able to provide information regarding not only the masses but also the couplings of both the DM candidate and the additional particles with which it interacts (relevant, in addition, in the calculation of the DM relic density [91, 92]). Recent monojet analyses by ATLAS [93, 94] and CMS demonstrate that the LHC is indeed quite competitive with respect to direct DM searches, in particular for low masses. In Figure 2.7 we show an overview of these results.

***

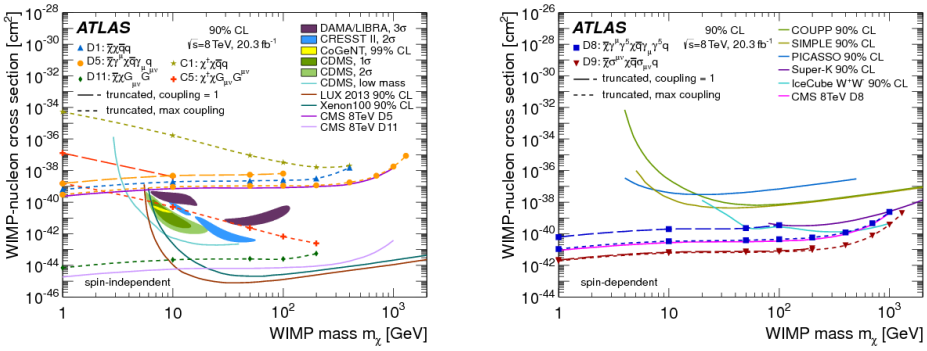

(a) Spin-independent

(b) Spin-dependent

Figure 2.7: 90%-confidence upper limits obtained from a recent ATLAS monojet analysis at a center-of-mass energy of 8 TeV on the spin-independent (left) and spin–dependent (right) DM–nucleon scattering cross section as a function of DM mass m_X for different operators. Results from direct-detection experiments for the spin-independent and spin–dependent cross section and the CMS results are shown for comparison [93].

3 Cold Dark Matter plus X: Constraints on the second dark inert component in the Universe

In the previous two Chapters we have presented an overview of standard Big Bang cosmology and how structure formation based on gravitational instabilities may arise; we also gave a brief overview on the role of dark matter in particle physics, introducing, as well, the detection methods adopted to search it. In this Chapter we address one of the specific work developed for this thesis: the study of a second inert component of DM within mixed dark matter (MDM) models. This Chapter is based on Ref [1], where we study the phenomenology of a broad range of MDM models consisting of a standard cold fraction of DM plus a fraction given by another component, non-cold. We deal with a scenario where the dominant species has to be (nearly) cold to account for current observations, but the sub-dominant species of DM could be warm or hot, or even contribute as a relativistic component.

The different ingredients that have to be considered for such analyses are the following.

- **Theoretical framework/Modelling**
  We consider MDM models which go beyond the reference ΛCDM standard model through the inclusion of a non-cold dark matter species whose temperature is the same of the standard neutrinos. This second inert component of dark matter contributes to the total amount of dark matter in the Universe

as $\Omega_{\rm dm} \approx \Omega_{\rm cdm} + \Omega_{\rm ncdm}$, where $\Omega_{\rm cdm}$ and $\Omega_{\rm ncdm}$ are the density of CDM and non-cold DM components, respectively. The effects of this non-cold DM component are quantified through two parameters: its mass, $m_{\rm ncdm}$, and its fraction, $f_{\rm ncdm}$. We study two typical classes of candidates for the non-cold DM component: fermions and bosons that froze-out when still relativistic. In this work we do not consider any specific particle physics model, that would be necessary in order to compute a non-thermal decoupling of the non-cold DM particle, and we assume that the non-cold DM component was in thermal equilibrium in the early Universe, when it was still relativistic. In Sec. 3.1 we introduce the fundamentals of this MDM model.

- **Goal**
  The goal of this analysis, within the MDM framework, is to study how cosmological measurements can be used to derive limits on the fraction $f_{\rm ncdm}$ of the non-cold DM component with respect to the total DM, as a function of its mass $m_{\rm ncdm}$.

- **Statistical Method**
  With this definite goal in mind, the next step is the methodology to be used. The statistical framework that we chose to conduct the analyses is *Bayesian inference*. We explain the basics of Bayesian analyses in Section 3.2.1. Beside the general Bayesian framework, in Section 3.3, we give details on the implementation of the theoretical framework in the software packages used.

- **Data**
  The last, necessary, ingredient required to confront theoretical predictions with experimental input is the *data*. We combine the most recent CMB temperature, polarization and lensing measurements from the Planck satellite, and the most recent BAO data with the predictions of the number of dwarf spheroidal satellite galaxies. We describe the different sources of data in Section 3.3.

After settling these different ingredients, we present our results in Sections 3.4 and 3.5.

3.1 Cold Dark Matter plus non-so clumpy Dark Matter

The ΛCDM model introduced in Chapter 1 is an extremely succesful model, consistent with the majority of current cosmological measurements as, for example, the acoustic peaks of the CMB, and the large scale structure observations [6, 95]. The ΛCDM model has six parameters: the energy density of CDM, $\Omega_{\rm cdm}$; the baryon energy

density, Ω_b; the reionization optical depth, τ; the angular scale of the acoustic peaks, θ; the amplitude and the tilt of the power spectrum of initial curvature perturbations, A_s and n_s. In addition, as we saw in Section 2.3, the Universe also contains relativistic particles defined in Eq.(2.2). Despite its great observational success, there are still some pending issues concerning the standard ΛCDM paradigm, related to several cosmological observations on galactic and sub-galactic scales, which are not in full agreement with the predictions of the ΛCDM model (see e.g. [96, 97]).

Important challenges for the ΛCDM model are the so-called *too big to fail problem* [98] and the *Milky Way satellite problem* [99, 100]. The former refers to the fact that the measured Galactic velocities indicate that dwarf galaxies are hosted by haloes that are less massive than those predicted by numerical simulations based on the ΛCDM model. The latter is related to predictions within the ΛCDM cosmology for the number of DM subhalos, which is much larger than the observed number of satellite galaxies that orbit close to the Milky Way. A number of solutions to these two problems have been proposed in the literature (see, *e.g.*, the recent works [101, 102] and references therein).

We consider a modified version of the most economical pure CDM model, allowing for a mixed DM cosmology with an additional dark and inert relic. An important subset of these models, where today's DM consists of an admixture of cold and warm DM particles, have been dubbed mixed DM models (see the Ref. [103, 104, 105]). They are a plausible solution to alleviate the small-scale crisis of the ΛCDM cosmology, while leaving the predictions from the CDM model at large scales unchanged. The reason is the following: the particle associated to this second DM component has a larger free-streaming length, affecting the matter power spectrum on the smallest scales, improving the compatibility with the observations of the local Universe. Usually, the free-streaming length is defined as [1] the comoving distance a particle can travel from its production time or time of last scattering, t_0, to the time of matter-radiation equality (MRE), t_{eq}. The approximate expression is given by [17]:

$$\lambda_{\rm fs} = \int_{t_0}^{t_{\rm eq}} dt\, \frac{v(t)}{a(t)} \approx \int_{t_0}^{t_{\rm NR}} dt\, \frac{c\, dt}{a(t)} + \int_{t_{\rm NR}}^{t_{\rm eq}} dt\, \frac{v(t)}{a(t)}\,, \tag{3.1}$$

where $t_{\rm NR}$ is the time when the particle of DM becomes non-relativistic, and $a(t)$ is the scale factor. In the relativistic regime, the velocity of the particle is $v(t) \sim c$, while in the non-relativistic case its momentum redshifts with the expansion as $v \propto a(t)^{-1}$. The effect of the free-streaming is, thus, quantified by the length that a particle travels before the primordial perturbations start to grow (around matter-radiation equality) [106]. This effect depends on the velocity of the particle, varying from a scale value

[1] Alternatively free-streaming can be thought of in terms of the critical Jeans mass in the linear evolution of the matter perturbations (see, e.g. [106]).

of few megaparsec for a warm dark matter component up to the size of the Hubble radius for a relativistic species.

In such a scenario, the non-cold DM species could be either a fermion or a boson. The difference between these cases is in the velocity distribution function. One example of fermion for our non-cold DM particle could be the sterile neutrino (introduced in Section 2.2.1): a sterile neutrino with mass in the keV range is a "warm" DM particle [107, 108, 109]. On the other hand, a boson non-cold DM candidate could be a thermal axion (introduced in Section 2.2.2).

We perform our analysis allowing both the mass and the fraction of the non-cold DM candidate to vary in a very large range. Thus, we will cover a very wide parameter space, exploring at once much more than a single particle physics model. Notice that this is a very wide region for the non-cold DM properties and therefore there are parts in which our results will overlap with other complementary analyses. That would be the case for both the bosonic axion, for which a part of the parameter space is ruled out by astrophysical constraints [110], and the fermionic sterile neutrino, that is constrained to have a mass larger than approximately 1 eV by oscillation searches and relatively large mixing angle [111]. In the latter case, we refer to sterile neutrinos motivated by laboratory anomalies, i.e. those that have a large mixing angle with active neutrinos. Nevertheless, we are not excluding the existence of sterile neutrinos with small mixing angle and with $m < 1$ eV, but those are not relevant since they did not reach the equilibrium in the early Universe [112].

However, we are focusing here on the constraining power of cosmological tools alone for a wide range of models. We do not aim to study specific particle physics candidates for which a combination of all the possible available measurements may further restrict the non-cold DM parameter region.

3.1.1 Model description

Our MDM model is described by the mass of the non-cold particle, $m_{\rm ncdm}$, and the fraction of this non-cold component, $f_{\rm ncdm}$. We *define* that fractional amount of non-cold DM species as

$$f_{\rm ncdm} \equiv \frac{\Omega_{\rm ncdm}}{\Omega_{\rm cdm} + \Omega_{\rm ncdm}} \ , \tag{3.2}$$

where $\Omega_x \equiv \rho_x/\rho_c$, $\rho_{\rm cdm}$ and $\rho_{\rm ncdm}$ are the mass-energy densities of the CDM and non-cold DM components, respectively, and ρ_c is the critical density of the Universe. Note that the total energy density of DM today is, strictly speaking, *not* exactly given by $\Omega_{\rm cdm}+\Omega_{\rm ncdm}$, since $\Omega_{\rm ncdm}$ can be potentially relativistic in our scenario. However, we note that for all cases of interest, $\Omega_{\rm dm} \approx \Omega_{\rm cdm}+\Omega_{\rm ncdm}$ will be approximately correct,

since the fraction that dark radiation can contribute to the energy density today is strongly constrained or, in other words, if the non-cold DM component is radiation, then $\Omega_{\rm ncdm} \ll 1$.

The phase space distribution of particles in thermal equilibrium that decoupled when still relativistic reads as in Eqs.(1.49). We stress again that we are assuming that, once, the non-cold DM component was in thermal equilibrium. It means that we consider a thermal production mechanism for both sterile neutrinos and axions. In the very first and simplest model, sterile neutrinos can be produced in the early Universe via mixing with the active neutrinos [113, 114, 115, 47, 116]. In the latter case, light axions, with mass $0.1{\rm eV} \lesssim m \lesssim 2{\rm eV}$, can be produced in the early Universe via thermal processes, behaving as extra hot DM components, together with the three standard relic neutrinos (see Refs. [117, 118, 119, 120, 121, 122] for current and forecasted future cosmological constraints on these models).

We assume that the non-cold DM component freezes out while still being relativistic ($E = p$), and with zero chemical potential ($\mu = 0$). In that case, the functional form of the momentum distribution is conserved at all later times, with a temperature reshifting like $T \propto 1 + z$ as the Universe expands [17]. We fix the actual temperature of the second component of DM as the same of the standard neutrinos. Namely, $T_{\rm ncdm} = T_\nu = 0.716\, T_{\rm cmb}$, where T_ν is the temperature of the active neutrinos, and $T_{\rm cmb} = 2.38 \times 10^{-4}$ eV is the CMB temperature today. Even if we consider a specific value of $T_{\rm ncdm}$, we are not restricting ourselves, since what is relevant for the cosmological calculations is the ratio $m_{\rm ncdm}/T_{\rm ncdm}$. This means that the results that we find for a particle with mass $m_{\rm ncdm}$ and temperature $T_{\rm ncdm} = T_\nu$ can be easily translated into constraints for a model where the non-cold DM particle is described by any other temperature T' by rescaling the mass accordingly as $m' = m_{\rm ncdm} T'/T_{\rm ncdm}$.

3.2 Statistical Analysis

The model introduced above, "lives" in a multi-dimensional parameter space. In order to explore this parameter space and derive bounds or favored regions for the parameters in which we are interested, we do a Bayesian analysis.

3.2.1 Bayesian Inference

In this Section we give a short and necessarily incomplete account of Bayesian inference, which is the approach we have adopted to analyze our MDM model in the light of existing datasets. There is a wide literature on the subject of Bayesian statis-

tics and we refer the interested reader to [123, 124, 125] (see also [126, 127] for the Bayesian method in Cosmology), which provide a physically-oriented introduction to the subject.

Uncertainty is inherent to the understanding of nature that we gain through experiment: it is the fuzziness with which we know physical constants, parameters of models, results of experiments, etc. Within this fuzziness we assign different degrees of belief to different possible values/results. *Probability* is this assignment of *degree of belief*. Constructed with a few axioms, probability theory provides a fundamental tool to describe consistently our state of knowledge.

The state of knowledge of a given physical quantity is described by a probability density function[2] (from now PDF, also called *probability density function* in the case of discrete variables). The output of an experiment can be understood as the PDF of data within a given model. It is crucial to understand the role played by "within a given model": this PDF is a conditional PDF. For a given set of parameters "$\boldsymbol{\theta}$" describing the model, we assign different degrees of belief to data "$\mathbf{d}$". The conditional probability function

$$p(\mathbf{d}|\boldsymbol{\theta})\,, \tag{3.3}$$

quantifies this degree of belief. However, in the Bayesian approach, our goal is a different one as we want to quantify the degree of belief in a model given a dataset, i.e. we want to estimate the conditional probability of $\boldsymbol{\theta}$ given $\mathbf{d}$:

$$p(\boldsymbol{\theta}|\mathbf{d})\,. \tag{3.4}$$

The relation between the two conditional probability functions, or more precisely the inference of $p(\boldsymbol{\theta}|\mathbf{d})$ from $p(\mathbf{d}|\boldsymbol{\theta})$ is obtained through Bayes Theorem. For two propositions A and B,

$$P(A \cap B) = P(A|B)P(B) = P(B|A)P(A)\,. \tag{3.5}$$

That is, the probability of "A and B (logical AND) is true" is equal to:

- the probability of "A is true" knowing that "B is true" multiplied by the probability of "B is true",
- the probability of "B is true" knowing that "A is true" multiplied by the probability of "A is true".

Consequently

$$P(B|A) = \frac{P(A|B)P(B)}{P(A)}\,, \tag{3.6}$$

[2] In fact our state of knowledge of a given *set* of physical quantities is described by a *joint* probability density function; individual PDFs lack the may-be-correlated nature of the information.

where the denominator is a normalization factor and represents the data probability. For continuous PDFs[3],

$$p(\boldsymbol{\theta}|\mathbf{d}) = \frac{p(\mathbf{d}|\boldsymbol{\theta})\ p(\boldsymbol{\theta})}{\int d\boldsymbol{\theta}\ p(\mathbf{d}|\boldsymbol{\theta})\ p(\boldsymbol{\theta})}\ . \tag{3.7}$$

This simple relation is the cornerstone of the inference process. Let us analyse the different factors:

- $p(\mathbf{d}|\boldsymbol{\theta})$, the *likelihood*, is the degree of belief in $\mathbf{d}$ given $\boldsymbol{\theta}$,
- $p(\boldsymbol{\theta})$, *prior*, is a priori degree of belief in $\boldsymbol{\theta}$,
- $p(\boldsymbol{\theta}|\mathbf{d})$, the *posterior*, the degree of belief in $\boldsymbol{\theta}$ given $\mathbf{d}$; that is, how the incorporated knowledge of $\mathbf{d}$ modifies our prior knowledge of $\boldsymbol{\theta}$.

Posterior probability density functions express our state of knowledge about the value of the different quantities. Bayesian inference is sometimes criticised for the "arbitrariness" of the prior election and its influence on the posterior distribution[4]. This can motivate some degree of scepticism with respect to Bayesian methods; nevertheless, they are quite natural: we always have a certain knowledge of the involved priors (allowed ranges for parameters, etc); if the posterior distribution is sensitive to the prior distribution, what we learn is the poverty of the information that data incorporates to our knowledge compared to our previous knowledge, the prior.

As we have seen, the inference process is achieved through the evaluation of $p(\boldsymbol{\theta}|\mathbf{d})$ in Eq. (3.7). For any parameter $\tilde{\boldsymbol{\theta}}$ we are not interested in[5], we *marginalize* over $\tilde{\boldsymbol{\theta}}$, that is, we integrate over $\tilde{\boldsymbol{\theta}}$ to obtain the marginalized PDF $p(\boldsymbol{\theta}|\mathbf{d})|_{\mathrm{Mar}\{\tilde{\boldsymbol{\theta}}\}}$,

$$p(\boldsymbol{\theta}|\mathbf{d})|_{\mathrm{Mar}\{\tilde{\boldsymbol{\theta}}\}} = \frac{\int d\tilde{\boldsymbol{\theta}}\ p(\mathbf{d}|\boldsymbol{\theta},\tilde{\boldsymbol{\theta}})\, p(\boldsymbol{\theta},\tilde{\boldsymbol{\theta}})}{\int d\boldsymbol{\theta} \int d\tilde{\boldsymbol{\theta}}\ p(\mathbf{d}|\boldsymbol{\theta},\tilde{\boldsymbol{\theta}})\, p(\boldsymbol{\theta},\tilde{\boldsymbol{\theta}})}\ . \tag{3.8}$$

Marginalization is indeed important: since the likelihood function takes values in a parameter space which is typically multi-dimensional, reducing the information to subspaces that one could really handle and represent – typically one or two dimensional spaces – becomes *necessary*. In those subspaces it is still possible to study important properties such as correlations.

It is common practice to present the results of the inference process in terms of *credible regions*, that is regions, in the one or two dimensional space of some quantity of interest, that include a given fraction of the probability, typically 68% and/or 95%

[3]Notice that in the denominator we use $p(\mathbf{d}) = \int d\boldsymbol{\theta}\ p(\mathbf{d}|\boldsymbol{\theta})p(\boldsymbol{\theta})$.

[4]Because of this, "Bayesian" is sometimes replaced by "subjective"; in these terms, objectivity is only thinkable as inter-subjectivity, i.e. through the obtention of conclusions common to several subjective inferences.

[5]For clarity, we now explicitely separate the parameter space in $\boldsymbol{\theta}$ and $\tilde{\boldsymbol{\theta}}$.

(for a one dimensional gaussian these are just the $\pm 1, 2$ standard deviation intervals). Usually, those regions are constructed in such a way that the PDF anywhere inside the region is larger than the PDF anywhere ouside the region.

Before addressing the basics of the method, some additional comments concerning the likelihood are in order. The likelihood function $p(\mathbf{d}|\boldsymbol{\theta})$, usually labeled $\mathcal{L}$, contains all the experimental information to be used (of course, information already used to shape the prior is not to be included in the likelihood). Independent measurements contribute multiplicatively to the global $\mathcal{L}$. One frequent example of likelihood function used to model experimental results is a Gaussian distribution. Let us illustrate it with an example. Consider: (1) a prediction $Q(\boldsymbol{\theta})$ for some observable in a given theoretical framework (it depends on the parameters $\boldsymbol{\theta}$) and (2) an experimental measurement of the quantity Q that we model through a Gaussian (characterized by a central value μ_Q and a standard deviation σ_Q). The corresponding likelihood function would be

$$\mathcal{L} = \frac{1}{\sqrt{2\pi}\sigma_Q} \exp\left(-\frac{(Q(\boldsymbol{\theta}) - \mu_Q)^2}{2\sigma_Q^2}\right) . \tag{3.9}$$

Gaussian likelihoods are particularly convenient when different independent measurements enter the global likelihood: as the global likelihood is the product of all of them, their exponents just add. In this case it is rather common to use equivalently the χ^2 function; for the example above, it would just be

$$\chi^2 = \frac{(Q(\boldsymbol{\theta}) - \mu_Q)^2}{\sigma_Q^2} , \tag{3.10}$$

that is $\chi^2 = -2 \ln \mathcal{L} + c$, where the constant c is irrelevant and thus omitted.

3.3 Dataset and Implementation

In the previous Sections we have seen the model we want to analyse and the methods that this analysis should follow. Now we move from the abstract/conceptual level of those Sections to the real implementation: that is, at a practical level, what is done and how it is done.

3.3.1 CMB dataset

We consider the CMB data of the most recent Planck data release [6], using the full temperature power spectrum at multipoles $2 \leq \ell \leq 2500$ (`Planck TT`) and the polarization power spectra in the range $2 \leq \ell \leq 29$ (`lowP`). We also include the

information on the gravitational lensing power spectrum estimated from the CMB trispectrum analysis, as implemented in the Planck lensing likelihood described in Ref. [128]. The presence of the large scale structures affects the CMB spectrum in a manner related to gravitational lensing. Gravitational lensing measurements can constrain the late time expansion and the clustering of matter through CMB data.

In addition, we have to consider the *nuisance parameters*, which parametrize both the systematic uncertainties and the astrophysical processes that affect the cosmological parameters (see Ref. [129] for further details). In order to exclude some unresolved foreground contributions and constrain better the nuisance parameters used in the likelihood codes, it is common to consider as well the high multipoles of the CMB spectrum. The addition of high-ℓ in the analysis is done by considering the likelihood codes from some Earth-based CMB experiments as the Atacama Cosmology Telescope (ACT) [130] and the South Pole Telescope (SPT) [131], since they have a better angular resolution. However, we follow a very conservative approach and neglect the small-scale polarization measurements (i.e., the so-called `highP`), as there could still be some level of systematics contamination [6].

In order to perform our numerical analyses, we have made use of the publicly available Planck likelihoods [129][6]. We refer to the combination of the data mentioned above as the "CMB dataset".

3.3.1.1 Planck

Since data from the planck satellite plays a central role (see also Figures 1.2 and 1.3) let us remind what is Planck. Planck is a mission of the European Space Agency (ESA) whose objective was to observe - with extreme accuracy - the primordial light of the Universe (the CMB anisotropies), both in temperature and polarization. It was launched in 2009 and used two different instruments, one at low frequency (Low Frequency Instrument) and another one at high frequency (High Frequency Instrument), to probe the emission in the microwave wavelengths at nine different frequencies, in order to subtract the signal of the CMB from the foreground contributions coming from the Milky Way. The CMB temperature spectrum is obtained from the Low Frequency and the High Frequency Instruments using different methods for both the low and high multipoles (low-ℓ and high-ℓ, respectively). The spectra and the likelihoods of the last data release were obtained by considering the following maps:

- For low multipoles ($2 \leq \ell \leq 29$) maps between 70 and 353 GHz were considered using a 94% fraction of the sky;
- For high multipoles and for the temperature spectrum ($2 \leq \ell \leq 2500$) maps at

[6]The likelihood codes are publicly available at the Planck Legacy Archive (`http://pla.esac.esa.int/pla/`).

100, 143 and 217 GHz were considered, using 66%, 57% and 47% of the sky, respectively. On the other hand, for the polarization spectra, they used the same maps but with a fraction of the sky of 70%, 50% and 41%, respectively, in order to avoid regions with a considerably high dust signal.

3.3.2 BAO dataset

Introduced in Section 1.8, we recall that the baryonic acoustic oscillations, caused by the baryons-photon fluid, leave a characteristic scale in the clustering of matter which is visible in the matter power spectrum at late time[7].

In our analysis, we also consider the Baryonic Acoustic Oscillation (BAO) measurements from several experiments. They are 6dFGS [35] at redshift $z = 0.1$, the SDSS Main Galaxy Sample (MGS) [134] at redshift $z_{\rm eff} = 0.15$, and the BOSS experiment Data Release 11 (DR11) using both the results from the LOWZ and CMASS samples [95] at redshifts $z_{\rm eff} = 0.32$ and $z_{\rm eff} = 0.57$, respectively.

3.3.2.1 6dF Galaxy Survey (6dFGS)

The 6dF Galaxy Survey (6dFGS) is a redshift survey which covers 17.000 square degrees of the southern sky. We use a subsample containing $\sim$ 75.000 galaxies at a low redshift ($z = 0.106$) of the 6dF Galaxy Survey (6dFGS) [35] because it allows to constrain the distance-redshift relation through baryon acoustic oscillations. We are interested in the power spectrum $P(k)$ at low redshift.

3.3.2.2 SDSS Main Galaxy Sample (MGS)

The SDSS Main Galaxy Sample (MGS) is a sample of 63.163 galaxies with $z < 0.2$ from the Sloan Digital Sky Survey (SDSS) Data Release 7 [135], that covers 6813 square degrees with an effective redshift $z = 0.15$.

3.3.2.3 CMASS

CMASS are massive and high luminosity galaxies within the Baryon Oscillation Spectroscopic Survey (BOSS) [136]. CMASS galaxies are luminous enough to probe large volumes with sufficient high density to detect, unambiguously, the BAO features. The sample considered here contains 743.803 galaxies covering an effective area of 8.377 square degrees with an effective redshift $z = 0.57$ and in a redshift range $0.43 < z < 0.7$ [95].

[7] See also [132] for a review, and [133] for details on the cosmological implication of BAO measurements.

3.3.2.4 LOWZ

LOWZ is a sample similar to CMASS, but smaller, which contains 265.369 galaxies and that covers an effective area of 7.341 square degrees in the redshift range $0.15 < z < 0.43$ and with an effective redshift $z = 0.32$ [95].

3.3.3 Dwarf spheroidal number counts

In Section 2.4.3, we have seen that one method to define the halo mass function can be inferred through analytical models such as the Press and Schechter [137] (PS) model. The PS approach goes as follows: assuming that the initial fluctuations follow a Gaussian distribution, a region with a mass overdensity above a certain threshold (eventually) collapses to form a bound object [137]. Nevertheless, the PS theory presents a problem: after integrating the halo mass function of Eq. (2.7) over the entire mass range (i.e., $\nu \equiv \delta_{sc}/\sigma(M) \to 0$ when $\sigma(M) \to \infty$) only half of the mass of the whole Universe ends up in collapsed objects[8]. This issue was solved simply multiplying Eq. (2.7) by a factor of 2. There were several improvements over the PS model as, for example, the *excursion set* approach, also referred to as the *Extended PS* model (EPS) [69, 138] (see [139] for a review), that naturally accounts for this missing factor of 2. This technique has been amply used to study, for example, the clustering of dark matter haloes as well as the halo formation.

The PS/EPS approaches fail to describe the halo formation in cosmologies with suppressed power spectra (see, e.g., [140, 141, 106, 142]), since the mass function cannot reproduce the halo abundance of warm dark matter or mixed dark matter cosmologies. One elegant method of circumventing this issue is to assume the *sharp k-space filter* approach, but maintaining the relations between the mass M and the filtering scale R. In the standard PS/EPS formalisms, given a density field $\delta(\vec{x})$, it is possible to "filter" it by using a normalized *window function* $W(\vec{x}; R)$ ($\int W(\vec{x}; R) d^3x = 1$). The window function is chosen to be a top hat in real space. In Fourier space, it is $W(k|M) = [3\sin(kR) - kR\cos(kR)]/(kR)^3$, where the relation between the mass M and the filtering scale R reads $M = \frac{4}{3}\pi\rho_c R^3$ [137]. This relation among M and R is also maintained with the choice of a sharp-k filter [109].

The EPS approach, adapted to the sharp-k model, can be used to estimate the average number of dwarf galaxies orbiting a galaxy like our Milky Way. This has been performed in Refs. [143, 144] where, instead of using a standard EPS approach, the simplified procedure of [145] was followed.

[8]The reason is that we assigned probability zero for all the density fields with $\delta < \delta_c$. These underdense regions correspond to half the mass. The low density peaks will end up in collapsed halos of larger mass. Therefore, only overdense regions participate in the spherical collapse.

Besides including the above CMB and BAO measurements, we derive constraints from the number of dwarf spheroidal satellite galaxies in the Milky Way. This type of galaxies are characterized by a low luminosity and by a mass-to-light ratio much larger than regular galaxies. Nevertheless, the determination of DM in such galaxies is uncertain, since dwarf spheroidals do not have gas in their outer parts. On the other hand, their distribution and number is a probe of the matter perturbations at sub-Mpc scales, which can potentially be affected by the free streaming of the non-cold DM component in our model. For this reason, we estimate the number of satellites predicted for a given MDM scenario. To do this, we have followed the procedure described in Ref. [143, 144], where the authors use a relation based on the conditional mass function normalized to the Aquarius N-body simulation [72]. The conditional mass function is an application of the EPS model. It is as that of Eq. (2.7) but with the origin translated, namely with δ_{sc} and $\sigma^2(M)$ shifted, in order to describe the fact that the subhalo is collapsing inside the high density host rather that low density background. For additional details, see Ref. [139]. According to [138], the expression of the conditional mass function reads

$$\frac{dN}{d\ln M}(M|M_0) = -\frac{M_0}{M}\sigma f(\delta_c, \sigma|\delta_{c,0}, \sigma_0)\,\frac{d\ln\sigma}{d\ln M}\,, \tag{3.11}$$

where M, σ and δ_c are the mass, the variance and the critical overdensity of the "*subhalo*", respectively. The sub-index 0 stands for host halo. By using a sharp-k filter approach, it simplifies as

$$\frac{dN_{sk}}{d\ln M}(M|M_0) = \frac{1}{6\pi^2}\,\frac{M_0}{M}\,f(\delta_c, \sigma|\delta_{c,0}, \sigma_0)\,\frac{P(1/R)}{R^3}\,, \tag{3.12}$$

where $P(1/R)$ is the matter power spectrum, the sub-index *sk* indicates "sharp-k", and M and R are related by the same cubic relation mentioned above. The term $f(\delta_c, \sigma|\delta_{c,0}, \sigma_0)$ is the shape of the conditional mass function:

$$f(\delta_c, \sigma|\delta_{c,0}, \sigma_0) = \frac{(\delta_c - \delta_{c,0})}{\sqrt{2\pi(\sigma - \sigma_0)}}\,\exp\left[-\frac{(\delta_c - \delta_{c,0})^2}{2(\sigma - \sigma_0)}\right]\,. \tag{3.13}$$

The shape of the function $f(\nu) \equiv f(\delta, \sigma)$ in Eq. (2.7) is a Gaussian, while here $f(\delta_c, \sigma|\delta_{c,0}, \sigma_0)$ appears as a Gaussian with the multiplying factor $(\delta_c - \delta_{c,0})$ which is related to the fact that a subhalo is a fluctuation on top of a fluctuation.

The expected number of the dwarf satellite galaxies can be calculated by integrating the conditional mass function over δ_c:

$$\frac{dN_{sat}}{d\ln M} = \frac{1}{N}\int_{\delta_{c,0}}^{\infty}\frac{dN_{sk}}{d\ln M}\,d\delta_c\,. \tag{3.14}$$

where N is a normalization constant.

We followed the procedure of [143, 144] where, after normalizing 3.14 to the Aquarius N-body simulation, the estimate for the number of the satellites reads

$$\frac{dN_{sat}}{d\ln M_{sat}} = \frac{1}{C_n}\,\frac{1}{6\pi^2}\,\left(\frac{M_{hh}}{M_{sat}}\right)\,\frac{P(1/R_{sat})}{R_{sat}^3\sqrt{2\pi(S_{sat}-S_{hh})}}\ , \tag{3.15}$$

where hh stands for "*host halo*" (the Milky Way in our case), sat stands for "*satellites*," and $C_n = 45$ is a number which mimics the results of N-body simulations. In the following we assume $M_{hh} = 1.77 \cdot 10^{12} h^{-1}\mathrm{M}_\odot$ for the Milky Way (MW) and we take $M_{sat,0} = 10^8 h^{-1}\mathrm{M}_\odot$ as a lower integration limit for the calculation of the number of satellite galaxies. Hence, we only consider satellite galaxies above that mass [143].

The parameters R_i, S_i and M_i ($i = sat, hh$) are, respectively, the radius, the variance[9] and the mass of the satellite galaxies or of the host-halo, defined as

$$S_i(M) = \frac{1}{2\pi^2}\int_0^\infty k^2 P(k) W^2(k|M) dk\,, \quad M_i = \frac{4\pi}{3}\,\Omega_m \rho_c (cR_i)^3\ . \tag{3.16}$$

The number $c = 2.5$ is fixed in order to give the best match to N-body simulations. For the calculation of the mass and the variance, we use the k-sharp filter approach. This filter cuts all the scales k below the cut-off scale $1/R_{sat}$ and it is written in terms of the window function $W(k|M)$ (in Fourier space) that enters the above equation (3.16). The window function is:

$$W(k|M) = \begin{cases} 1, & \text{if} \quad k \le k_s(M)\,; \\ 0, & \text{if} \quad k > k_s(M)\,, \end{cases} \tag{3.17}$$

where $k_s(M)$ is the cut-off scale as a function of the mass.

The computation of the number of the dwarf spheroidal galaxies has been implemented in a likelihood function (labelled "SAT"), incorporeted into `Montepython`. We define the satellite likelihood as a half-Gaussian with mean $N_{\rm sat} = 61$ and standard deviation $\sigma_{N_{\rm sat}} = 13$.[10] In other words, we only consider satellite galaxy bounds when the predicted number of satellite galaxies within a given model is *below* the mean number of galaxy satellites that are (expected to be) observed, with the present observations ($N_{\rm sat} = 61$) representing only a lower limit. This assumes the plausible scenario that not all dwarf spheroidal galaxies in the relevant mass range have been found up to now, and that the number of satellite galaxies might increase by ongoing and/or future searches.

[9] S is the variance of the gaussian random field of which the halo is an excursion [69].

[10] The choice of $N_{\rm sat} = 61$ is motivated by Refs. [144, 146], in which the authors add to the eleven standard satellites the fifteen observed by SDSS, after having corrected for the limited sky coverage of the SDSS catalogue ($f_{\rm sky} \simeq 0.28$), resulting in $\sim 61 \pm 13$ satellite galaxies. The error only accounts for the SDSS sample, for which we assume Poisson statistics, see Ref. [146].

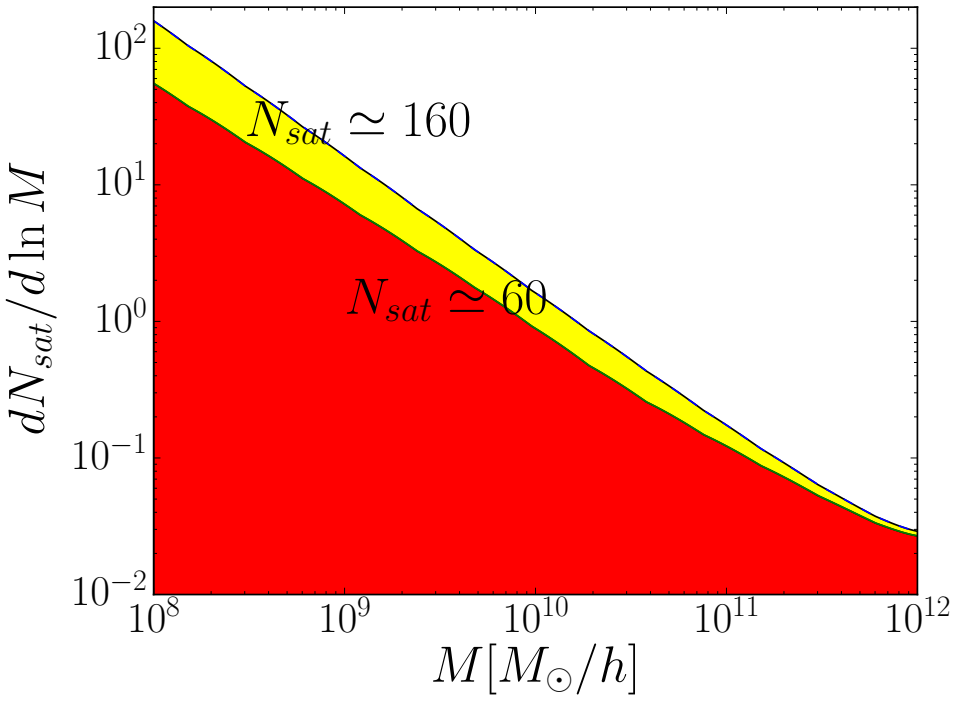

Figure 3.1: Estimate of the number of satellites with mass M inside a host halo with mass $M_{hh} = 1.77 \cdot 10^{12} h^{-1} M_\odot$, for two different MDM models. The thin green solid line which separates the two coloured regions refers to a non-cold DM component with fraction $f_{\rm ncdm} = 0.25$ and mass $m_{\rm ncdm} = 10^3$ eV, corresponding to a total of $\simeq 60$ dwarf spheroidal satellites galaxies. The black line which limits the upper coloured region refers to a model where the fraction is $f_{\rm ncdm} = 0.9$ and the mass is $m_{\rm ncdm} = 10^5$ eV, corresponding to a total of $\simeq 160$ dwarf spheroidal galaxies.

In Fig. 3.1, we show the number of satellite galaxies, see Eq. (3.15), versus the satellite mass, for a Milky Way-like host halo with mass $M_{hh} = 1.77 \cdot 10^{12} h^{-1} \mathrm{M}_{\odot}$. We show two cases. The first case depicts a situation where the mass of the non-cold DM particle is large ($m_{\rm ncdm} = 10^5$ eV) and it constitutes almost all the DM ($f_{\rm ncdm} = 0.9$). The other case is for smaller values of the mass and the fraction of the non-cold DM species, having $m_{\rm ncdm} = 10^3$ eV and $f_{\rm ncdm} = 0.25$, respectively. For the ΛCDM-like scenario we get $N_{\rm sat} \sim 160$, while for the second scenario we obtain $N_{\rm sat} \sim 60$, providing naively a better agreement with observations. However, we are conservatively imposing that our model must reproduce *at least* the number of observed dwarf satellite galaxies, penalizing only those cases for which the number of satellite galaxies is *smaller* than the observed one. Hence, both of the exemplary MDM scenarios will be equally allowed by the "SAT" likelihood, since future measurements may detect more of these objects.

3.3.4 Boltzmann code and scanner

To calculate the evolution of matter perturbations in the Universe and evaluate the CMB and BAO observables, we use the Boltzmann solver code `CLASS` [147]. The tool used for the computation of the likelihoods is `Montepython` [148], which informs CLASS about the cosmological parameters and retrieves the computed quantities. In order to explore the N-dimensional parameter space and get limits on the various parameters, we adopt a nested sampling algorithm as implemented in the publicly available `Multinest` code [149, 150, 151], a tool for the estimation of the Bayesian evidence and of the parameter constraints. It uses an ellipsoidal and multimodal nested-sampling algorithm to estimate the posterior probability over the entire parameter space. Then, we link `Montepython` to `Multinest` by using `PyMultiNest` [152] which interacts with `MultiNest`. Namely, the inner MCMC routine in `Montepython` is substituted with the algorithm of `Multinest`. In practice, instead of doing a standard MCMC, the selection of the points is addressed by `Multinest`.

The varying cosmological parameters are the six basic ΛCDM parameters introduced in Section 3.1, plus the mass of the non-cold DM component, $m_{\rm ncdm}$ and its fraction, $f_{\rm ncdm}$. In order to estimate the Bayesian evidence we give a prior as input. The priors for the standard ΛCDM cosmological parameters are chosen to be flat, while for the mass and the fraction of the non-cold DM component we use flat priors on their logarithms, having:

$$\log_{10}(m_{ncdm}/\mathrm{eV}) \text{ uniform in } : [-5; 5]\,; \tag{3.18}$$

$$\log_{10} f_{ncdm} \text{ uniform in } : [-6; 0]\,. \tag{3.19}$$

We stress again that this is a very wide region for the non-cold DM properties, and

therefore there are parts in which our results will overlap with other complementary analyses.

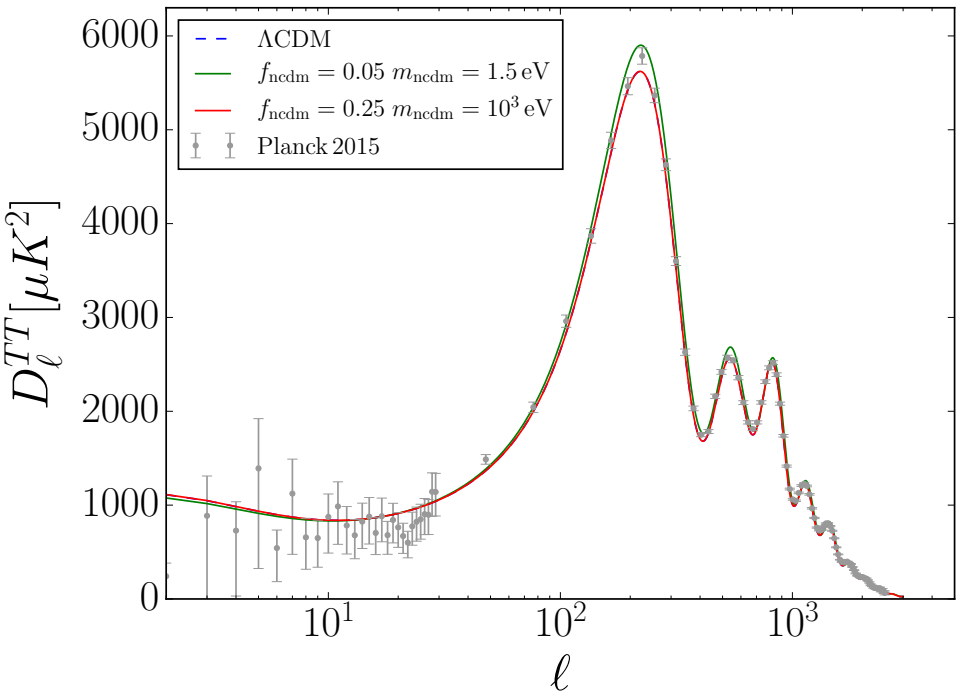

Figure 3.2: Angular power spectrum for two different models. The green (red) solid line refers to a non-cold DM component with fraction $f_{\rm ncdm} = 0.05$ ($f_{\rm ncdm} = 0.25$) and mass $m_{\rm ncdm} = 1.5$ eV ($m_{\rm ncdm} = 10^3$ eV). The standard ΛCDM predictions are depicted by a blue dashed line, that is not visible because it coincides with the red one. The data points and errors are from the Planck 2015 data release [6] (see Fig.1.3.

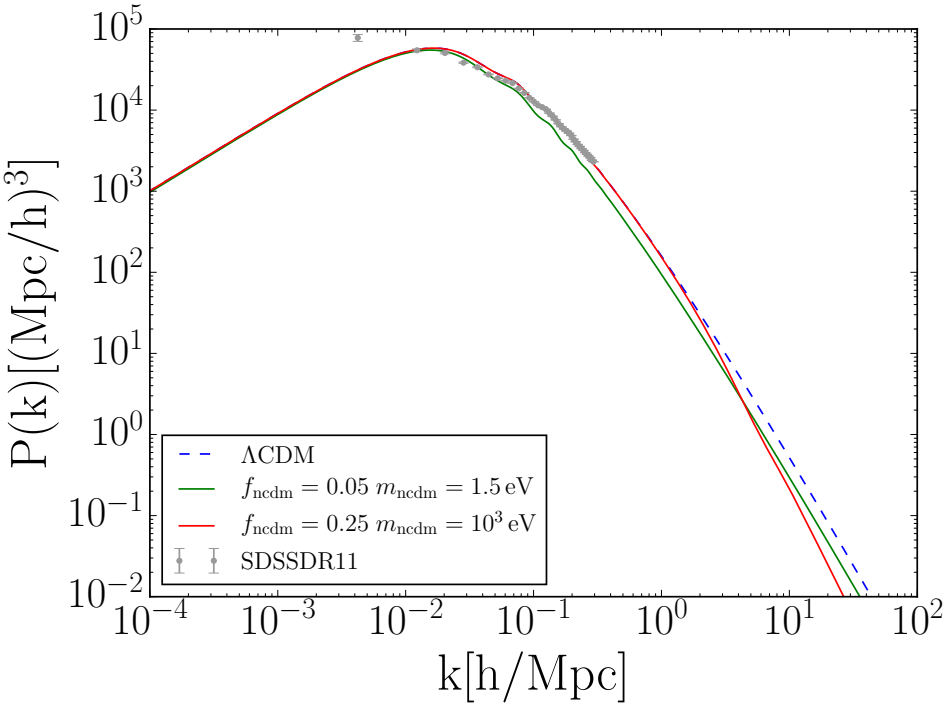

Figure 3.3: The same as in Fig. 3.2, but for the matter power spectrum. The data points and their errors are from the BOSS DR11 measurements [95]. Notice that we use BOSS DR11 data in its geometrical form, i.e. using the BAO information rather than the shape of the power spectrum information.

Before going to the main results, we first give an impression of how much the standard cosmological picture changes for two exemplary MDM scenarios explored here. Figures 3.2 and 3.3 show the angular power spectra and the matter power spectra, respectively, obtained by using two models: one with $f_{\rm ncdm} = 0.25$ and $m_{\rm ncdm} = 1$ keV, and a second one with $f_{\rm ncdm} = 0.05$ and $m_{\rm ncdm} = 1.5$ eV. We show for comparison the predictions for the standard ΛCDM model, as well as the measurements from the latest data release of Planck satellite [6] (from the BOSS DR11 sample [95]) in the case of the temperature anisotropies (matter) power spectrum.

Notice that for the case $m_{\rm ncdm} = 1$ keV and $f_{\rm ncdm} = 0.25$, the predictions for the temperature power spectrum are essentially identical to those within the canonical ΛCDM scenario for most of the scales. This is due to the fact that CMB physics is basically unaffected by the free-streaming nature of a 1 keV particle that accounts here for 25% of the total DM mass-energy density. There only exists a tiny difference in the matter power spectrum at very small scales (see Fig. 3.3) due to the suppression of the growth of matter perturbations induced by the non-zero velocity dispersions of the non-cold DM component, even if it is not the dominant one. Therefore, we expect this point in the parameter space to be allowed by both CMB data and satellite galaxy measurements. On the other hand, the MDM model with $f_{\rm ncdm} = 0.05$ and $m_{\rm ncdm} = 1.5$ eV gives predictions for the CMB temperature anisotropies that are not compatible with the present CMB data. This is because the non-cold DM component behaves as radiation at the decoupling period, enhancing the first acoustic peak height, although the effect will be degenerate with the CDM energy density, in such a way that one could partly compensate this enhancement by increasing the total DM energy density. However, the suppression in the matter power spectrum for $m_{\rm ncdm} = 1.5$ eV occurs at much larger scales than before, due to the shorter free-streaming scale, showing a clear discrepancy with power spectrum measurements.

3.4 Results

In this Section we show the main results obtained in the analysis.

In Fig. 3.4, we show in equal-weight scatter plots[11] our numerical results as function of the fraction and mass of the non-cold DM component. As described above, the results are based on the combination of CMB+SAT+BAO data. The samples are colour-coded by the predicted number of satellite galaxies. We find that the number counts of dwarfs start to be noticeably affected for fractions larger than a few percent, and for masses up to around 10 keV. At 100 keV, the non-cold DM component behaves essentially as CDM for our purposes.

In Fig. 3.5 we show the central results of this work. For each decade in the mass of the non-cold DM component, we show the marginalized upper limits on its fraction $f_{\rm ncdm}$ for both fermions and bosons. We find that the 95.4%CL limits for masses 1–10 keV are $f_{\rm ncdm} \leq 0.29$ (0.23) for fermions (bosons), and for masses 10–100 keV they are $f_{\rm ncdm} \leq 0.43$ (0.45), respectively.

For large values of the non-cold DM mass, our limits on its fraction $f_{\rm ncdm}$ are competitive to those existing in the literature; see, *e.g.*, Ref. [153]. In this regime the bounds come mainly from the BAO data and the number of satellites galaxies, since CMB alone is not able to distinguish the heavy non-cold DM component from a pure CDM one.

On the other hand, in the semi-relativistic regime, 10–100 μeV, the limits are very strong, $f_{\rm ncdm} \leq 3.3{\times}10^{-6}$ ($9.8{\times}10^{-6}$) for fermions (bosons). This is expected, since in the relativistic limit the current cosmological upper bounds on dark radiation, $\Delta N_{\rm eff}$, apply. We use Eq. (2.2), where $N_{\rm eff}$ is defined as the ratio of the energy density of all relativistic species, ρ_x (which includes standard neutrinos plus any other non-cold DM component in its relativistic regime), to that of photons as:

$$N_{\rm eff} = \left(\frac{8}{7}\right)\left(\frac{11}{4}\right)^{4/3} \frac{\rho_x}{\rho_\gamma}\,. \tag{3.20}$$

Indeed, we find for a very light non-cold DM particle:

$$f_{\rm ncdm} = \frac{\Omega_{\rm ncdm}}{\Omega_{\rm dm}} = \frac{\Omega_\gamma\,\Delta N_{\rm eff}}{\Omega_{\rm dm}} \approx 10^{-4}\Delta N_{\rm eff}\,. \tag{3.21}$$

Considering that the 95.4%CL limits that arise from the standard ΛCDM+$N_{\rm eff}$ analyses [6] correspond to $\Delta N_{\rm eff} \lesssim 0.3$, our limits for $f_{\rm ncdm}$ when the mass is around 10–100 μeV are in reasonable agreement with Eq. (3.21). The agreement, however,

[11] The weights given by `Multinest` incorporate both likelihood and prior information.

is not complete, especially in the fermion case. The reason is that the region of parameter space that corresponds to such a case is rather small and the shot noise of the simulation has a significant role, so that even the `Multinest` algorithm cannot properly explore it. The result is that the density of sampled points in the relevant region is not sufficient to obtain exactly the expected constraints corresponding to Eq. (3.21).

Moreover, as we can see in Fig. 3.5, there are several small unexpected differences between the fermion and the boson case. These discrepancies between the two cases are also due mainly to the shot noise of the Monte Carlo simulation.

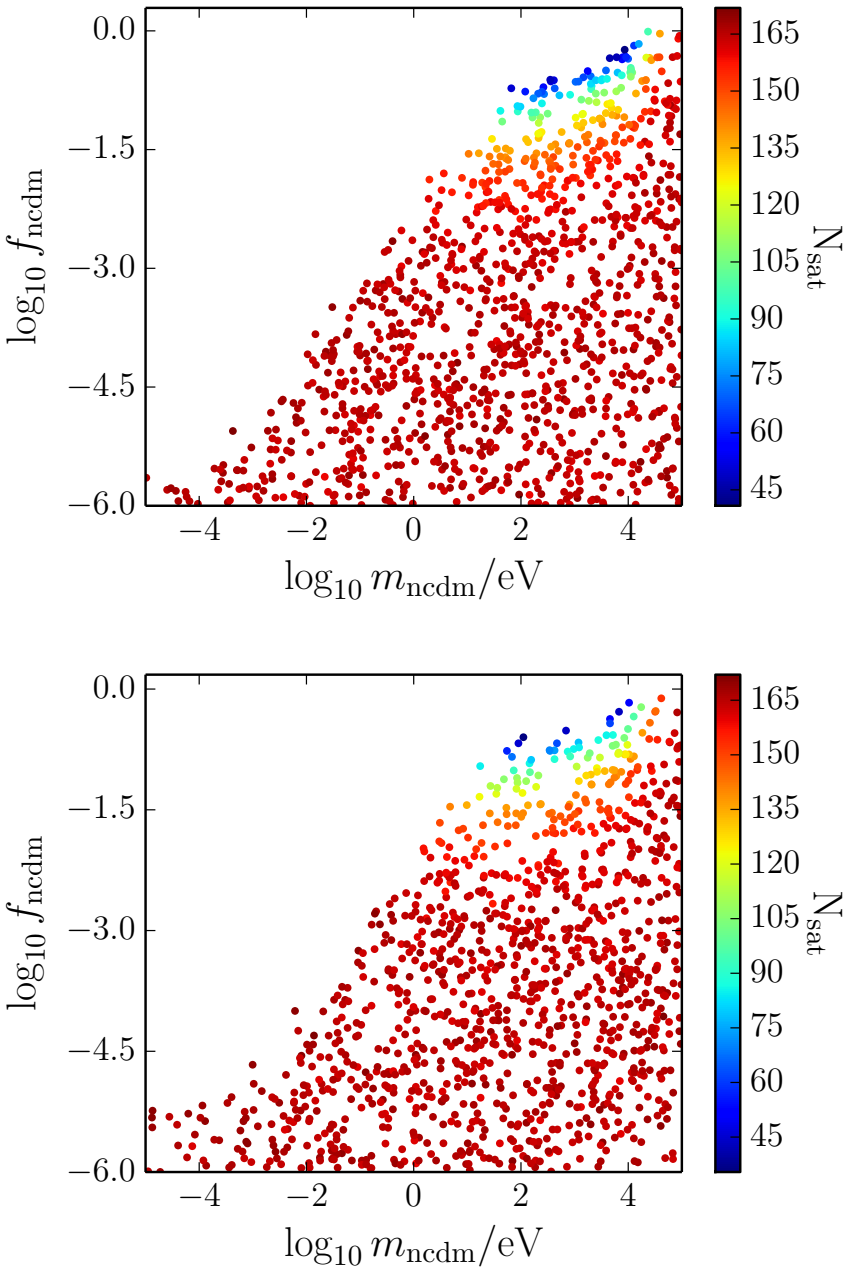

Figure 3.4: Samples in the ($\log_{10} f_{\rm ncdm}$, $\log_{10} m_{\rm ncdm}$) plane from CMB+SAT+BAO data, colour-coded by the number of the satellite galaxies obtained for the case of a fermionic (top panel) or bosonic (bottom panel) non-cold DM candidate.

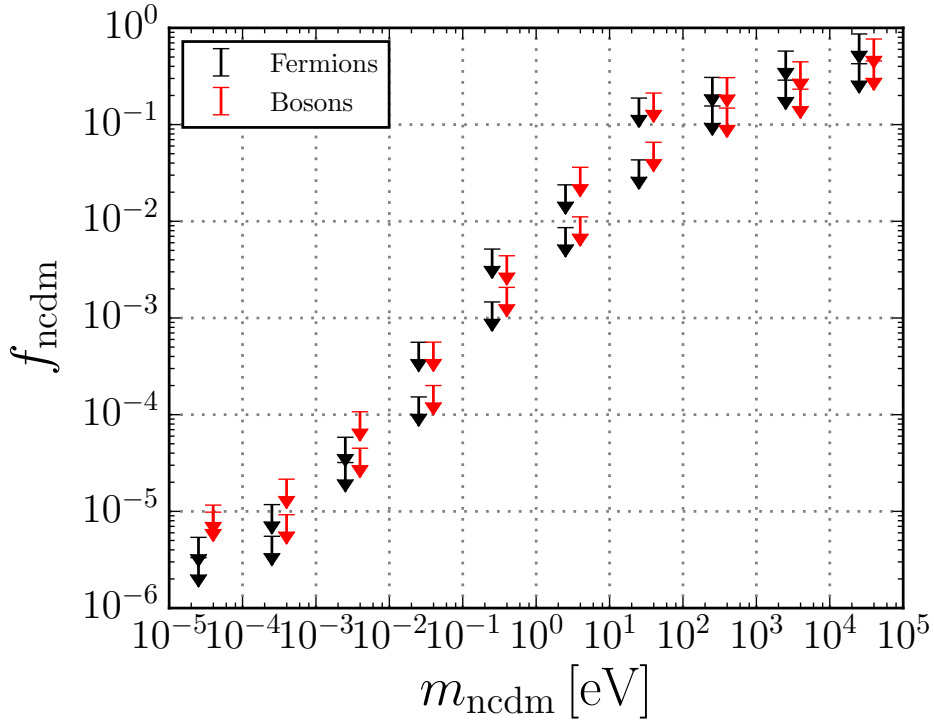

Figure 3.5: 2σ and 3σ upper limits on the fraction $f_{\rm ncdm}$ of the non-cold DM component, obtained for different ranges of masses. In black (red) we present the results derived from the analysis of the CMB+SAT+BAO datasets for a fermion (boson) non-cold DM candidate.

3.5 Discussions

In this work, we have explored the cosmological bounds arising from Planck CMB temperature and polarization at low multipoles plus BAO measurements on general cosmological models with a second non-cold dark component. To constrain this second component of DM in the regime where it is warm, we include additional constraints by requiring that the model does not under-predict the number of satellite galaxies observed in the Milky Way. We adopt phase space distributions for the non-cold DM species that correspond to a component that froze out while still being relativistic.

We compare results for bosonic and fermionic non-cold DM species. Our results show that, for the adopted observables, there is not a substantial difference between the allowed regions corresponding to the bosonic and fermionic cases. In the following we summarise the most important results.

- We find that for small masses of this second species of DM, the limit on its fraction relative to the total amount of DM in the universe ($f_{\rm ncdm}$) is around a few times 10^{-5}. This limit is approximately close to what one would expect from present constraints on the extra relativistic degrees of freedom $\Delta N_{\rm eff}$.
- On the other hand, for high values of its mass, above fractions of keV, the CMB is unable to distinguish among the non-cold DM and CDM components and one therefore needs to look for independent observables such as the matter power spectrum that we include through the measurements of the BAO scale. In that case, we obtain for $f_{\rm ncdm}$ the following 2σ-level upper limits:
  1. for non-cold DM particles with mass in the range 1–10 keV, $f_{\rm ncdm} \leq 0.29$ (0.23) in the fermionic (bosonic) case;
  2. for non-cold DM particles with mass in the range 10–100 keV, $f_{\rm ncdm} \leq 0.43$ (0.45).
- For these (high) values of the mass of the non-cold DM component, our limits on its fraction $f_{\rm ncdm}$ are slightly tighter than those existing in the literature (see e.g. Ref. [154, 153, 155]).
- Forthcoming precise measurements of the matter power spectrum at small scales may be able to further corner mixed DM scenarios.

***

4 Prospects on the Dark Matter Protohalos within Supersymmetric Models

This Chapter is based on paper [2], where a study of the kinetic decoupling of dark matter within the context of a supersymmetric extension of the Standard Model is used to analyse the properties of dark matter protohalos, in connection with the most probable neutralino masses and the implications for direct, indirect detection and colliders.

Section 4.1 is devoted to supersymmetric extensions of the SM. First, in subsection 4.1.1, we expand the initial discussion on the motivations for supersymmetric extensions of the SM. In subsection 4.1.2, we discuss relevant aspects of supersymmetric scenarios, in particular the one under consideration, taking into account the constraints after the first run of the LHC (with collisions at center-of-mass energies of 7-8 TeV[1]) while in Section 4.2, the concepts and tools involved in the analysis are presented. Kinetic decoupling and protohalos are then addressed, within this supersymmetric context, in section 4.3. The first results of the analysis are presented and discussed in the following section: the most probable regions in parameter space in 4.4.1, and profile likelihood maps in 4.4.2. The implications for direct and indirect detection of DM are then explored in subsections 4.5.1 and 4.5.2, respectively. A short discussion of collider implications of the analysis is also included, in 4.5.3. To

[1]Since this work, the second run of the LHC has started with increased center-of-mass energies of 13 TeV.

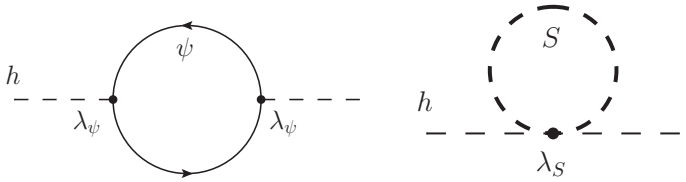

(a) Fermion loop. (b) Scalar loop.

Figure 4.1: One loop diagrams contributing to the Higgs mass corrections.

close the chapter, a summary of the results is given in section 4.6.

4.1 Supersymmetry

4.1.1 Motivations

Supersymmetry was introduced in section 2.2.3 as a class of scenarios which provide dark matter candidates of the WIMP type. Additional motivations, in particular addressing the *hierarchy problem* and improving the unification of gauge couplings in Grand Unification theories, do also contribute to the interest of SUSY extensions of the SM.

The hierarchy problem is a *naturalness* problem associated to the presence of a scalar, the Higgs, in the SM. Consider the one-loop diagram in Figure 4.1(a), which involves an interaction term $\lambda_\psi\, h\, \bar{\psi}\psi$ among a scalar h (from now on, "the Higgs") and a Dirac fermion ψ. It gives a contribution (a "correction") to the Higgs mass of the following form:

$$\delta m_h^2 = -\frac{1}{8\pi^2}|\lambda_\psi|^2\{\Lambda^2 + \ldots\}\,, \tag{4.1}$$

with Λ some ultraviolet cutoff usually considered to be, at least, the energy scale at which new physics enters the high energy (ultraviolet) behaviour of the theory.

If Λ is related to some Grand Unification scale or to the Planck mass scale, δm_h^2, which is expected to be a *correction*, is in fact many orders of magnitude larger than the electroweak scale or the Higgs mass (the problem comes from the huge difference among the 100 GeV scale and that high energy scale of new physics, not from the precise value of the Higgs mass, 125 GeV, or the regularization scheme). This would drag the whole SM spectrum to that high scale, since all the masses within the SM are related to the Higgs. There is of course a way out. Since the *physical* Higgs mass m_h^2 is the sum of that correction and a tree level value, $m_h^2 = (m_h^2)_0 + \delta m_h^2$, the value

of $(m_h^2)_0$ can be carefully tuned to obtain $m_h^2 = (125\ \text{GeV})^2$ out of the difference of two much, much, larger numbers. This way out, this kind of fine tuning, is *unnatural*. There would be no reason for the scalar to be light (compared to high energy scale), except for the tuning of the parameters up to many decimal places. In contrast to the scalar case, loop corrections to fermion masses are proportional to the masses themselves; when the mass of a fermion becomes zero, there is an additional chiral symmetry which "protects" the mass from becoming non-zero. From that point of view, having light fermions is *natural*. For vector mesons, having zero masses can also be viewed as a natural consequence of symmetry, of *gauge* symmetry in that case, as it happens, for example, with the photon. Coming back to our toy example, consider now an additional interaction term $\lambda_S\, h^2|S|^2$ of the Higgs with a complex scalar S. The one-loop diagram of Figure 4.1(b) would give a contribution to the Higgs mass

$$\delta m_h^2 = \frac{1}{16\pi^2}\lambda_S\{\Lambda^2 + \ldots\}\,. \tag{4.2}$$

Now, if λ_S in Eq. (4.2) and λ_ψ in Eq. (4.1) were related, owing to the relative -1 sign arising from the scalar versus fermion closed loop, a cancellation among both contributions could arise. If that relation among couplings is based on a symmetry, that cancellation would be *natural*, and no hierarchy problem would arise. In that respect, this is what supersymmetry, a priori, achieves. Since exact supersymmetry is not a possibility (superpartners of known fermions would have their same masses, and that is not the case), it has to be broken, as mentioned in Section 2.2.3, softly, at an energy scale of the order of the TeV. Although this reintroduces the need of some fine tuning, it remains rather reduced.

Concerning unification of gauge couplings, running the renormalization group evolution of the three gauge couplings in the SM does not lead to a common value of all three at any given energy scale (a common value of all three gauge couplings would be a hint of a unified dynamics at that scale, then broken down and evolved differently to low energies). The situation in supersymmetric scenarios is schematically summarised in Figure 4.2: once the SUSY particles affect the evolution of the couplings, the extrapolation to high energies can lead to a common value at around 10^{16} GeV. For the interested reader we refer to the now classical introduction [156] for further details.

4.1.2 Status

Despite the high expectations for the direct discovery of light SUSY particles at the LHC (after the negative results at LEP and the Tevatron), so far no signal of new physics has been found. This could be considered to be in tension with the ideas of natural SUSY. Nevertheless, the mass of the Higgs boson, heavier than what

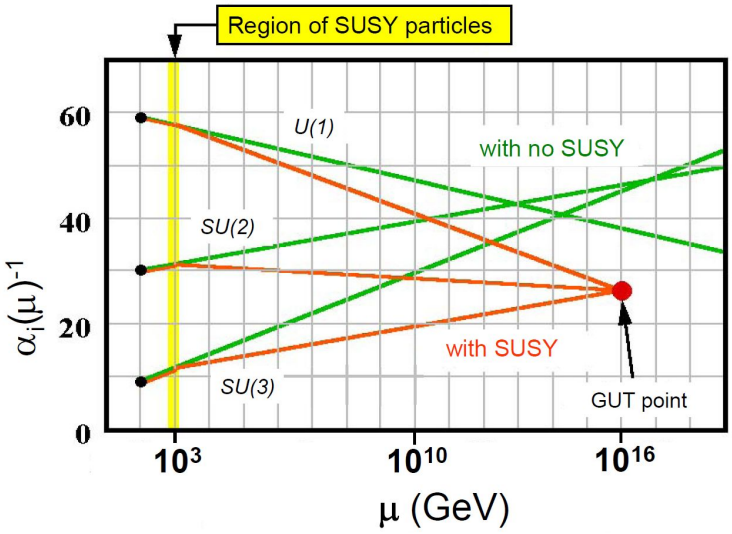

Figure 4.2: Running couplings and unification in the MSSM. Figure from `http://sites.uci.edu/energyobserver/2012/12/02/update-on-some-higgs-blog-entries/`

would be more easily accommodated, would rather point to a heavier mass spectrum and suggest that the lack of discovery of sparticles in the first run of the LHC is a consequence of the Higgs mass value.

In the MSSM, a lightest Higgs boson of around 125 GeV implies a range of $M_{\rm SUSY}$ between[2] $\sim 10^3$ GeV and $\sim 3 \cdot 10^4$ GeV, where $M_{\rm SUSY}$ is the typical scale at which SUSY particles decouple from the SM (for details, see [159, 160]). Hence, within the MSSM framework, the Higgs mass and naturalness of the electroweak symmetry breaking, require a tuning at the $\mathcal{O}(1)\%$ level, see, e.g., [161]. This tension is, in any case, relaxed going beyond the MSSM [162, 163, 164, 165, 166]. Moreover, since stops contribute most to the Higgs mass, the allowed range of $M_{\rm SUSY}$ could be translated into a constraint on the stop sector, requiring stop masses typically larger than ~ 3 TeV, unless they mix maximally [167], while the rest of the SUSY spectrum is left rather unconstrained [3].

[2]This range is valid for relatively large values of $\tan\beta$, the ratio of vacuum expectation values of the two different Higgs doublets in the MSSM, H_u and H_d. Small values of $\tan\beta$ are disfavoured since they force lighter Higgs (see, e.g., the reviews [157] and [158]).

[3]Notice however that for example [161] re-examined natural SUSY scenarios showing that light stop masses, closer to the lower limits imposed by the Higgs mass, are not really a generic requirement of natural SUSY scenarios.

On the other hand, as already mentioned, one of the attractive aspects of SUSY, is the apparent unification of gauge couplings (in the MSSM). Taking SUSY parameters at $M_{\rm GUT}$ and evolving with the renormalization group equations (RGE), leads to implicit relations between sparticle masses when matching at low energies with the SM is imposed[4]. In particular, for $\tan\beta = 10$, the average of the two stop masses at a scale of 1 TeV, $\overline{m}_{\tilde{t}}^2$, expressed in terms of the soft parameters at $M_{\rm GUT}$ [161], reads:

$$\begin{aligned}\overline{m}_{\tilde{t}}^2 \simeq\ & 2.972\, M_3^2 + 0.339\, m_{\tilde{Q}_3}^2 + 0.305\, m_{\tilde{U}_3}^2 + 0.091\, M_2^2 \\ & - 0.154\, m_{H_u}^2 - 0.052\, A_t^2 + 0.017\, M_1^2\ \ldots + m_t^2\,, \quad (4.3)\end{aligned}$$

where M_1, M_2 and M_3 are, respectively, the bino, wino and gluinos soft mass terms, $m_{\tilde{Q}_3}$ and $m_{\tilde{U}_3}$ are the masses of the third generation squarks, and m_{H_u} is the H_u soft mass. Equation (4.3) shows that large stop masses imply large gluino masses, $M_{\tilde{g}} \simeq 2.22 M_3$, unless the mass terms of the third generation squarks are very large.

In terms of naturalness, the largest tuning necessary to obtain the correct electroweak symmetry breaking (EWSB) concerns the μ parameter. From the minimization of the Higgs potential one obtains

$$\begin{aligned}\frac{1}{2}M_Z^2 = (&1.62\, M_3^2 - 0.64\, m_{H_u}^2 + 0.37\, m_{Q_3}^2 + 0.29\, m_{U_3}^2 - 0.29\, A_t\, M_3 \\ & - 0.20\, M_2^2 + 0.14\, M_2 M_3 + 0.11\, A_t^2 + \ldots) - \mu^2\,. \quad (4.4)\end{aligned}$$

This expression is valid at a scale of 1 TeV, for $\tan\beta = 10$ [161]. As in (4.3), the M_3 contribution has the largest coefficient. The bounds from ATLAS and CMS [169, 170], $m_{\tilde{g}} > 1.33$ TeV on the gluino mass (assuming 100% decays to $q\bar{q}\chi_1^0$ and a mass difference between $\tilde{g}$ and χ_1^0 of at least 200 GeV), are the more stringent for naturalness. It is also important to stress that, according to equations (4.3) and (4.4), naturalness and Higgs constraints affect mainly the gluino and squarks sector while sleptons, Binos and Winos are basically unconstrained.

In a more general framework, the phenomenological MSSM, pMSSM for short, where the MSSM is simply parameterized at the electroweak symmetry breaking scale, the Higgs mass measurements constrain mainly the stop sector and leave the rest of the spectrum effectively unconstrained. In this case, the main constraints on sparticle masses come from LHC limits and from B-physics (see, e.g., Refs. [171, 172, 173, 174]).

Besides the tuning associated to the electroweak symmetry breaking, having a good DM candidate also requires some tuning. References [175, 176] have studied the fine tuning required to produce the correct DM relic density.

[4]Notice nevertheless that in gravity mediated SUSY breaking scenarios, conditions are rather set at $M_{\rm Planck}$. For some particular scenarios, starting the RGE running from $M_{\rm GUT}$ instead of $M_{\rm Planck}$ is not necessarily a correct approximation [168].

4.2 Analysis

4.2.1 Generalities

Having introduced the SUSY context of our work from its particle physics side, this Section details additional aspects of the analysis and the specific incarnation of the MSSM that has been considered. In order to study the model, that is in order to study its parameter space, numerical methods adequate for the task are sophisticated. The analysis that has been done is a Bayesian one. Some basic statistical notions on Bayesian analysis have been reviewed in Section 3.2.1.

At this point, we specify our SUSY scenario: we assume gravity mediated SUSY breaking, and consider the MSSM with 10 fundamental parameters defined at the unification scale of the gauge couplings, in addition to the Standard Model parameters. Unification is assumed. Furthermore, squark masses, slepton masses and trilinear terms follow universality (they do not distinguish among generations, in terms of matrices in generation space, they are proportional to the identity matrix). Then, the set of 10 parameters is

$$\{g_i, y_i, M_1, M_2, M_3, m_0^{\rm sq}, m_0^{\rm sl}, m_H, A_0^{\rm sq}, A_0^{\rm sl}, \mu, B\}. \tag{4.5}$$

g_i and y_i are, again, the gauge and Yukawa couplings. M_1, M_2, M_3 are the gaugino masses, while $m_0^{\rm sq}$, $m_0^{\rm sl}$ and m_H are the squark, slepton and neutral scalar masses, respectively. $A_0^{\rm sq}$ and $A_0^{\rm sl}$ are the squark and slepton trilinear couplings, finally, as already introduced, B is the bilinear Higgs coupling, and μ is the Higgs mass term in the superpotential. It is more convenient to use the equivalent set of parameters

$$\{\mathbf{SM}, M_1, M_2, M_3, m_0^{\rm sq}, m_0^{\rm sl}, m_H, A_0^{\rm sq}, A_0^{\rm sl}, \tan\beta, \text{sign}(\mu)\}, \tag{4.6}$$

where **SM** stands for the SM parameters, since $\tan\beta$, $\text{sign}(\mu)$ are more easily related to observables than μ and B; the most relevant ones for the analysis are included in Table 4.1. Without loss of generality, the sign of μ is fixed to $+1$; then, allowing M_i to take positive and negative values, regions with relative phases between μ and M_i are covered.

With our 9-parameter MSSM specified, let us comment on some differences among the predictions of the scenario we consider and the most general MSSM. In our approach, SUSY is assumed to break at the gauge-coupling unification scale. Although the assumption is reasonable in gravity-mediated SUSY breaking scenarios, it is not the only possibility. For example, in gauge mediated scenarios, this may happen, in principle, at any scale. Moreover, the consequences of this assumption depend on how much freedom is given to the soft parameters. Imposing the above mentioned

	Gaussian prior	Range scanned	ref.
M_t [GeV]	173.2 ± 0.9	(167.0, 178.2)	[180]
$m_b(m_b)^{\bar{M}S}$ [GeV]	4.20 ± 0.07	(3.92, 4.48)	[181]
$[\alpha_{em}(M_Z)^{\bar{M}S}]^{-1}$	127.955 ± 0.030	(127.835, 128.075)	[181]
$\alpha_s(M_Z)^{\bar{M}S}$	0.1176 ± 0.0020	(0.1096, 0.1256)	[182]

Table 4.1: Relevant SM parameters, treated as nuisance parameters in the numerical analysis.

universality condition and the unification condition (right and left sfermions have equal masses, as well as $m_{H_u} = m_{H_d}$), produces a specific hierarchy for the squark and slepton masses; this hierarchy could be ameliorated by lowering the SUSY breaking scale. This means that other possible hierarchies of sfermion masses will not be probed in this scenario. In our case, for example, $\tilde{t}_1$ is always the lightest squark, and $\tilde{\tau}_1$ the lightest slepton. On the other hand, the universality condition does not introduce new sources of flavour changes, and consequently, is well motivated by the low energy experimental constraints from the flavour sector.

In the case of the phenomenological MSSM, the pMSSM mentioned in the previous Section, the parameterisation is taken at the EWSB scale and thus the sparticle masses do not "feel" the impact of the renormalization group equations (that is, there is almost no "room" for the renormalization group evolution)[5]. Correlations among parameters disappear, and the choice of priors most likely dominates the results, not allowing to draw conclusions about most probable regions, for example. Anyway, Bayesian analyses have been performed in the pMSSM from different perspectives [177, 178, 179], in order for example to identify better which parameters are directly constrained by experimental information (through the prior dependence of results in each parameter)

In the analysis, following the lines of reference [183], two different priors are considered: standard log priors, "S-log priors", that is log priors for each parameter independently, and improved log priors, "I-log prior", which assume a common origin for the soft masses, as expected from SUSY breaking mechanisms. The range of the parameters in the numerical analysis varies from 10 GeV to 10^6 GeV. Although both priors are based on a uniform dependence in logarithms, they are rather different from one another: the S-log priors, for example, favor large splittings between the parameters, while for the I-log priors, since a common origin for the soft parameters is assumed, this is not the case.

Basically, we assume a common scale with the values of the parameters being propor-

[5]Notice however that the universality condition is somehow taken into account in the pMSSM when setting sfermion masses in the first and second generations equal.

tional to that scale, which is to be marginalized over. Now, given the parameters θ_1 and θ_2 (with the same dimensions), in the standard log prior case, we would have

$$p(\theta_1, \theta_2) = \frac{1}{\theta_1} \frac{1}{\theta_2} \,. \tag{4.7}$$

In this case, consider two situations: (1) $\theta_1 \sim 10^{-10}$ and $\theta_2 \sim 10^{10}$, and (2) $\theta_1 \sim \theta_2 \sim 1$. The standard log prior assigns the same probability to both while we would rather favor the second case if θ_1 and θ_2 are proportional to a common scale. The I-log priors achieve that in a simple manner, with a prior of the form:

$$p(\theta_1, \theta_2) = \frac{1}{max(\theta_1, \theta_2)^2} \,. \tag{4.8}$$

That is, in the latter case, situations with either large or small values of some parameters, pay a probability penalty[6]. Notice, finally, that in this approach, which incorporates naturalness arguments, we are able to explore large ranges for the different parameters and obtain consistent results.

Concerning the experimental input considered in our analysis, it is described in Table 4.2: it covers electroweak precision measurements [184], some B-physics observables [185, 186, 187, 188, 189][7], the Higgs boson mass [194, 195], and constraints on the WIMP-nucleon scattering cross-section by XENON-100 [196]. In addition, we include the measured relic density according to the *Planck* collaboration results [197], since we are assuming a scenario with a single DM component which is thermally produced in the early Universe[8]

4.2.2 Tools

The numerical analysis involves the combined use of a number of tools (written in `Fortran` and `C++`, which we briefly describe now. `SuperBayeS-v2.0` is a set of routines for parameter extraction within a Bayesian statistical approach in supersymmetric scenarios. It implements the nested sampling `MultiNest` [149, 150] algorithm which, although oriented to the efficient computation of the Bayesian evidence, does also produce posterior probability distributions. `SuperBayeS` interfaces/handles: `Softsusy`

[6] We refer to Sec. 3.3 of reference [183] for a more detailed discussion on the priors.

[7] More recent values would be, for example, $\mathrm{BR}(\bar{B} \to s\gamma) = (3.43 \pm 0.22 \pm 0.07) \times 10^{-4}$ [190] (see also Refs. [191, 192]) and $\mathrm{BR}(\bar{B} \to \mu^+\mu^-) = 2.8^{+0.7}_{-0.6} \times 10^{-9}$ [193]. These measurements are still in agreement (within uncertainties) with the values that are adopted in the analysis, and therefore, their impact would not be large.

[8] We actually assume that 100% of dark matter consists of the neutralino. If there are other dark matter components, one would need to regard the measurement of the dark matter density determined by the Planck satellite as an upper limit, and follow some scaling ansaz as studied, e.g., in [198, 183].

Observable	Mean value	Uncertainties		Ref.
	μ	σ (exper.)	τ (theor.)	
M_W [GeV]	80.399	0.023	0.015	[199]
$\sin^2\theta_{eff}$	0.23153	0.00016	0.00015	[199]
$\mathrm{BR}(\overline{B}\to X_s\gamma)\times 10^4$	3.55	0.26	0.30	[200]
$R_{\Delta M_{B_s}}$	1.04	0.11	-	[186]
$\frac{\mathrm{BR}(B_u\to\tau\nu)}{\mathrm{BR}(B_u\to\tau\nu)_{SM}}$	1.63	0.54	-	[200]
$\Delta_{0-}\times 10^2$	3.1	2.3	-	[201]
$\frac{\mathrm{BR}(B\to D\tau\nu)}{\mathrm{BR}(B\to De\nu)}\times 10^2$	41.6	12.8	3.5	[187]
R_{l23}	0.999	0.007	-	[188]
$\mathrm{BR}(D_s\to\tau\nu)\times 10^2$	5.38	0.32	0.2	[200]
$\mathrm{BR}(D_s\to\mu\nu)\times 10^3$	5.81	0.43	0.2	[200]
$\mathrm{BR}(D\to\mu\nu)\times 10^4$	3.82	0.33	0.2	[200]
$\Omega_\chi h^2$	0.1196	0.0031	0.012	[202]
m_h [GeV]	125.66	0.41	2.0	[180]
$\mathrm{BR}(\overline{B}_s\to\mu^+\mu^-)$	3.2×10^{-9}	1.5×10^{-9}	10%	[189]
	Limit (95% CL)		τ (theor.)	Ref.
Sparticle masses	As in Table 4 of Ref. [203].			
$m_\chi-\sigma^{\mathrm{SI}}_{\chi N}$	XENON100 2012 limits (224.6×34 kg days)			[204][a]

Table 4.2: Observables used for the computation of the likelihood function. For each quantity, we use a likelihood function with mean μ and standard deviation $s=\sqrt{\sigma^2+\tau^2}$, where σ is the experimental uncertainty and τ represents our estimate of the theoretical uncertainty. Lower part: observables for which, at the moment, only limits exist. The explicit form of the likelihood function is given in ref. [203]. In particular, in order to include an appropriate theoretical uncertainty in the observables, the likelihood contains a smearing out of experimental errors and limits.

[a]Since this work was published, improved XENON100 limits have been presented in Refs. [205, 206].

[207] for the computation of the mass spectrum of the MSSM including one loop corrections, `micrOmegas` [208] for the computation of the DM relic density, `DarkSusy` [209] for the computation of direct[9] and indirect detection observables, `SusyBSG` [211] for the $b \to s\gamma$ computation within a Minimal Flavour Violating MSSM, and `Superiso` [212] for other B-physics observables. In addition, for the Wino-like and Higgsino-like LSP cases addressed in Section 4.4.1, the Sommerfeld enhancement[10] of the primordial and present day neutralino annihilation has been included, following the lines of references [215, 216, 217, 218], using `DarkSE` [219, 220], which is a package for `DarkSusy`.

4.3 Neutralinos and protohalos

As discussed in Chapter 2 and in the previous Sections, neutralinos are a clear example of a WIMP-type dark matter candidate. With the WIMP hypothesis, the abundance of DM originates from thermal decoupling in the early Universe. That is, when the processes of pair-annihilation and pair-creation of WIMPs go out of chemical equilibrium due to the Hubble expansion, the resulting number density freezes out and remains constant, per comoving volume, until the present time. As discussed in Section 1.4.2.1, this chemical decoupling, however, does not signal the end of the interactions of the WIMPs with the thermal plasma. There could still be elastic scattering processes with SM particles, which keep WIMPs in kinetic equilibrium until later time (without modifying the abundance). When the rate of those elastic scattering processes also falls below the Hubble expansion rate, the WIMPs enter the so-called *kinetic decoupling* epoch. From that moment on, WIMPs are decoupled from the thermal bath, and begin to free-stream. After this stage, the first gravitationally bound DM structures begin to form; their size is set by the temperature of kinetic decoupling, related to a small-scale cutoff in the primordial power spectrum of density perturbations.

In reference [84] the primordial power spectrum was calculated including collisional damping and free-streaming of WIMPs, showing that the free-streaming led to a cold DM power spectrum with a cutoff around a scale corresponding to the Earth mass $\sim 10^{-6}\, M_\odot$ (see also references [85, 86, 16, 23]). One of the most challenging goals

[9] For the contribution of the light quarks to the nucleon form factors, concerning the spin-independent WIMP-nucleon cross section, we have adopted the values $f_{Tu} = 0.02698$, $f_{Td} = 0.03906$ and $f_{Ts} = 0.36$ [210].

[10] The Sommerfeld enhancement [213] is a non-relativistic effect that depends on three quantities: the neutralino mass, the difference in mass between the neutralino and the next-to-lightest particle, and the size of the coupling among them. In this context, the Sommerfeld enhancement of the annihilation cross sections can significantly shift the neutralino mass consistent with the experimental $\Omega_{cdm}h^2$ value [214].

today is to shed light on the nature of the small-scale cutoff in the primordial power spectrum of density perturbations, often dubbed with the name of *protohalo*; protohalos are the smallest possible DM halos. Their properties are relevant for indirect DM searches. As introduced in Section 2.6.2, indirect DM detection looks for signatures of DM annihilation, such as gamma-ray photons, from dense celestial environments; there, the protohalo mass is a relevant quantity to determine the enhancement of the signal due to substructure, the "boost" factor. On the other hand, experiments of direct detection of DM (see Section 2.22), look for energy deposition in underground detectors due to scattering interactions between target nuclei and WIMPs around us; they give valuable information on the scattering cross sections, and (anticipating results presented in the following), through the correlations discussed in this study, they constrain the mass of the DM protohalos. Let us first discuss what is the smallest mass of the protohalos.

As mentioned, WIMP interactions with the plasma in the early Universe produce damping of the power spectrum before and after the kinetic decoupling. Before kinetic decoupling, WIMPs behave as a fluid tightly coupled to that plasma. Interactions produce shear viscosity in the WIMP fluid, causing the density perturbations (in that WIMP fluid) to oscillate acoustically in the heat bath [85, 86]. The damping scale set by these acoustic oscillations is given by the DM mass enclosed in the horizon at this epoch, i.e, the size of the horizon when kinetic decoupling occurs[24]:

$$M_{ao} \approx \frac{4\pi}{3}\frac{\rho_\chi(T_{kd})}{H^3(T_{kd})} = 3.4\times10^{-6}\,M_\odot\left(\frac{T_{kd}\,g_{eff}^{1/4}}{50\,\mathrm{MeV}}\right)^{-3}, \tag{4.9}$$

g_{eff} is the number of effective degrees of freedom in the early Universe and ρ_χ is the DM density, both evaluated at the temperature of kinetic decoupling, T_{kd}.

After kinetic decoupling, WIMP interactions give a free-streaming scale which induces a damping of density perturbations below a scale characterized by a (comoving) free-streaming wavenumber, k_{fs} [221, 84]. Therefore, if we have perturbations contained in a sphere of radius π/k_{fs}, we have the minimal mass of a DM protohalo, and then the mass of the smallest protohalo allowed by free-streaming is [24]:

$$M_{fs} \approx \frac{4\pi}{3}\rho_\chi\left(\frac{\pi}{k_{fs}}\right)^3 = 2.9\times10^{-6}\,M_\odot\left(\frac{1+\ln(g_{eff}^{1/4}T_{kd}/50\,\mathrm{MeV})/19.1}{(m_\chi/100\,\mathrm{GeV})^{1/2}g_{eff}^{1/4}(T_{kd}/50\,\mathrm{MeV})^{1/2}}\right)^3. \tag{4.10}$$

Both mechanisms, collisional damping and free-streaming of WIMPs, lead to a cutoff in the CDM power spectrum, from which the typical scale for the first haloes in the hierachical picture of structure formation is set. The canonical value for the mass of the DM protohalos is related to the nature of the DM particle. The SUSY based predictions for the size of the DM protohalos fall in a range from 10^{-11} to $10^{-3}\,M_\odot$

[24]. It is not clear, however, if these first and smallest halos survive until today, since they can be destroyed either in the process of merging or during galaxy formation by the so-called tidal stripping [70]. According to references [166, 222], the first halos lose their mass during structure formation, but survive until today with their inner density still intact.

For a typical WIMP one finds that the chemical-decoupling temperature is given by $T_{cd} \sim m/25$, where m is the WIMP mass, for an annihilation cross section $\langle \sigma v \rangle \sim 10^{-26}\,\mathrm{cm}^3\,\mathrm{s}^{-1}$, (appropriate in order to obtain the CDM relic density as observed today). On the other hand, the kinetic-decoupling temperature and, therefore, the minimal protohalo mass, are not well constrained for WIMPs. A reference value of the minimal protohalo mass for SUSY candidates is $\sim 10^{-6}\,M_\odot$, which was computed by assuming a Bino-neutralino scattering with the SM particles through sfermions with a mass of around twice the neutralino mass [16, 223, 224, 221]. The chosen nature of the neutralino and the particular relation between the sfermions and Bino neutralino was well motivated by a constrained SUSY extension of the SM (CMSSM), where the typically light neutralinos (lighter than 1 TeV) that are able to reproduce the correct relic density are mostly Bino that, efficiently, annihilate through sfermions in the early Universe.

Even though $M_{\mathrm{ph}} \sim 10^{-6}\,M_\odot$ was a good estimate of the value of the smallest mass of the DM protohalos for a "well motivated" neutralino, it is not a strong prediction for a general neutralino DM. As described in [225], there are several ways to get a well tempered neutralino; in a low-energy supersymmetric scenario, possible solutions that reproduce the correct DM density are a pure Bino, a pure Higgsino or a pure Wino. The Bino-neutralino, that annihilates through sfermions, is one of those possibilities. Reference [24] performed a general study of the chemical and kinetic decoupling temperatures T_{cd} and T_{kd} for the MSSM neutralino: as expected, $m/T_{cd} \sim 25$, while m/T_{kd} has a range of variation of almost four orders of magnitude, leading to a range in $M_{\mathrm{ph}} \sim 10^{-12}$–$10^{-3}\,M_\odot$. The reason of the big range of T_{kd} is that the interactions involved in the annihilation of neutralinos, the ones which are constrained by the relic density, are not necessarily the relevant ones for the "last" scattering of neutralinos with the plasma, and, therefore, the relic density value does not constrain them. For example, in the case of Wino-like or Higgsino-like neutralinos, the annihilation products are mainly gauge bosons, whose interactions involve different couplings with respect to the ones involved in the neutralino-fermion scattering.

It is important to mention that the computation of the kinetic decoupling temperature, and hence of the smallest protohalo mass, becomes more complicated when the decoupling occurs close to the Quantum Chromodynamics (QCD) phase transition. As mentioned above, the computation of T_{kd} and M_{ph} is performed with `DarkSusy`, following the lines described in reference [24]. For the case of two light (u, d) and

one massive s quarks, the critical temperature is assumed to be $T_c = 154$ MeV. The plasma is described including three quarks and gluons for a temperature $T > 4T_c$. Therefore, in the following analysis, for the regions where the kinetic decoupling temperature lies between T_c and $4T_c$ ($154\,\mathrm{MeV} < T_{kd} < 616\,\mathrm{MeV}$), T_{kd} will represent an upper bound while M_{ph} a lower bound.

4.4 Results

4.4.1 Most probable regions

The temperature of kinetic decoupling, the mass of the smallest protohalos and the mass of the neutralino are the most relevant quantities involved in the analysis. Figure 4.3 shows the two dimensional joint posterior PDF for the temperature of kinetic decoupling, T_{kd}, and for protohalo mass, M_{ph}, against the neutralino mass $m_{\chi_1^0}$. The contours represent 68% and 95% probability regions. As mentioned in subsection 4.2.1, we refer to 3.2.1 for details of the Bayesian analysis. One can clearly distinguish two most probable regions, around ~ 1 TeV and ~ 3 TeV. They correspond to a Higgsino-like and to a Wino-like neutralino, respectively. Both the Higgs mass

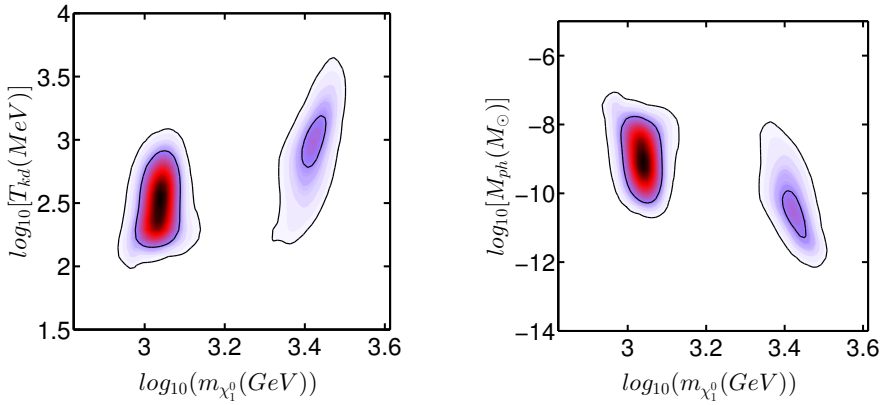

Figure 4.3: The two dimensional joint posterior PDF for kinetic decoupling temperature, T_{kd}, versus the neutralino mass (left panel), and for the protohalo mass, M_{ph}, versus the neutralino mass (right panel). The region with higher probability density (with $m_{\chi_1^0} \sim 1$ TeV) corresponds to a Higgsino DM candidate, while in the second region the DM candidate is a Wino.

measurement and the relic density constraint, as discussed in [183], are the main responsibles for the shift of the preferred regions towards high masses. Of course, it is important to stress that the credibility intervals represent the most probable regions

assuming the model that we consider is correct. In other words, the credibility regions show relative probability densities within the model. Values outside the regions can be disfavored because they have worse likelihoods and/or because they require a large tuning to reproduce the experimental data (less volume in parameter space). Concerning the prior dependence of our Bayesian analysis, the stability of the results has been checked by using the two different priors (I-log and S-log priors) introduced before: the results are basically unchanged (they are prior independent). Further details on those two regions are addressed in connection with the implications for direct detection in Section 4.5.1.

4.4.2 Profile likelihood maps

The most probable neutralino mass regions are those around 1 TeV and 3 TeV. As already stressed, this does not imply that there are no valid points in other regions like, for example, for neutralinos in the intermediate region between 1 TeV and 3 TeV. One can have points with good likelihood but outside the 95% probability regions showed in Figure 4.3 because (larger) fine-tunings are required to reproduce the experimental data and the correct EWSB.

In this subsection we study scenarios that reproduce all the observables within 2σ confidence level. To this end, a new exploration is performed by requiring a non-negligible Bino component for the lightest neutralino. In this way, we complete the previous exploration on Higgsino-like and Wino-like neutralinos, including all the different neutralino natures. Bounds on sparticle masses based on simplified models, as detailed in Table 4.3, are included. To apply these simplified model limits, production cross sections published by the LHC SUSY Cross Section Working Group [226], are used, including interpolation routines for gluino, squark and neutralino-chargino production. The slepton production cross section has been computed using PYTHIA 8 [227, 228]. Constraints from the signal strengths of the Higgs measurements by ATLAS [229] are also included[11]. For the computation of the branching ratios, we used SUSY-HIT [231].

Figure 4.4 shows points that reproduce the experimental data within 2σ confidence level. We show the lightest neutralino mass as a function of the kinetic decoupling temperature, T_{kd} (top), and the protohalo mass, $M_{\rm ph}$ (bottom). Let us describe the mass spectrum. The characteristics of the electroweakino sector[12] are set mainly by the fact that an efficient neutralino annihilation is needed to reproduce the correct

[11] More recent and detailed results, in particular [230], have appeared since the analysis was done.

[12] The Bino and Wino masses, together with both the Higgsino mass term, μ, and the ratio of up and down Higgs's vacum expectation values, $\tan\beta$, are referred to as *electroweakino sector* of the MSSM.

Topology			Refs.
Production	Decay	Comment	
$\tilde{t}_1\tilde{t}_1$	$\tilde{t}_1 \to bW^{(*)}\tilde{\chi}_1^0$	$m_{\tilde{t}_1} \ll m_{\chi_1^\pm}$	[232]
$\tilde{t}_1\tilde{t}_1$	$\tilde{t}_1 \to t\tilde{\chi}_1^0$	all hadronic	[233]
$\tilde{b}_1\tilde{b}_1$	$\tilde{b}_1 \to b\tilde{\chi}_1^0$		[234]
$\tilde{g}\tilde{g}$	$\tilde{g} \to b\bar{b}\chi_1^0$	$m_{\tilde{q}} \gg m_{\tilde{g}}$	[235]
$\tilde{g}\tilde{g}$	$\tilde{g} \to t\bar{t}\chi_1^0$	$m_{\tilde{q}} \gg m_{\tilde{g}}$, 0 leptons + 3 b-jets channel	[235]
$\tilde{g}\tilde{g}$	$\tilde{g} \to q\bar{q}\chi_1^0$	$m_{\tilde{q}} \gg m_{\tilde{g}}$	[169]
$\tilde{g}\tilde{g}$	$\tilde{g} \to b\bar{t}\chi_1^\pm$	$m_{\tilde{q}} \gg m_{\tilde{g}}$, $m_{\chi_1^\pm} - m_{\chi_1^0} = 2$ GeV	[235]
$\tilde{q}\tilde{q}$	$\tilde{q} \to q\chi_1^0$	$m_{\tilde{g}} \gg m_{\tilde{q}}$	[169]
$\chi_1^\pm\chi_2^0$	$W^{(*)}\chi_1^0 Z^{(*)}\chi_1^0$	$m_{\chi_1^\pm} = m_{\chi_2^0}$	[236]
$\tilde{l}_L^\pm\tilde{l}_L^\mp$	$\tilde{l}_L^\pm \to l^\pm\chi_1^0$		[236]
$\tilde{l}_R^\pm\tilde{l}_R^\mp$	$\tilde{l}_R^\pm \to l^\pm\chi_1^0$		[236]
$\tilde{l}_{LR}^\pm\tilde{l}_{LR}^\mp$	$\tilde{l}_{LR}^\mp \to l^\pm\chi_1^0$		[236]

Table 4.3: Exclusion limits in simplified models included in the analysis. The luminosity for each process is $\sim 20.3\,\text{fb}^{-1}$.

relic density. To identify regions where the lightest neutralino co-annihilates with sfermions in the early Universe, in both left panels we highlight points that satisfy a criterion based on the mass difference between the lightest neutralino and the lightest stau (green points), and between the lightest neutralino and the lightest stops (blue points). To select those points we have required a maximal relative mass difference, $\Delta(m_{\tilde{f}} - m_{\chi_1^0})$, of 5% and a maximal absolute mass difference of 5 GeV which are imposed for neutralino masses above and below 100 GeV, respectively. The gray band of the top-left panel shows the range of temperatures where the QCD phase transition occurs, from one to four times the critical temperature, where the value of T_{kd} represents an upper bound. Those points with T_{kd} around the QCD phase transition are represented with lighter colors in the $m_{\chi_1^0}$–M_{ph} plane in the bottom-left panel, where in this case the value of M_{ph} represents a lower bound.

Most of the points in Fig. 4.4 have a neutralino quasi-degenerate with another sparticle. Higgsino-like and Wino-like lightest neutralinos are quasi-degenerate with the lightest chargino, guaranteeing both a very efficient annihilation of neutralinos and co-annihilation with charginos, and selecting rather heavy neutralino masses. Neutralinos with a dominant Higgsino or Wino component cover the mass region of[13] $m_{\chi_1^0} \gtrsim 1$ TeV. As commented above for the most probable regions, for pure-Higgsino and pure-Wino neutralino, the relic density constraint fixes the mass to ~ 1 TeV and

[13] Assuming DM is made of several species, the relic density constraint becomes an upper bound, allowing to have lighter Higgsino-like and Wino-like neutralinos.

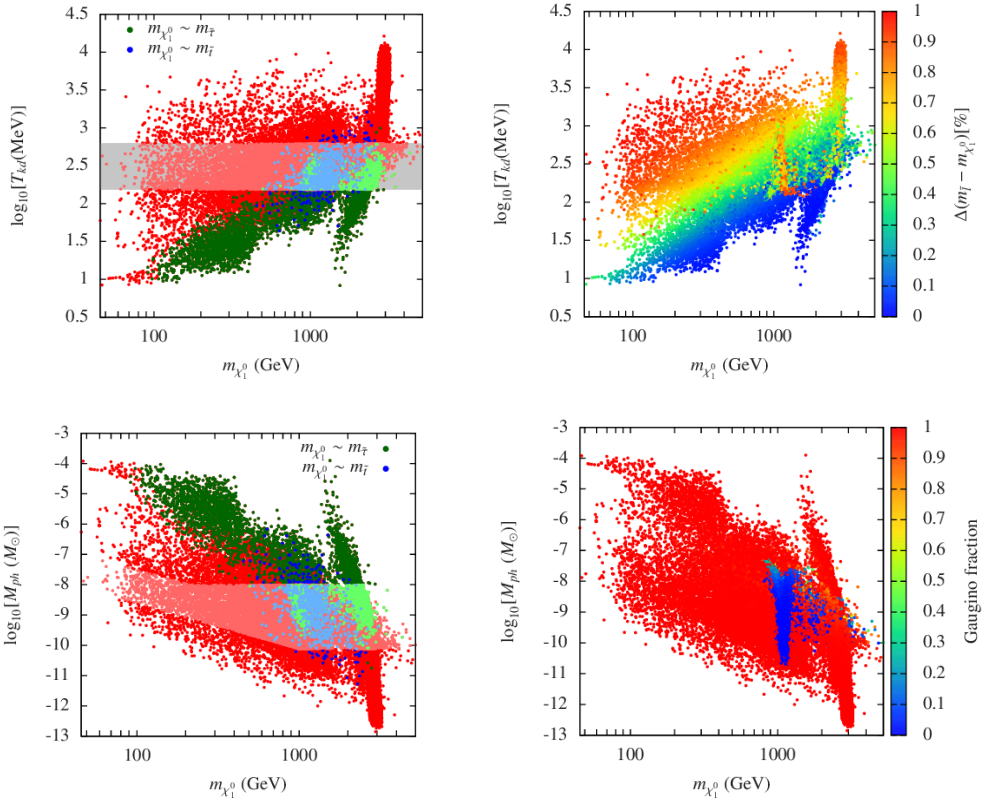

Figure 4.4: Lightest neutralino mass versus T_{kd} (top panel) and $M_{\rm ph}$ for points that reproduce all the experimental observables within 2σ confidence level.

~ 3 TeV, respectively. As a result of this scan, we have identified different mixed states lying between these regions: Higgsino-Wino neutralinos, Higgsino-like and Wino-like neutralinos that co-annihilate with staus or stops, and Wino-Bino neutralinos and Higgsino-like neutralinos with a mass equal to half of the mass of the pseudoscalar. Some of the points with $m_{\chi_1^0}$ slightly below 1 TeV are Higgsino-Bino neutralinos. This region is strongly constrained by direct detection experiments like Xenon100 and LUX.

Points with $m_{\chi_1^0} \lesssim 1$ TeV have a lightest Bino-like neutralino. For 100 GeV $\lesssim m_{\chi_1^0} \lesssim$ 600 GeV, it is possible to distinguish two groups of points in the bottom-left panel of Fig. 4.4. The first group has smaller T_{kd}, ranging from $\sim$ 10 MeV to $\sim$ 100 MeV and is basically aligned to the stau co-annihilation region. For these points sleptons are light, and the correct neutralino abundance was reached by slepton-neutralino co-annihilation in the early Universe. Charginos and heavier neutralinos

are typically much heavier. For the second group of points with larger T_{kd} varying from $\sim$ 100 MeV to $\sim$ 3 GeV, we checked that the lightest (Bino-like) neutralino is quasi-degenerate with both the lightest Wino-like chargino and the second lightest neutralino, guaranteeing the neutralino annihilation. Top-right panel of Fig. 4.4 shows that these two regions are not completely disconnected. For example, for $m_{\tilde{l}} - m_{\chi_1^0} \sim 0.5(m_{\tilde{l}} + m_{\chi_1^0})$, sleptons also play a role in the annihilation processes. The region 600 GeV $\lesssim m_{\chi_1^0} \lesssim$ 1 TeV has similar characteristics, but in this case the two regions, the one with light sfermions and the one with light charginos, have a large overlap for 30 MeV $\lesssim T_{\rm kd} \lesssim$ 500 MeV.

Last but not least, we find that there are very few points for the Higgs and Z resonance regions. These two regions require a very large tuning, and therefore, they are very difficult to explore when requiring boundary conditions at the GUT scale.

To understand the dominant process of neutralino-SM scattering in the regions described above, in the top-right panel of Fig. 4.4 we show the relative mass difference between the lightest first and second generation of sleptons and the lightest neutralino, $\Delta(m_{\tilde{l}} - m_{\chi_1^0})$, while in the bottom-right panel we show the gaugino fraction[14]. These plots show, for all gaugino-like neutralinos (Bino-like or Wino-like), a clear correlation between the lightest neutralino mass and the kinetic decoupling temperature for a fixed value of $\Delta(m_{\tilde{l}} - m_{\chi_1^0})$. Higgsino-like neutralinos around 1 TeV do not show a correlation for specific sleptons masses; their interaction with sfermions is proportional to the Yukawa coupling, and it is therefore negligible for the first and the second generations of sleptons. In the Higgsino-like case the dominant interaction is the one mediated by the Z-boson, as in the case of Bino-like and Wino-like neutralinos when sfermions are decoupled.

As discussed in Section 4.2.1, we assume universality and unification of the squarks and slepton masses. These conditions imply that $\tilde{t}_1$ and $\tilde{\tau}_1$ are the lightest squark and slepton, respectively, which is the reason why we only find neutralino-stop and neutralino-stau co-annihilation regions in our analysis. In more general scenarios where sfermions masses do not unify, the possibility of having co-annihilation with any sfermion is open, since any of them could be the next-to-LSP. If the lightest neutralino is Bino-like and the first or second generation sfermions are close enough in mass to the lightest neutralino to guarantee a large enough effective annihilation in the early Universe, then the dominant interaction in the scattering between the lightest neutralino and the SM particles will be the same interaction (neutralino-fermion-sfermion), producing a strong correlation between the mass of the lightest neutralino and $M_{\rm ph}$.

[14] We remind that the lightest neutralino is a linear combination of the superpartners of the gauge and Higgs field: $\chi_1^0 = N_{11}\tilde{B} + N_{12}\tilde{W}^3 + N_{13}\tilde{H}_1^0 + N_{14}\tilde{H}_2^0$. The gaugino fraction is defined by $Z_g \equiv |N_{11}|^2 + |N_{12}|^2$ (see [237] for details).

Another consequence of universality and unification is that the first and second generations of squarks are in general very heavy (due to the Higgs mass constraint on the stop sector), having, in most of the cases, a negligible contribution to the neutralino annihilation and neutralino scattering with the SM particles in the early Universe.

Without this assumption, the most important constraint on squark masses will come from the LHC bounds and direct detection experiments, allowing smaller masses. Due to the strong lower bounds on the first and second generation squarks masses coming from the LHC [238], one would expect that sleptons will still give the dominant contribution to the neutralino annihilation and neutralino scattering with the SM particles in the early Universe for neutralinos lighter than 300 GeV. However, for neutralino masses larger than 300 GeV, contributions from first and second generation squarks could be sizeable. Interestingly, the cases that set the smaller value of $M_{\rm ph}$, when sleptons are very close in mass to the mass of the lightest neutralino, and larger values of $M_{\rm ph}$, when sleptons are decoupled and the scattering is mediated by Z-boson, are covered in our analysis. On the other hand, the implications on direct detection, indirect detection and on LHC prospects, could be different, as discussed in the next Section.

The understanding of the interactions that play a relevant role in the annihilation and scattering of neutralinos with SM particles helps us to identify correlations between $M_{\rm ph}$ and the SUSY spectrum. These correlations could be very helpful for constraining T_{kd} indirectly from current DM experiments. In particular, the region of $m_{\chi_1^0} \lesssim 600$ GeV could be potentially tested by the LHC, as discussed in Section 4.5.3.

4.5 Implications

4.5.1 Direct detection

As discussed in Section 2.6.1, direct detection experiments of DM look for energy deposition in detectors (typically underground to suppress backgrounds) caused by scattering interactions between target nuclei and DM WIMPs around us. The measurement or the bound on this cross section has direct consequences on the value of the kinetic decoupling temperature T_{kd}, assuming that the processes involved in the last scattering are the same as the ones producing the scattering of the DM with the material in the detector. Before addressing the implications in terms of correlations arising in the analyses, let us first comment some relevant features associated to the most probable regions.

The region around 1 TeV corresponds to a Higgsino-like neutralino. Its annihilation cross section is driven by its Higgsino component (the main annihilation processes are those of a pure Higgsino-neutralino). On the other hand, for the scattering cross section, the small components of Wino and Bino play a crucial role. The reason is the following. Assuming that sfermions are heavy enough to be considered decoupled, the tree level SD scattering of Higgsino-like neutralino with fermions is mediated by the Z boson. In the limit of pure Higgsino-neutralino, $\tilde{H}_u$ and $\tilde{H}_d$ are degenerate, and since they have opposite quantum numbers, their contributions cancel. But then, when the gaugino masses are not decoupled, the $\tilde{H}_u$ and $\tilde{H}_d$ composition of the lightest neutralino is not the same, and the cancellation does not occur. Regarding the tree level SI scattering[15], the interaction is mediated by the Higgs boson, and as it interacts with the neutralinos via a Higgsino-Bino(Wino)-Higgs coupling, a nonzero gaugino component is necessary in order to have a nonzero tree level contribution. In this region sfermions are not necessarily decoupled. However, since the Higgsino-sfermion-fermion interaction is proportional to the Yukawa coupling[16], these contributions are negligible.

The region around 3 TeV corresponds to a Wino-like neutralino, where the most important annihilation interactions are those of the pure Wino neutralino. The part of the region closer to ~ 2.5 TeV has also important contributions from the neutralino-stau co-annihilation[17], reducing the effective annihilation rate of neutralinos in the early Universe and, therefore, decreasing the value of the neutralino mass to obtain the correct relic density, that for the case of pure Wino is ~ 3 TeV. As in the Higgsino-like neutralino case, the tree level SD neutralino-fermion scattering cross section receives an important contribution from the Z boson, which is the mediator of this interaction, while the tree level SI neutralino-fermion scattering cross section receives it from a Higgs. In both cases, a non-negligible component of Bino or Higgsino is needed to have a tree-level contribution to these processes, since $\tilde{W}^0$–$\tilde{W}^0$–Z and $\tilde{W}^0$–$\tilde{W}^0$–h interactions do not exist. In addition, sfermions give an important contribution to the neutralino-fermions scattering cross sections, in particular for Wino-neutralinos with mass ~ 2.5 TeV. As we commented above, in this region staus are close in mass to the lightest neutralino, and selectrons and smuons are light enough to give a sizeable

[15] We still assume that sfermions are decoupled.

[16] We remind that at temperatures of the order of MeV, when the kinetic decoupling occurs, the population of third generation of fermions is very small.

[17] Sometimes, solving the Boltzmann equation for the evolution of the neutralino number density to obtain the correct relic abundance of DM requires additional considerations; degeneracies in mass between the lightest neutralino and the next to lightest one, or the presence of thresholds and resonances in the annihilation cross section may be relevant (see, e.g., the review [239]). In particular, when the lightest neutralino is close in mass to a heavier neutralino, the relic abundance is determined both by its annihilation cross section and by co-annihilation with this heavier partner which, then, decays into the lightest one. Co-annihilations may also occur with squarks, when they happen to be very close in mass to the lightest neutralino.

contribution to the scattering cross section.

Reference [87] analyzed correlations between the mass of protohalos $M_{\rm ph}$, the temperature of kinetic decoupling T_{kd} and the spin dependent and spin independent scattering cross sections. Such correlations appear when the masses of the squarks are assumed to be large, $m_{\tilde{q}} \simeq 5 - 10$ TeV[18], and the dominant process for the scattering is the exchange of a Z boson. In Fig. 4.5, we show the most probable

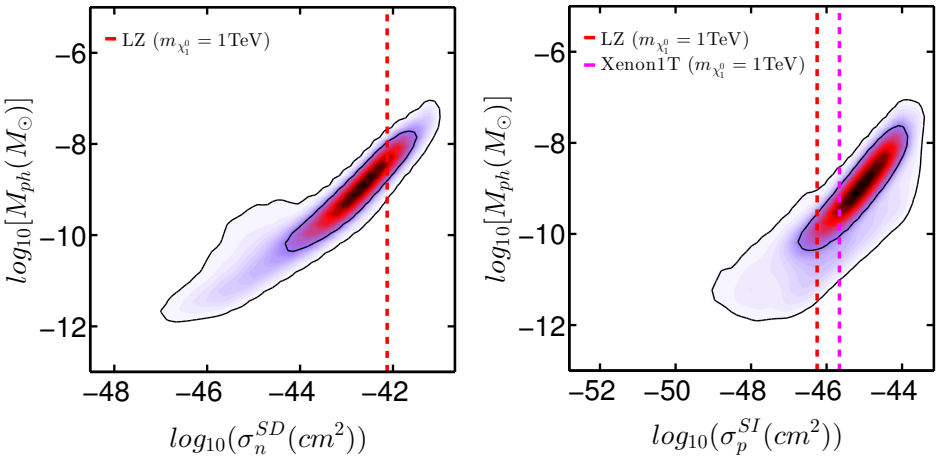

Figure 4.5: Most probable regions on the scattering cross section–protohalo mass plane. The left and right panels show the correlation with the spin-dependent and spin-independent cross sections, σ_n^{SD} and σ_p^{SI}, respectively.

region on the plane of the protohalo mass, $M_{\rm ph}$, and the SD and the SI cross sections computed at tree level. Contrary to Fig. 4.3, the probability regions do not have disconnected parts, but they include both Higgsino-like (at ~ 1 TeV) and Wino-like (at ~ 3 TeV) neutralinos. In both cases the dominant scattering process is mediated by the Z-boson. We see how the expected improvement on the SI sensitivity by, e.g., the Xenon1T [240] and the LUX-Zeppelin experiments (LZ) [241], will reduce the most probable range of the minimal subhalo mass down to below $\sim 10^{-9}$ $M_\odot$, while the expected SD sensitivity provides weaker constraints. Since in the analysis we have included the XENON100 limits as constraints on the WIMP-nucleon scattering cross section, we see in the right panel of Fig. 4.5 that the region around $\sigma_p^{SI} \approx 2 \times 10^{-44}$ cm^2 is strongly penalized. The current LUX bound is more stringent on the spin-independent sensitivity, giving an upper bound of $\sigma_p^{SI} \approx 10^{-44}$ for a 1 TeV neutralino [242], although we did not include it in our analysis[19]. Including the LUX bound,

[18]The authors of ref. [87] used the squark mass to show the effect of light sfermions in the correlation, but clarify that when the correlation is broken, the relative contribution from sleptons, especially the slepton exchange in the kinetic decoupling process, increases.

[19]Since this work was published, the LUX experiment has released updated results [243], and

therefore, would affect the very right part of the right panel of Fig. 4.5 (and also Fig. 4.7 shown below). However, since the regions affected are tiny, it will not affect our conclusions. Figure 4.6 shows points that reproduce the experimental constraints

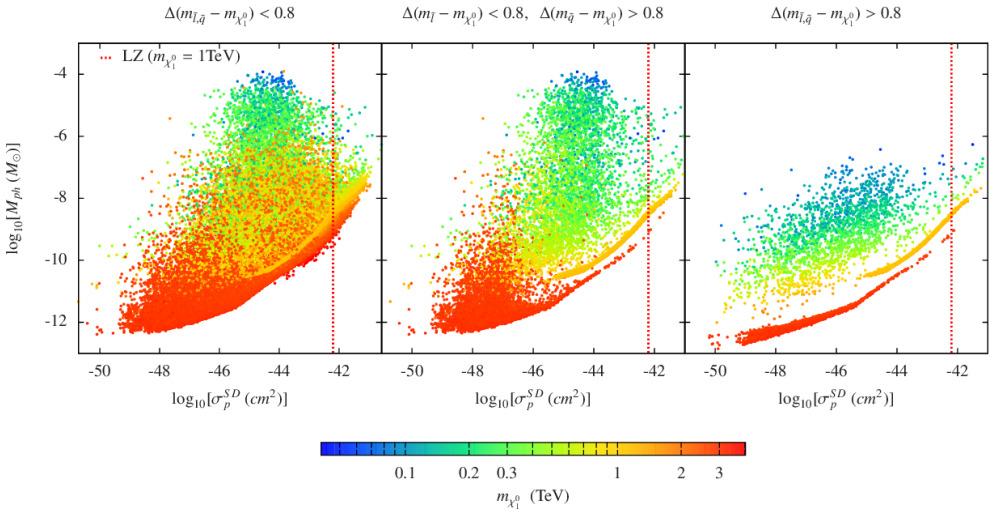

Figure 4.6: Points that reproduce all the experimental observables at 2σ confidence level in the SD cross section σ_p^{SD} versus protohalo mass $M_{\rm ph}$ plane. The neutralino mass is indicated with colors, as shown in the color bar. The three panels separate the points in three groups: light squarks and sleptons (left panel), light sleptons and decoupled squarks (central panel), and decoupled squarks and sleptons (right panel).

at the 2σ confidence level for the minimal protohalo mass versus the tree level SD cross section plane. The right panel shows the case where the lightest first or second generation of sfermions is at least nine times heavier than the lightest neutralino, $\Delta(m_{\tilde{l}\,\tilde{q}} - m_{\chi_1^0}) > 0.8$. The thin yellow line corresponds to a ~ 1 TeV Higgsino-like neutralino, while the thin red line to a ~ 3 TeV Wino-like neutralino. In these two cases the Z-boson mediates both scattering processes. The rest of the points correspond to the Bino-like neutralino where, instead of a line, we obtain scattered points with 100 GeV $\lesssim m_{\chi_1^0} \lesssim 1$ TeV. We remind that for the Bino-like case, the annihilation cross section and, therefore, the relic density, can be adjusted varying the neutralino mass and its mass splitting with respect to the lightest (Wino-like) chargino. On the other hand, even if they are ten times heavier than the lightest neutralino, sleptons mediate the dominant scattering processes that set T_{kd} for most of the points. The size of the contribution of processes mediated by the Z-boson, depends on how large the Higgsino component of the neutralino is. However, the Higgsino component of a Bino-like neutralino is highly constrained by SI cross sections bounds. Nevertheless,

improved XENON100 limits have been presented in Refs. [205, 206].

as commented previously, there are some blind spots for SI cross sections. For those points, the Z-boson gives an important contribution to the scattering cross section.

Regarding $\sigma_p^{\rm SD}$ for the Bino-like region, the dominant process is mediated by the Z-boson[20]. Despite the dominant scattering processes for T_{kd} and $\sigma_p^{\rm SD}$ being different, there is an apparent correlation between the two quantities for a fixed neutralino mass. We have checked the behavior of the correlation for specific values of $m_{\chi_1^0}$, finding that T_{kd} spreads around one order of magnitude for a given value of $\sigma_p^{\rm SD}$.

The central panel of Fig. 4.6 shows the case where the lightest slepton has a mass smaller than ~ 10 times the lightest neutralino mass. As expected, the Wino-like and Bino-like regions spread to larger protohalo masses[21]. The left panel of Fig. 4.6 shows the case where the lightest sleptons and squarks are lighter than ~ 10 times the lightest neutralino. In that case, squarks are light enough to give important contributions to the scattering with the nucleus, spreading the points to larger values of σ_n^{SD}. Figure 4.7 shows points in the minimal protohalo mass versus tree level

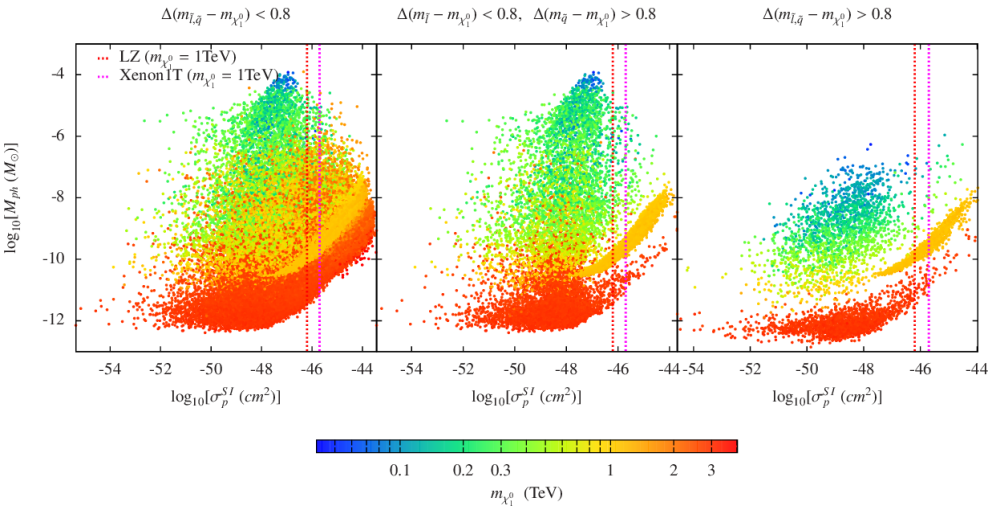

Figure 4.7: Same as Fig. 4.6 for the the SI cross section, σ^{SI}.

SI cross section plane. The main contribution to the SI cross section comes from the Higgs exchange, requiring a non-negligible Higgsino and Wino/Bino coupling

[20]Squarks are typically heavier than sleptons when parameterizing the model at the gauge coupling unification scale. Therefore, imposing the condition $\Delta(m_{\tilde{l}} - m_{\chi_1^0}) > 0.8$ implies that squarks are typically much heavier than ten times the mass of the lightest neutralino.

[21]Winos and Binos have strong SD interactions since diagrams where the incoming and outgoing fermions have the same helicity are allowed. On the other hand, the diagrams where the incoming and outgoing fermions have opposite helicities are spin-independent, requiring a $q\tilde{q}\tilde{H}$ vertex to yield the helicity flip, which is Yukawa suppressed. For a review, see Ref [244].

(since Higgs couplings to neutralinos are $H\tilde{H}\tilde{B}$ and $H\tilde{H}\tilde{W}$). On the other hand, the total neutralino-SM scattering, and therefore T_{kd} and $M_{\rm ph}$, are dominated by SD interactions. As a consequence, right panel of Fig. 4.7 shows the correlation between the $Z\chi_1^0\chi_1^0$ and $H\chi_1^0\chi_1^0$, for the Higgsino and Wino case. Central and left panels show the effect of sleptons and squarks in the scattering processes.

Figures 4.6 and 4.7 show the expected sensitivity of Xenon1T and LZ assuming that the neutralino mass is ~ 1 TeV. For a neutralino of ~ 100 GeV, the expected sensitivity is around one order of magnitude stronger.

As we commented in precedence, assuming universality and unification of the squark and slepton masses, we impose a particular mass hierarchy: $\tilde{t}_1$ is the lightest squark and $\tilde{\tau}_1$ is the lightest slepton. Without this assumption, the first and second generations of sfermions can be lighter and change the phenomenology for direct detection experiments and colliders. When the lightest neutralino is gaugino-like and the first and second generations of squarks are the lighter sfermions, T_{kd} will be completely correlated with the neutralino-nucleon scattering cross section. Still, if they are not the lightest ones but they are significantly lighter than in our analysis, the neutralino-nucleon scattering cross section could increase, taking values close to the actual limits. In addition, if they are lighter or close in mass to the first and second generation sleptons, the scattering of the neutralino with SM particles in the early Universe could also increase. Those points will most likely populate the top-right corner of the left panel of Figs. 4.6 and 4.7.

Finally, we remind that the scattering cross sections considered in this work were computed at tree level. In the cases where the neutralino approaches a pure state (Bino, Wino or Higgsino), this approximation may not give a reliable result. In particular, in the case of the Wino-neutralino, one loop corrections give the dominant contributions (see, e.g., Ref. [245, 246]).

4.5.2 Indirect detection

One of the most reliable methods to model the non-linear evolution of DM is numerical simulation, although it is limited by mass resolution. In fact, the minimum self-bound mass (M_{min}) of DM halos is expected to be many orders of magnitude below the resolution of current simulations. Through numerical simulations such as *Acquarius* [72], we can obtain information on the subhalo hierarchy, although its resolution mass limit $\sim 10^4$ or $\sim 10^5 M_\odot$ is far from the predicted protohalo mass shown in Sections 4.4.1 and 4.4.2.

Here we investigate the impact of different values of M_{min} on the gamma-ray luminosity due to DM annihilation, and compute the boost factor of a given halo of mass M

due to the substructure inside it, by integrating the subhalo annihilation luminosities from the protohalo mass we have found, $M_{\rm ph}$, up to the mass of a sizable fraction of the host halo $M_{\rm max}$. The total luminosity of the DM halo due to annihilation is proportional to:

$$L \propto \int_{M_{\rm ph}}^{M_{\rm max}} dM \, \frac{dn}{dM} \, L_{\rm sh}(M) \, , \tag{4.11}$$

where dn/dM is the subhalo mass function, i.e. the subhalo number density per unit mass range. Numerical simulations find that the differential subhalo mass function follows a power law $dn/dM \propto M^{-\beta}$, with $\beta \sim 1.9$ or $\beta \sim 2$ (see, e.g. [70, 247]). We adopt a M^{-2} subhalo mass spectrum as our fiducial subhalo model.

We assume that each individual DM subhalo is described by a Navarro-Frenk-White density profile [248]:

$$\rho_{sh} = \frac{\rho_s}{(r/r_s)(1 + r/r_s)^2} \, , \tag{4.12}$$

where ρ_s and r_s are the characteristic density and radius, respectively. $L_{\rm sh}(M)$ is defined as the luminosity of each subhalo in the host halo, which depends on the volume integral of the subhalo density squared, and is given by:

$$L_{\rm sh}(M) = \int dV_{sh} \, \rho_{sh}^2 \propto \rho_s^2 \, r_s^3 \, . \tag{4.13}$$

Following the approach of Ref. [249], we parameterize the scaling relation between the gamma-ray luminosity and subhalo mass as:

$$L_{\rm sh}(M) \propto L_0 \times \begin{cases} \left(\frac{M}{10^4 \, M_\odot}\right)^{0.77} \, , & M > 10^4 \, M_\odot \\ \left(\frac{M}{10^4 \, M_\odot}\right)^{\gamma} \, , & M < 10^4 \, M_\odot \, , \end{cases} \tag{4.14}$$

where above the simulation resolution of $\sim 10^4 \, M_\odot$, the luminosity versus subhalos mass scales as $L \propto M^{0.77}$, while below the resolution we assume $\gamma < 1$. Here, L_0 encodes all the particle physics, i.e., $L_0 \propto \langle \sigma v \rangle / m^2_{\chi^0_1}$, where $\langle \sigma v \rangle$ is the velocity-averaged annihilation cross section times the relative velocity [22]. In order to obtain the scaling behavior of $L_{\rm sh} \propto M^{0.77}$, we adopted scaling relations among several quantities found in the *Aquarius* numerical simulation. Since each subhalo is described by a NFW density profile, we related the maximum rotation velocity of the subhalo, $V_{\rm max}$, and the radius at which the rotation curve reaches this maximum, $r_{\rm max}$, with the characteristic density and radius, ρ_s and r_s, to obtain them as a function of the subhalo mass M. These empirical relations between ($V_{\rm max}$, $r_{\rm max}$) and (ρ_s, r_s), however, loose validity in the mass regions below the resolution limit of the simulation. For this reason we split Eq. (4.14) in two terms, above and below the resolution ($10^4 M_\odot$),

[22] In the considered MSSM, for almost all the data points, we find that the annihilation cross section, $\langle \sigma v \rangle$, is almost independent of velocity, $\langle \sigma v \rangle \approx (\sigma v)_0$.

where in the latter we put γ as a phenomenological parameter describing the scaling behavior. The luminosity in Eq. (4.11) can be then written as:

$$L \propto \frac{\langle\sigma v\rangle}{m^2_{\chi^0_1}} \left[\int_{M_{\rm ph}}^{10^4\, M_\odot} dM\, M^{-2} \left(\frac{M}{10^4\, M_\odot}\right)^{\gamma} + \int_{10^4\, M_\odot}^{M_{\rm max}} dM\, M^{-2} \left(\frac{M}{10^4\, M_\odot}\right)^{0.77} \right] . \quad (4.15)$$

Assuming that the first term dominates, the luminosity is, thus, a function of the protohalo mass:

$$L(M_{\rm ph}) \sim \frac{\langle\sigma v\rangle}{m^2_{\chi^0_1}} \left(\frac{M_{\rm ph}}{10^4\, M_\odot}\right)^{\gamma-1} . \quad (4.16)$$

For comparison, we define a reference value for such a luminosity, $L_{\rm ref}$, as:

$$L_{\rm ref} \propto \frac{\langle\sigma v\rangle_{\rm ref}}{m^2_{\chi^0_1}} \left(\frac{M_{\rm ref}}{10^4\, M_\odot}\right)^{\gamma-1} . \quad (4.17)$$

For values of these reference parameters, we adopt $\langle\sigma v\rangle_{\rm ref} = 3\times10^{-26}\,{\rm cm}^3\,{\rm s}^{-1}$, $M_{\rm ref} = 10^{-6}\,M_\odot$, and $\gamma = 0.8$.

The left panel of Fig. 4.8 shows the two-dimensional joint posterior PDF for the protohalo mass $M_{\rm ph}$ and $\langle\sigma v\rangle$ with 68% and 95% probability contours. These most probable regions fall in a mass range between 10^{-7} and $10^{-12} M_\odot$, and $\langle\sigma v\rangle = 10^{-26}$–$10^{-24}$ cm^3 s^{-1}. The region with higher probability density corresponds again to a Higgsino DM candidate with the annihilation cross section close to the canonical value $10^{-26}\,{\rm cm}^3\,{\rm s}^{-1}$, while the second region corresponds to a DM Wino candidate with much larger annihilation cross section $\sim 10^{-24}\,{\rm cm}^3\,{\rm s}^{-1}$. In the right panel we show the ratio of the luminosity over the reference one $\tilde{L} \equiv L/L_{ref}$, versus the DM mass, $m_{\chi^0_1}$.

We also analyzed the change in the boost by varying the γ-parameter in a range between 0.5 and 0.9, we only show the case $\gamma = 0.8$, and found that $\tilde{L}$ always got largely boosted by decreasing γ. This behavior depends on the normalization made on the protohalo mass, $M_{\rm ph}$, since it has been normalized to the limit of the numerical simulation ($10^4 M_\odot$). Figure 4.9 shows the boost factor, $\tilde{L} \equiv L/L_{ref}$, for points that reproduce all the experimental observables within 2σ confidence level. Right panel shows points which refer to a Higgsino-like and Wino-like neutralinos, while the left panel shows points where the neutralino is mostly Bino-like. Bino-like neutralinos have very small $\langle\sigma v\rangle$ in the limit of zero velocity. Co-annihilations, which play a very important role in the efficient annihilation in the early Universe, are not present anymore; this is the reason for which we have a very small boost of the luminosity.

Finally we comment that although not included in this work, Fermi and HESS bounds in the $m_{\chi^0_1}$–$\langle\sigma v\rangle$ plane strongly constrain the Wino-like region, excluding the region around 2.4 TeV (see Refs. [250, 251, 252, 253]).

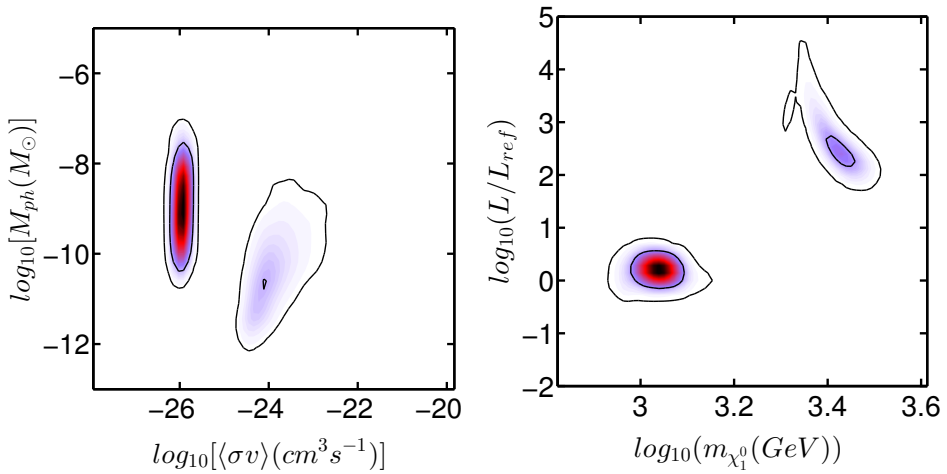

Figure 4.8: The two dimensonal joint posterior PDF for the protohalo mass, $M_{\rm ph}$, versus the velocity-averaged annihilation cross section times the relative velocity, $\langle\sigma v\rangle$ (left panel), and for $\tilde{L}$, obtained by using $\gamma = 0.8$, versus the dark matter particle mass, $m_{\chi_1^0}$ (right panel). For both panels, the region with higher probability density corresponds to a Higgsino DM candidate; in the second region the DM candidate is a Wino. Left panel shows that, in the Higgsino case, the protohalo mass $M_{\rm ph}$ is lower than the reference one, while $\langle\sigma v\rangle$ does not deviate from $\langle\sigma v\rangle_{\rm ref} \sim 10^{-26}$ cm^3 s^{-1}. Right panel shows that, in the Wino case, the protohalo mass $M_{\rm ph}$ is even lighter and $\langle\sigma v\rangle$ is two orders of magnitude larger than $\langle\sigma v\rangle_{\rm ref} \sim 10^{-26}$ cm^3 s^{-1}; thus, there is a substantial enhancement of $\tilde{L}$.

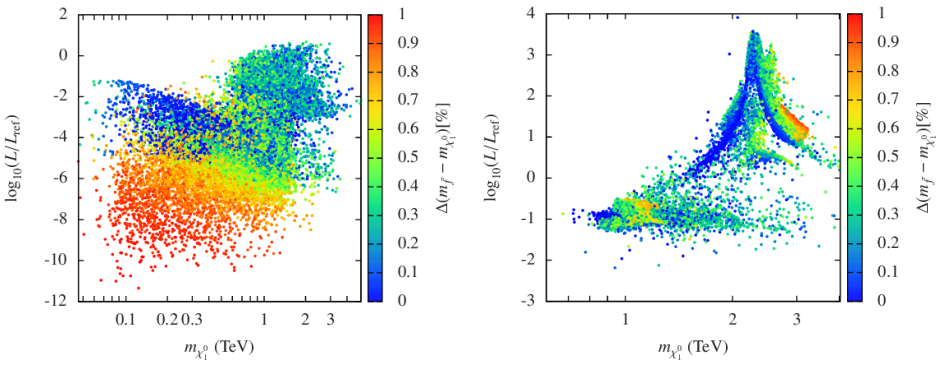

Figure 4.9: The mass of the lightest neutralino versus the boost factor, $\tilde{L} \equiv L/L_{ref}$, for points that reproduce all the experimental observables within 2σ confidence level. Left panel shows points which refer to a Bino-fraction (N_{11}) larger than 0.8. Right panel shows point with a Bino-fraction smaller than 0.8.

4.5.3 Collider

As commented in subsection 4.4.2, points with $m_{\chi_1^0}$ smaller than ~ 1 TeV are Bino-like and require a light enough next-to-lightest sparticle, in order to guarantee an efficient annihilation in the early Universe. Based on the characteristics of the next-to-lightest sparticle, we now comment some potential LHC signatures. For neutralinos lighter than 500 GeV there are two regions, in addition to Z/h/A resonances. The first one has $\chi_1^\pm$ close in mass to χ_1^0. A light Wino-like chargino which annihilates and co-annihilates in the early Universe is required, and is represented by points with 5 GeV $\lesssim m_{\chi_2^0} - m_{\chi_1^0} \lesssim$ 40 GeV in the left panel of Fig. 4.10. In this region χ_1^0 is dominantly Bino and $\chi_1^\pm$ and χ_2^0 are dominantly Winos. The Bino and Wino mass, M_1 and M_2, are close to the values where the tree level decay of χ_2^0 to $Z^{(*)}\chi_1^0$ is suppressed, and the branching ratio to $\gamma\,\chi_1^0$ acquires a large value, as discussed in detail in Refs. [254, 255]. Right panel of Fig. 4.10 shows that some of the points can have a dominant $\chi_2^0 \to \gamma\chi_1^0$ decay, giving a characteristic signature at a collider. Moreover, the decay channel $\tilde{l}_L \to l\chi_2^0 \to l\gamma\chi_1^0$ becomes relevant. Although the photon produced in the χ_2^0 and $\tilde{l}_L$ decays is very soft, it could give a clear signature at a collider in the boosted regime. It is important to keep in mind that a potential measurement of sleptons will directly constrain the prediction for the protohalo mass for the Bino-like neutralino. The second region corresponds to stau co-annihilation, where $\tilde{\tau}_1$ and χ_1^0 are very close in mass. In the left panel of Fig. 4.10, the points outside 5 GeV $\lesssim m_{\chi_2^0} - m_{\chi_1^0} \lesssim$ 40 GeV correspond to this region. Notice that, as a consequence of the universality conditions of slepton masses, the first and second generation of sleptons are relatively close in mass to the lightest stau and, therefore,

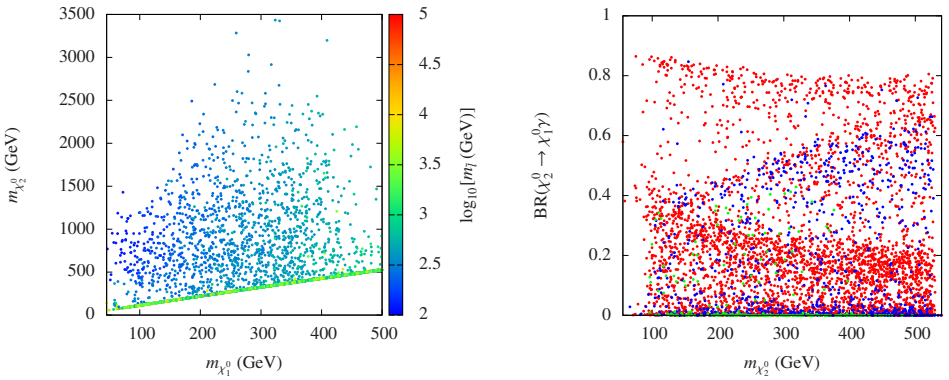

Figure 4.10: Left panel shows the χ_1^0 mass versus χ_2^0 mass plane. The colors show the mass of the lightest slepton ($\tilde{e}_{L,R}, \tilde{\mu}_{L,R}$). Right panel shows the branching ratio of χ_2^0 to photons as a function of the χ_2^0 mass for points with $m_{\tilde{l}_L} > m_{\chi_2^0}$. Red, blue and green points correspond to $m_{\tilde{l}_L} > 1\,\mathrm{TeV}$, $500\,\mathrm{GeV} < m_{\tilde{l}_L} < 1$ TeV and $m_{\tilde{l}_L} < 500\,\mathrm{GeV}$ respectively.

to the lightest neutralino. The authors of Ref. [256] discuss the status of this region after the first run of the LHC in the framework of the constrained MSSM, and project the likely sensitivity of the LHC searches in Run 2 at 14 TeV center of mass energy and 300 fb^{-1} of integrated luminosity, concluding that the entire CMSSM co-annihilation strip will be tested.

For $m_{\chi_1^0} \gtrsim 500$ GeV, new regions arise. Stop co-annihilations and neutralino annihilations are mediated by sfermions. In this neutralino mass range, the production of colored particles is the most promising. In Refs. [257, 258, 259], the stop co-annihilation region is studied, not only by direct stop production but also by gluino production, where direct stop productions constrain light stops ($m_{\tilde{t}_1} \lesssim 400$ GeV); for heavier stops, the production seems to be more promising. On the other hand, the region where neutralino annihilation is mediated by squarks is directly constrained by limits on squarks masses.

4.6 Summary

In this Chapter, based on [2], we have studied how the kinetic decoupling of dark matter could improve our knowledge of the properties of the dark matter protohalos within a well motivated supersymmetric extension of the Standard Model, the Minimal Supersymmetric Standard Model. Although it was at first introduced to solve the hierarchy problem of SM and space-time supersymmetry at large can be motivated by string theory, it revealed to have a very interesting characteristic when supplemented

with R-parity (invoked to ban undesirable interactions mediating for example proton decay): a dark matter candidate of the WIMP class, the lightest neutralino. If such a neutralino is the lightest supersymmetric particle (and the quantum number R-parity is preserved), it is stable, and could yield a thermal relic abundance as that indicated by the observed dark matter density.

In our analysis, we do a forecast on the mass of the protohalos within a framework realized with 9 independent parameters. The analysis is performed in the light of the latest data coming from particle physics experiments, as well as the relic density constraints: the most relevant observables involved in the analysis, in terms of their influence on the results, are the mass of the Higgs and the DM relic density. The most salient results are summarised in the following.

- The kinetic-decoupling temperature and, thus, the minimal protohalo mass result to be not well constrained for WIMPs, since the interactions involved in the annihilation of neutralinos, that are constrained by the relic density, are not necessarily those which participate in the scattering of neutralinos with first and second generation of fermions. In a supersymmetric framework, the minimal protohalo mass is typically $10^{-6} M_{\odot}$, assuming a Bino-neutralino annihilating through sfermions with a mass of around twice the neutralino mass. This resulted in a possible option to get a well tempered neutralino. In addition, this possibility has been well motivated by constrained scenarios like CMSSM, affirming that when the neutralino is mostly Bino, it efficiently annihilates through sfermions in the early Universe, giving the correct relic density. Nevertheless, it was in tension with the experimental data within the CMSSM, especially after the first run of the LHC, where a considerable part of this region was excluded.

- Using a Bayesian framework, we showed that the most probable neutralino mass regions satisfying both the Higgs mass and the relic density contraints, are those with the lightest supersymmetric neutralino mass around 1 TeV and 3 TeV, that correspond to Higgsino-like and Wino-like neutralino, respectively. We mentioned that, concerning the Higgsino-like neutralino, the annihilation cross section is driven by its Higgsino component, while for Wino-like neutralino, the annihilation cross section is mainly driven by its Wino component. We also discussed that the part of the region closer to ~ 2.4 TeV gets important contributions from the neutralino-stau co-annihilation, reducing both the effective annihilation rate of neutralinos in the early Universe and the value of the neutralino mass, in order to obtain the correct relic density.

- We commented that in the case of Wino-like or Higgsino-like neutralinos the annihilation products are gauge bosons, whose interactions involve different cou-

plings with respect to the ones of the neutralino-fermion scattering. For that reason kinetic decoupling temperature, T_{kd}, exhibits a considerable range of variation, that reflects, in turn, to a protohalo mass range of $M_{\rm ph} \sim 10^{-12}$–$10^{-7} M_\odot$.

- We also discussed the Bino like neutralino with masses smaller than ∼1 TeV, where a quasi-degenerated sfermion or chargino, or a light sfermion are necessary to get the correct dark matter abundance. Sleptons give the most important contribution for the kinetic decoupling temperature and therefore to the protohalo mass, setting the range $M_{\rm ph} \sim 10^{-11}$–$10^{-4} M_\odot$.

- Kinetic decoupling of dark matter, involving elastic scattering of a dark matter particle with Standard Model particles in the early Universe, reveals a relevant process for dark matter direct detection searches. In our analysis, we showed that the regions where the probability is higher the correlation between the protohalo mass and experimental signatures permits to put constraints on the protohalo mass. We depicted how improvements on the spin-independent sensitivity might reduce the most probable range of the protohalo mass between $\sim 10^{-9}\, M_\odot$ and $\sim 10^{-7}\, M_\odot$, while constraints associated to the expected spin-dependent sensitivity are weaker. To give this conclusion we computed scattering cross sections at tree-level. However, specially in the Wino-like neutralino case, loop corrections should be considered since the tree level coupling vanishes when approaching the pure Wino case.

- We discussed, as well, how the interplay among both spin-dependent and spin-independent scattering procesess, strongly depends on the neutralino composition. For both Higgsino-like and Wino-like cases, the spin-dependent scattering between Higgsino and fermions is mediated dominantly by the Z boson at tree level, while for the spin-independent scattering, the interaction is mediated by the Higgs boson. Regarding the Higgsino neutralino, we commented that the spin-independent interaction gives a nonzero tree-level contribution as long as gauginos are not decoupled, a non-negligible Bino or Wino component is necessary to have a non-negligible coupling with the Higgs. On the other hand, for the Wino-like neutralino the requirement of a non-negligible component of Higgsino is indispensable to have a tree-level contribution to both scattering processes if sfermions are decoupled.

- Depending on the nature of neutralino, the value of the annihilation cross section, $\langle \sigma v \rangle_{v \to 0}$, changes by different orders of magnitude. We presented that the annihilation cross section, $\langle \sigma v \rangle$, in the Higgsino case does not deviate from the canonical cross section, $\langle \sigma v \rangle \sim 10^{-26}$ cm^3 s^{-1}. On the other hand, in the Wino case non-relativistic effect is important, $\langle \sigma v \rangle$ increases up to two orders of

magnitude. And it is much smaller in the Bino-like case, where co-annihilations with sfermions played a crucial role to fix the correct abundance.

- Another way to look for dark matter is through indirect detection methods, which consist to detect, *indirectly*, the lightest supersymmetric particle through annihilation processes where Standard Model particles, including gamma-ray photons, are produced. Since the luminosity of each subhalo in the host halo due to the dark matter annihilation processes depends on the volume integral of the subhalo density squared, smaller and denser substructures provide an enhancement of the luminosity. In this work, we showed for both neutralino Higgsino-like and Wino-like cases how the boost of the luminosity due to dark matter annihilation increases, depending on the protohalo mass. We discussed that in the Higgsino case, there is no a significant enhancement of the luminosity: the protohalo mass is lower than the standard value often used in the literature of $\sim 10^{-6}\, M_{\odot}$, while $\langle \sigma v \rangle$ does not deviate from $\langle \sigma v \rangle \sim 10^{-26}$ cm^3 s^{-1}. In the Wino case, a substantial enhancement of the luminosity is seen: the protohalo mass reaches lighter values, and $\langle \sigma v \rangle$ is two orders of magnitude larger.

***

Summary

Our actual knowledge of the Universe is based on the theory of the initial "big explosion", the phenomenon known as the Big Bang. It explains the evolution of the Cosmos from a fraction of a second after its birth until today. According to the Big Bang theory the Universe was born circa 13,700 millions years ago, and at the beginning it occupied a tiny volume under the form of an extremely dense and hot plasma. From this point on, it has been expanding and freezing, in a process similar to that of the dough of the bread with the yeast. This process, along thousand of millions of years, gave room to the atoms, the stars and the galaxies that make up the current Universe. Such a model of cosmic evolution is based on General Relativity and on three empirical and robust facts: the observed recession of distant galaxies; the relative abundance of light chemical elements (hidrogen, helium and litium, created few minutes after the Big Bang); and the existence of a Cosmic Microwave Background radiation, the CMB. This CMB radiation was "emitted" in all directions of space 380,000 years after the big explosion, when the Universe had frozen-out enough for the electrons and photons to combine among themselves and to form the first neutral atoms. That is, since the electromagnetic radiation does not interact with neutral matter, from that point on, the photons freely propagated through space. This CMB radiation bath still continues to arrive to us and constitutes the most ancient light that we have managed to detect.

When this radiation was emitted, the conditions of the early Universe were impressed in the CMB under the form of tiny inhomogeneities of the order of 1 part in 10,000. Such small differences of density, derived from quantum fluctuations, would have been the seeds of the formation of the structures at large scale that we observe today in the sky, full of galaxies and voids. By measuring the CMB, we can obtain valuable information about the actual Universe. A detailed analysis of the CMB anisotropies permits to estimate the cosmological parameters as well as to discriminate among the different models of Universe. The model that better fits the current data is the Standard Model with a cosmological constant and cold dark matter. This model supposes,

as well, a flat Universe and an accelerated expansion caused by the cosmological constant, dubbed "dark energy" due to its unknown origin.
According to the CMB observations, the dark energy represents approximately 69% of the energy density of the Universe. Most of the remaining energy density is in the form of *cold dark matter*, a matter of unknown composition, non-relativistic and non-baryonic, i.e. not composed by protons, neutrons and electrons, that only constitute the 4% of ordinary matter that fills the Universe. Dark matter is a mysterious ingredient of the Universe, and it is the leading actor in this manuscript. It does not emit neither absorbs radiation, and it interacts weakly with ordinary matter. Nevertheless, we know about its existence by means of its gravitational effects: if there exists a large amount of dark matter, its gravitational effects would explain the rotation curves of galaxies. According to the standard cosmological model, the galaxies are mostly formed by huge concentrations of dark matter, usually dubbed as *halos*. In the middle of these enormous accumulations of dark matter – and only there – is present the observable part of galaxies.
Despite the numerous efforts spent to search dark matter, through different methods that span from direct and indirect detection to production at particle colliders, we do not have yet any definite information about its nature, and can only consider promising hypoteses. For example, we know that the dark matter has a velocity much smaller than the speed of light; otherwise the fluctuations of the density in the primordial Universe would not give rise to the galactic structures that we observe today. This implies that the particles composing the dark matter possess a rather large mass. On the other hand, we know that the dark matter particles have to be stable over cosmic time scales. The reason is simple: we do not know any plausible mechanism which is able to produce the dark matter; therefore, it has to be produced at the Big Bang. This stability is usually achieved in particle dark matter models through some quantum number or parity whose conservation forbids the decay of dark matter candidates.
A paradigmatic dark matter candidate which fulfills the above requirements is the WIMP, that is, a Weakly Interacting Massive Particle. It is a stable particle which has rather weak interactions with Standard Model particles, and yields the correct relic abundance to reproduce the observed dark matter density. As the other particles, the WIMPs were produced at the Big Bang. At very high energies, these particles were continuously created and destroyed. Their number then varied as a function of two effects, related to the expansion of the Universe: the first one is the *freeze-out* of the primordial plasma, that decreased both the density and the available energy controlling the annihilation and creation of WIMPs, that is stopping the processes of pair-annihilation and pair-creation of WIMPs. Nevertheless, this is not the end of WIMPs interactions. Indeed, after the freeze-out, WIMPs can still undergo elastic scattering processes with other particles of the primordial plasma. This second effect does not change the amount of WIMPs, but can still keep them in equilibrium with

the plasma: WIMPs are in kinetic equilibrium. When the rates of these processes drop below the expansion rate of the Universe, WIMPs finally decouple and we have *kinetic decoupling*. The idea of kinetic decoupling is relevant for considerations related to the formation of dark matter structures under the influence of gravity. Coming back to the nature of dark matter, recently there has been much speculation favouring mixed dark matter models, models where dark matter consists of an admixture of cold and non-cold particles, since they are a plausible solution to alleviate the small-scale crisis of the standard cosmology. The reason is the following: the particle associated to this second dark matter component has a larger free-streaming length, that causes a suppression of the matter power spectrum on the smallest scales, improving the compatibility with the observations of the local Universe, as for example the *Milky Way satellite problem* for which the simulated number of dark matter subhalos in a standard cosmology is much larger than the observed number of satellite galaxies that orbit close to the Milky Way.

In Chapter 3, we consider mixed dark matter models through the inclusion of a non-cold dark matter species. We vary both the mass and the fraction of the non-cold dark matter component in a wide range, in such a way we can explore more than a single particle physics model. Within this very large range, the possibility that our second component of dark matter could be either a sterile neutrino or an axion are included. Sterile neutrinos with keV masses may act as warm matter, and therefore their propagation may suppress the power spectrum at scales smaller than the characteristic free-streaming length. On the other hand, if axions were thermally-produced in the early Universe, they can contribute to the radiation density and then to the fraction of hot dark matter. Within a mixed dark matter framework, in the light of the most recent Planck data (CMB) and Baryonic Acoustic Oscillations (BAO) measurements, and adding as well the number of dwarf spheroidal satellite galaxies in the Milky Way, we have derived limits on the fraction of the non-cold dark matter component with respect to the total dark matter, as a function of its mass. We find that for small masses of this second species of dark matter, the limit on its fraction is approximately close to what one would expect from present constraints on the extra relativistic species. On the other hand, for values of the non-cold dark matter mass above fractions of keV, the CMB is unable to distinguish among the non-cold and the cold dark matter components, since the CMB physics is basically unaffected by the free-streaming nature of a particle with large mass. After including the matter power spectrum, that we include through the measurements of the BAO scale and the number of dwarf spheroidal satellite galaxies, yielding a suppression of the growth of matter perturbations induced by the non-zero velocity dispersions of the non-cold dark matter component, we obtain slightly tighter bounds on the fraction of warm dark matter (with respect to the total dark matter) with respect to those existing in the literature.

Then, in Chapter 4, we have studied how the kinetic decoupling of dark matter could improve our knowledge on the properties of the first gravitationally bound dark matter structures, often dubbed with the name of *protohalos*, within a well motivated supersymmetric extension of the Standard Model, the Minimal Supersymmetric Standard Model. Supersymmetry, initially introduced to solve problems within the Standard Model, proposed the existence of a new collection of particles, the lightest of which could constitute a dark matter candidate. In addition, the lightest supersymmetric particle, the lightest *neutralino*, belongs to the WIMP class. Within a chosen supersymmetric model, one with 9 independent parameters, we studied correlations among the temperature of the kinetic decoupling and direct detection signatures of dark matter, as the spin-dependent and the spin-independent cross-sections. Kinetic decoupling of dark matter, involving elastic scattering of a dark matter particle with Standard Model particles in the early Universe, reveals a relevant process for dark matter direct detection searches. We use electroweak precision measurements, some B-physics observables, the Higgs boson mass, and constraints on the WIMP-nucleon scattering cross-section by XENON-100. In addition, we include the measured relic density according to the *Planck* collaboration results, since we assumed a scenario with a single dark matter component which is thermally produced in the early Universe. We find that the most relevant observables involved in the analysis, in terms of their influence on the results, are the mass of the Higgs and the dark matter relic density. The kinetic decoupling and protohalos are addressed; within this supersymmetric context, we show how improvements on the spin-independent sensitivity might reduce the most probable range of the protohalo mass. Complementarily, we have done a study from the dark matter indirect detection point of view. Depending on the nature of the neutralino, the value of both the annihilation cross section and the mass of the protohalo change significantly. We show how the boost of the luminosity due to dark matter annihilation increases, depending on the protohalo mass, and thus on the type of neutralino. The understanding of the interactions that play a relevant role in the annihilation and scattering of neutralinos with Standard Model particles has helped us to identify correlations between protohalo masses and the supersymmetric spectrum. These correlations could be very helpful for constraining the kinetic decoupling temperature indirectly from current dark matter experiments. In particular, we have analyzed regions where neutralinos co-annihilate with other supersymmetric particles, that could be potentially tested by the largest operating collider, the Large Hadron Collider (LHC) at CERN.

Throught the joint analysis of particle physics and astrophysics aspects, we have studied how the implications of the dark matter nature could help us to unveal the puzzle of its existence.

Samenvatting

Onze kennis van het heelal is gebaseerd op de theorie van de eerste "grote explosie", het fenomeen dat bekend staat als de oerknal. Het verklaart de evolutie van de kosmos vanaf een fractie van een seconde na haar ontstaan tot aan vandaag. Volgens de oerknal-theorie ontstond het heelal ongeveer 13,7 miljard jaar geleden, en in het begin besloeg het slechts een heel klein volume in de vorm van een extreem dicht en heet plasma. Vanaf dit moment begon het uit te zetten en af te koelen, een proces dat je kan vergelijken met het rijzen van brooddeeg. Over een periode van miljarden jaren heeft dit proces ruimte gegeven aan atomen, sterren en sterrenstelsels waaruit het huidige heelal nu bestaat. Een dergelijk model van kosmische evolutie is gebaseerd op de algemene relativiteitstheorie en op drie empirische en robuuste feiten: de observatie dat ver van ons gelegen sterrenstelsels zich van ons verwijderen, de relatieve overvloed van lichte chemische elementen (waterstof, helium en lithium, die al een paar minuten na de oerknal zijn ontstaan), en het bestaan van de kosmische achtergrond straling (Cosmic Microwave Background, afgekort CMB). Deze kosmische achtergrond straling is ongeveer 380 duizend jaar na de oerknal in alle richtingen van het heelal uitgezonden. Het heelal was toen zodanig afgekoeld dat electronen en protonen samen de eerste neutrale atomen konden vormen. Omdat electromagnetische straling geen interacties aangaat met neutrale materie, konden fotonen vanaf dat moment vrij door de ruimte propageren. Het licht van dit CMB stralingsbad bereikt ons nog altijd en is het oudste licht dat we kunnen observeren. Toen deze straling werd uitgezonden is de toestand van het vroege heelal ingeprent in de CMB, in de vorm van minuscule inhomogeniteiten. Zulke kleine verschillen in de dichtheid, voortgekomen uit quantumfluctuaties, zouden de zaadjes zijn geweest van de structuurformatie op grote schaal die we vandaag de dag aan de hemel observeren, vol met sterrenstelsels en de zich daartussen bevindende leegtes. Een gedetailleerde analyse van de CMB anisotropieën staat ons toe de kosmologische parameters te schatten en onderscheid te kunnen maken tussen de verschillende modellen van het heelal. Het model dat het best aansluit bij de huidige data is het standaard model van de kosmologie, met een kosmologische con-

stante en koude donkere materie. Dit model veronderstelt een vlak heelal en versnelde uitdijing veroorzaakt door de kosmologische constante, ook wel donkere energie genoemd. Uit de observaties van de CMB volgt dat donkere energie verantwoordelijk is voor ongeveer 69 procent van de energiedichtheid van het heelal. Het grootste gedeelte van de overige energiedichtheid wordt bepaald door koude donkere materie, een vorm van materie van onbekende samenstelling, dat niet-relativistisch en niet-baryonish is. Dit laatste wil zeggen dat het niet is opgebouwd uit protonen en neutronen etc., deeltjes die vallen onder de gewone materie, dat maar 4 procent van ons heelal vult. Donkere materie is een mysterieus ingrediënt van het heelal, en het speelt de hoofdrol in dit proefschrift. Het zendt geen straling uit en absorbeert het ook niet, en het gaat zeer zwak interacties aan met normale materie. Toch weten we van het bestaan ervan af door effecten veroorzaakt door de zwaartekracht: als er een grote hoeveelheid donkere materie bestaat, zouden de zwaartekrachtseffecten die erdoor veroorzaakt worden de rotatiecurve van sterrenstelsels kunnen verklaren. Volgens het standaard kosmologische model bestaan de sterrenstelsels voornamelijk uit gigantische concentraties donkere materie, ook wel donkere materie halos genoemd. Alleen in het midden van deze enorme samenklontering van donkere materie bevindt zich het door ons zichtbare gedeelte van het sterrenstelsel. Ondanks de talrijke pogingen om donkere materie te ontdekken, variërend van directe detectie en indirecte detectie tot productie in deeltjesversneller, hebben we nog steeds geen definitieve informatie over haar aard, en kunnen we alleen veelbelovende hypotheses overwegen. We weten bijvoorbeeld dat de snelheid van de donkere materiedeeltjes veel kleiner is dan de lichtsnelheid, anders zouden de dichtheid-fluctuaties in het zeer vroege heelal niet hebben geleid tot de galactische structuren die we vandaag de dag observeren. Dit impliceert dat de deeltjes waaruit donkere materie bestaat een relatief grote massa moeten hebben. We weten ook dat de donkere materiedeeltjes stabiel moeten zijn gedurende kosmische tijdschalen. De reden is simpel: we kennen geen aannemelijk mechanisme dat in staat is donkere materie te produceren, daarom moet het zijn ontstaan tijdens de oerknal. Deze stabiliteit wordt in donkere materie-modellen gewoonlijk bereikt door een bepaald quantum nummer of pariteit waarvan de conservatie het verval van de donkere materie-kandidaat verbiedt. Een donkere materie-kandidaat die aan al deze bovenstaande eisen voldoet is de WIMP, de "Weakly Interacting Massive Particle". Het is een stabiel deeltje dat tamelijk zwak interacties aan gaat met deeltjes uit het standaard model, en levert het juiste overschot aan donkere materie uit het vroege heelal op om de geobserveerde donkere materie-dichtheid te reproduceren. Net zoals de andere deeltjes zijn de WIMPs ontstaan tijdens de oerknal. Deze deeltjes werden continu met zeer hoge energieën gecreëerd en weer vernietigd. Hun aantal varieerde op dat moment als een functie van twee effecten gerelateerd aan de uitzetting van het heelal: het eerste effect is de "freeze-out", het heel erg sterk afkoelen van het oerplasma, wat zowel zorgde voor een afname van de dichtheid als de beschikbare energie voor het in paren creëren van WIMPs, waardoor dit proces stopte. Dit is des-

ondanks niet het einde van WIMP-interacties. Na deze "freeze-out" konden WIMPs nog steeds elastische verstrooiing ondergaan met andere deeltjes in het oerplasma. Het tweede effect heeft geen invloed op de hoeveelheid WIMPs, maar zorgt ervoor dat deze deeltjes nog steeds in evenwicht zijn met het plasma: de WIMPs zijn in kinetisch evenwicht. Wanneer de mate van deze verstrooiing-processen lager wordt dan de mate van de uitdijing van het heelal, ontkoppelen de WIMPs en spreken we van kinetische ontkoppeling. Het idee van kinetische ontkoppeling speelt een rol bij overwegingen gerelateerd aan de formatie van donkere materie-structuren onder de invloed van zwaartekracht. Om terug te komen op de aard van donkere materie: recentelijk is er veel gespeculeerd in het voordeel van gemengde donkere materie-modellen, modellen waar donkere materie uit een mengsel van koude en niet-koude deeltjes bestaat. Dit zou namelijk een aannemelijke oplossing zijn om het probleem dat de standaard kosmologie op kleine schaal heeft, te verlichten. De reden hiervoor is dat het laatstgenoemde deeltje een grotere afstand kan afleggen in het vroege heelal, de zogenaamde "vrije-propagatie lengte". Dit onderdrukt de "materie power spectrum" op de kleinste schaal en verbetert hierdoor de verenigbaarheid met de observaties van het lokale heelal. Zoals bijvoorbeeld het probleem met de satelliet-sterrenstelsels van onze Melkweg, waarvoor het aantal subhalos berekend doormiddel van simulaties veel groter is dan het aantal satelliet-sterrenstelsels dat dicht om onze Melkweg draait. In hoofdstuk 3 overwegen we gemengde donkere materie-modellen, met zowel koude als niet-koude donkere materie soorten. We variëren zowel de massa en de fractie van de niet-koude component van de donkere materie over een grote schaal, op een dusdanige manier dat we meerdere deeltjes modellen kunnen verkennen. Op deze zeer grote schaal is ook meegenomen dat de tweede donkere materie-component een steriele neutrino of een axion zou kunnen zijn. Steriele neutrinos met massa's rond de keV kunnen zich gedragen als warme materie, waardoor hun voortbeweging het power spectrum zou kunnen onderdrukken op schalen kleiner dan de karakteristieke vrij-propagatie lengte van het deeltje. Anderzijds, als axionen in het vroege heelal in thermisch evenwicht zijn geproduceerd, kunnen ze bijdragen aan de stralingsdichtheid en de fractie hete donkere materie. Binnen een gemengd donkere materie-kader, in het licht van de meest recente Planck data (CMB) en Baryonische Akoestische Oscillaties (BAO) metingen, waarin we ook het aantal bolvormige dwerg satelliet-sterrenstelsels in de Melkweg hebben meegenomen, hebben we limieten afgeleid op de fractie van de niet-koude donkere materie component ten opzichte van de totale donkere materie, als functie van haar massa. We vinden dat voor donkere materie van deze tweede soort met kleine massa's, de limiet op de fractie van deze soort in het totaal ongeveer gelijk is aan wat we verwachten aan de hand van huidige afbakeningen van de extra relativistische soorten. Aan de andere kant is de CMB niet in staat onderscheid te maken tussen de niet-koude en koude donkere materie-componenten voor massa's in de orde van grote van een keV en hoger, omdat de natuurkunde van de CMB in feite onaangetast blijft door de vrije propagatie van een zwaar deeltje. Gebruikmakend van de metingen van

de BAO-schaal en het aantal bolvormige dwerg satelliet-sterrenstelsels hebben we het "materie power spectrum" toegevoegd, wat resulteert in een onderdrukking van de groei van dichtheid verstoringen geïnduceerd door de snelheidsspreiding van de niet-koude donkere materie-component. Hierna verkregen we iets strakkere begrenzingen op de fractie warme donkere materie (ten opzichte van de totale donkere materie) ten opzichte van de begrenzingen in de literatuur. Dan, in hoofdstuk 4, bestuderen we hoe de kinetische ontkoppeling van donkere materie onze kennis over de eigenschappen van de eerste zwaartekrachtsgebonden donkere materie-structuren kan verbeteren, vaak protohalos genoemd, binnen een goed onderbouwde supersymmetrische extensie van het Standaard Model, de Minimal Supersymmetric Standard Model. Supersymmetrie, aanvankelijk geïntroduceerd om problemen binnen het Standaard Model op te lossen, stelt het bestaan van een nieuwe collectie deeltjes voor, waarvan de lichtste deeltjes een donkere materie-kandidaat zouden kunnen zijn. Daarnaast behoort het lichtste supersymmetrische deeltje, de lichtste neutralino, tot de WIMP-klasse. Binnen een gekozen supersymmetrisch model, met 9 onafhankelijke parameters, hebben we de correlaties bestudeerd tussen de temperatuur van de kinetische ontkoppeling van donkere materie, en de signalen afkomstig van directe detectie van donkere materie in de vorm van spin-afhankelijke en spin-onafhankelijke werkzame doorsnedes. Kinetische ontkoppeling van donkere materie, waar de elastische verstrooiing van donkere materiedeeltjes met deeltjes uit het Standaard Model in het vroege heelal bij betrokken is, onthult een relevant proces voor het direct detecteren van donkere materie. We gebruiken precisiemetingen aan de elektrozwakke wisselwerking, een aantal waarnemingsgrootheden uit de B-fysica, de massa van het Higgs-deeltje, en de afbakening van de werkzame doorsnede van WIMP-nucleon verstrooiing bepaald door XENON-100. Daarnaast nemen we de gemeten "relic" dichtheid uit de resultaten van de Planck collaboratie mee, gezien we een scenario aannemen met een enkele donkere materie-component die in het vroege heelal in thermisch evenwicht is geproduceerd. We vinden dat de massa van het Higgs-deeltje en de relic dichtheid van de donkere materie de meest relevante waarnemingsgrootheden zijn die bij de analyse betrokken zijn, gezien hun invloed op de resultaten. De kinetische ontkoppeling en protohalos komen aan bod; binnen deze supersymmetrische context laten we zien hoe verbeteringen aan de spin-onafhankelijke gevoeligheid mogelijk het meest waarschijnlijke gebied van de protohalo-massa kan verkleinen. Complementair hieraan hebben we ook een studie gedaan vanuit de invalshoek van de indirecte detectie van donkere materie. Afhankelijk van de aard van het neutralino verandert zowel de waarde van de annihilatie-werkzame doorsnede als de massa van de protohalo significant. We laten zien dat de oppepper van de helderheid veroorzaakt door de annihilatie van donkere materie toeneemt, afhankelijk van de massa van de protohalo, en dus van het type neutralino. Het begrip van de interacties die een relevante rol spelen bij de annihilatie en verstrooiing van neutralinos met deeltjes uit het Standaard Model heeft ons geholpen om correlaties te identificeren tussen de massa van protohalos en het

supersymmetrische spectrum. Deze correlaties kunnen behulpzaam zijn bij het indirect afbakenen van de temperatuur van de kinetische ontkoppeling doormiddel van huidige donkere materie-experimenten. In het bijzonder hebben we regionen geanalyseerd waar neutralinos co-annihileren met andere supersymmetrische deeltjes. Dit kan mogelijk getest worden met de grootste opererende deeltjesversneller, the Large Hadron Collider (LHC) in CERN.

Door de gezamenlijke analyse van aspecten uit de deeltjesfysica en de astrofysica hebben we bestudeerd hoe implicaties van de aard van donkere materie kunnen helpen om de puzzel van haar bestaan te ontrafelen.

Vertaald door Niki Klop en Richard Bartels.

A Appendix: Jeans Theory

A.1 Jeans Theory

In an attempt to understand the formation of stars and planets, Jeans (1902) demonstrated the existence of an important instability in evolving clouds of gas. This instability, known as the *gravitational Jeans instability*, is now the cornerstone of the standard model for the origin of galaxies and large-scale structures. Jeans demonstrated that, starting from a homogeneous and isotropic fluid, small fluctuations in the density, $\delta\rho$, and velocity, δv, could evolve with time. In particular, he showed that density fluctuations can grow in time if the stabilising effect of pressure is much smaller than the tendency of the self-gravity of a density fluctuation to induce collapse.

Gravity is an attractive force so, as long as pressure forces are negligible, an overdense region is expected to accrete material from its surroundings, thus becoming even denser. The denser it becomes, the more it will accrete, resulting in an instability which can ultimately cause the collapse of a fluctuation into a gravitationally bound object. The simple criterion needed to decide whether a fluctuation will grow with time is that the typical lengthscale of a fluctuation should be larger than the *Jeans length*, λ_J, for the fluid.

Let us work out the details of the previous summary. The Newtonian motion of a perfect fluid is described by the following set of equations:

$$\frac{\partial \rho}{\partial t} + \vec{\nabla} \cdot (\rho \, \vec{v}) = 0 \quad \text{(Continuity)}, \tag{A.1}$$

$$\frac{\partial \vec{v}}{\partial t} + (\vec{v} \cdot \vec{\nabla}) \, \vec{v} + \frac{1}{\rho} \, \vec{\nabla} \, p + \vec{\nabla} \Psi = 0 \quad \text{(Euler)}, \tag{A.2}$$

$$\vec{\nabla}^2 \Psi - 4\pi G \, \rho = 0 \quad \text{(Poisson)}, \tag{A.3}$$

$$\frac{\partial s}{\partial t} + \vec{v} \cdot \vec{\nabla} s = 0 \quad \text{(Conservation of Entropy)}, \tag{A.4}$$

where ρ is the matter density, p the pressure, $\vec{v}$ the local fluid velocity, s the entropy density and Ψ the gravitational potential. We can consider a static solution with matter at rest and uniformly distributed:

$$\rho = \rho_0 \, , \tag{A.5}$$

$$\vec{v} = \vec{0} \, , \tag{A.6}$$

$$p = p_0 \, , \tag{A.7}$$

$$\vec{\nabla} \Psi = \vec{0} \, , \tag{A.8}$$

$$s = s_0 \, . \tag{A.9}$$

Notice, however, that assuming a vanishing gravitational force, $\vec{\nabla} \Psi = \vec{0}$ contradicts Poisson's equation[1]; as Jeans did, "the Jeans swindle", we will proceed anyway. This problem will disappear when we analyse the case of an expanding Universe. Our next step is to consider perturbations of the static case,

$$\rho = \rho_0 + \delta \rho \, , \tag{A.10}$$

$$\vec{v} = \delta \vec{v} \, , \tag{A.11}$$

$$p = p_0 + \delta p \, , \tag{A.12}$$

$$\Psi = \Psi_0 + \delta \Psi \, , \tag{A.13}$$

$$s = s_0 + \delta s \, . \tag{A.14}$$

Substitution of eqs.(A.10)-(A.14) in (A.1)-(A.4) gives a set of equations that is non-linear: we linearize neglecting the terms beyond the first order in the perturbations, to obtain:

[1] This ultimately means that there is no homogeneous static configuration for a self gravitating perfect fluid in a static Newtonian Universe.

$$\frac{\partial \delta\rho}{\partial t} + \rho_0 \vec{\nabla} \cdot \delta\vec{v} = 0\,, \tag{A.15}$$

$$\frac{\partial \delta\vec{v}}{\partial t} + \frac{1}{\rho_0}\left(\frac{\partial p}{\partial \rho}\right)_s \vec{\nabla}\,\delta\rho + \left(\frac{\partial p}{\partial s}\right)_\rho \vec{\nabla}\delta s + \vec{\nabla}\,\delta\Psi = 0 \tag{A.16}$$

$$\vec{\nabla}^2\delta\Psi - 4\pi G\,\delta\rho = 0\,, \tag{A.17}$$

$$\frac{\partial \delta s}{\partial t} = 0\,. \tag{A.18}$$

In Eq. (A.17), $\left(\frac{\partial p}{\partial \rho}\right)_s \equiv c_s^2$, with c_s^2 the speed of sound.
We now look for solutions in the form of plane waves

$$\delta u_i = \delta_{0,i}\,\exp(i\omega t)\,\exp(i\vec{k}\cdot\vec{r})\,, \tag{A.19}$$

where δu_i, $i = 1$ to 4 stands for $\delta\rho$, $\delta\vec{v}$, $\delta\Psi$ and δs, respectively. $\vec{r}$ is the position vector, $\vec{k}$ is a wave vector, and ω an angular frequency; we also introduce $\delta_0 = \delta\rho/\rho_0$.

We can now substitute (A.19) into equations (A.15)-(A.18) to obtain:

$$\omega\,\delta_0 + \vec{k}\cdot\delta\vec{v} = 0\,, \tag{A.20}$$

$$\omega\,\delta\vec{v} + \vec{k}\,c_s^2\,\delta_0 + \frac{\vec{k}}{\rho_0}\left(\frac{\partial p}{\partial s}\right)_\rho \delta s + \vec{k}\,\delta\Psi = 0 \tag{A.21}$$

$$k^2\,\delta\Psi + 4\pi G\,\delta_0\,\rho_0 = 0\,, \tag{A.22}$$

$$\omega\,\delta s = 0\,. \tag{A.23}$$

First we consider the solutions that do not depend on time, i.e. those with $\omega = 0$.

- With $\delta s =$ constant $\neq 0$, that is, the perturbation in s is conserved, such a solution is called *isoentropic solution*.
- Additional solutions with $\omega = 0$ are obtained with $\delta s = 0$ and $\vec{k}\cdot\delta\vec{v} = 0$. They have $\vec{k}$ perpendicular to $\delta\vec{v}$, and do not imply a perturbation of the density: they just correspond to vortex motions.

Time dependent solutions are much more interesting. They have $\delta s = 0$ and are thus called *adiabatic*. From equation (A.20), $\vec{k}\cdot\delta\vec{v} \neq 0$; since we can separate $\vec{k}$ in components parallel and perpendicular to $\delta\vec{v}$, and the latter has already appeared in the time independent case, we now assume that $\vec{k}$ is parallel to $\delta\vec{v}$, i.e. longitudinal. Thus, equations (A.20)-(A.23) become ($|\delta\vec{v}| = \delta v$ and $|\vec{k}| = k$):

$$\omega\,\delta_0 + k\,\delta v = 0\,, \tag{A.24}$$
$$\omega\,\delta v + k\,c_s^2\,\delta_0 + k\,\delta\Psi = 0\,, \tag{A.25}$$
$$k^2\,\delta\Psi + 4\pi G\,\delta_0\,\rho_0 = 0\,. \tag{A.26}$$

The system admits a non-vanishing solution if and only if the following condition, a *dispersion relation*, is satisfied:

$$\omega^2 - c_s^2\,k^2 + 4\pi G\,\rho_0 = 0\,. \tag{A.27}$$

We will then have two types of solutions, depending on the wavelength $\lambda = 2\pi/k$, being larger or smaller than

$$\lambda_J = c_s \left(\frac{\pi}{G\,\rho_0}\right)^{1/2}\,, \tag{A.28}$$

called the *Jeans length*.

- $\lambda < \lambda_J$: in this case the pulsation ω in equation (A.27) is real:

$$\omega = \pm c_s^2\,k \left[1 - \left(\frac{\lambda}{\lambda_J}\right)^2\right]^{1/2}\,. \tag{A.29}$$

  Therefore, the density perturbation evolves according to:

$$\delta\rho = \rho_0\,\delta_0\,\exp[i(\vec{k}\cdot\vec{r} \pm |\omega| t)]\,, \tag{A.30}$$

  which represents two progressive sound waves propagating in the directions $\pm\vec{k}$, with a phase velocity:

$$v_{ph} = c_s \left[1 - \left(\frac{\lambda}{\lambda_J}\right)^2\right]^{1/2}\,. \tag{A.31}$$

  Such a velocity goes to zero when $\lambda \to \lambda_J$.

- $\lambda > \lambda_J$: in this case ω is imaginary:

$$\omega = \pm(4\pi G\,\rho_0)^{1/2} \left[1 - \left(\frac{\lambda}{\lambda_J}\right)^2\right]^{1/2}\,. \tag{A.32}$$

Now, the density perturbation reads:

$$\delta\rho = \rho_0\,\delta_0\,\exp(i\vec{k}\cdot\vec{r})\,\exp(\pm|\omega|t)\,, \tag{A.33}$$

which describes stationary waves whose amplitudes increase or decrease exponentially with time. The characteristic timescale for the evolution of the amplitude is:

$$\tau = |\omega|^{-1} = (4\pi G\,\rho_0)^{-1/2}\left[1-\left(\frac{\lambda_J}{\lambda}\right)^2\right]^{-1/2}\,. \tag{A.34}$$

Only this previous solution identifies the phenomenon of gravitational instability. For scales $\lambda \gg \lambda_J$, τ coincides with the free fall time, $\tau_{ff} \simeq (4\pi G\,\rho_0)^{-1/2}$, but for $\lambda \to \lambda_J$ the characteristic time diverges, $\tau \to \infty$.

A.1.1 Instabilities in an expanding Universe

We have analysed the evolution of perturbations of a static homogeneous fluid: let us now consider the evolution of perturbations associated to an expanding Universe. To do so we now consider an expanding background solution to eqs.(A.1)-(A.4),

$$\rho(t) = \rho(t_0)\,a^{-3}(t)\,,\ \vec{v} = \frac{\dot{a}}{a}\vec{r},\ \vec{\nabla}\Psi = \frac{4\pi G}{3}\rho\,\vec{r}\,, \tag{A.35}$$

where $a(t)$ is the expansion factor. The linearized equations describing the evolution of adiabatic perturbations become

$$\frac{\partial\delta\rho}{\partial t} + 3\frac{\dot{a}}{a}\,\delta\rho + \frac{\dot{a}}{a}(\vec{r}\cdot\vec{\nabla})\delta\rho + \rho_0\,\vec{\nabla}\cdot\,\delta\vec{v} = 0\,, \tag{A.36}$$

$$\frac{\partial\delta\vec{v}}{\partial t} + \frac{\dot{a}}{a}\delta\vec{v} + \frac{\dot{a}}{a}(\vec{r}\cdot\vec{\nabla})\delta\vec{v} + \frac{c_s^2}{\rho_0}\vec{\nabla}\,\delta\rho + \vec{\nabla}\,\delta\Psi = 0 \tag{A.37}$$

$$\vec{\nabla}^2\delta\Psi - 4\pi G\,\delta\rho = 0\,. \tag{A.38}$$

Notice that "the Jeans swindle" is not necessary anymore[2]. Defining again δ_0 and decomposing the perturbations in Fourier modes according to

$$f(\vec{r},t) \propto \int d^3r\, f_{\vec{k}}(t)\,\exp\left(i\vec{k}\cdot\vec{r}\right)\,, \tag{A.39}$$

[2]Notice in addition that for $|\vec{r}| > \left(\frac{\dot{a}}{a}\right)^{-1}$, $|\vec{v}| > 1$, a relativistic treatment would then be necessary; furthermore the background potential Ψ diverges with $|\vec{r}| \to \infty$.

for $f = \delta_0$, $\delta\vec{v}$ and $\delta\Psi$, equations (A.36)-(A.38) lead to

$$\ddot{\delta}_{0\vec{k}} + 2\frac{\dot{a}}{a}\,\delta_{0\vec{k}} + \left(c_s^2\,k^2 - 4\pi G\rho\right)\delta_{0\vec{k}} = 0\,. \tag{A.40}$$

In eq.(A.40) one can read the same kind of qualitative behaviour that was found in the non-expanding case in terms of the Jeans wavenumber $k_J^2 = \frac{4\pi G}{c_s^2}\rho$, which separates gravitationally stable and unstable modes: short wavelength modes ($k \gg k_J$) where the perturbations oscillate as a sound wave, and long wavelength modes ($k \ll k_J$) where the perturbation may grow. Detailed solutions depend on the expansion factor $a(t)$. Let us illustrate how things work considering a spatially flat, matter dominated FRW model where $\rho = 1/(6\pi G\,t^2)$, $a = a_0(t/t_0)^{2/3}$, and $\dot{a}/a = 2/3t$. Then, for $k \ll k_J$,

$$\ddot{\delta}_{0\vec{k}} + \frac{4}{3}\frac{\dot{\delta}_{0\vec{k}}}{t} - \frac{2}{3t^2}\delta_{0\vec{k}} = 0\,. \tag{A.41}$$

We thus find

- a growing solution
$$\delta_+ \propto t^{2/3} (\propto a)\,; \tag{A.42}$$

- a decaying solution
$$\delta_- \propto t^{-1} (\propto a^{-2/3})\,. \tag{A.43}$$

The solutions above are quite different from the static case: instead of exponential growth or decay, the effect of expansion, resulting in a power law behaviour, slows the evolution of perturbations.

In order to extend the analysis for a radiation dominated Universe, since we have not started with a fully relativistic treatment, one can modify the evolution equations to incorporate the effect of radiation pressure. Skipping details (for which we refer the reader to [260]), the set of equations describing the fluid becomes

$$\frac{\partial\rho}{\partial t} + \vec{\nabla}\cdot\left(\rho + \frac{p}{c^2}\right)\vec{v} = 0\,, \tag{A.44}$$

$$\left(\rho + \frac{p}{c^2}\right)\left(\frac{\partial\vec{v}}{\partial t} + \vec{v}\cdot\vec{\nabla}\vec{v}\right) + \vec{\nabla}p + \left(\rho + \frac{p}{c^2}\right)\vec{\nabla}\Psi = 0 \tag{A.45}$$

$$\vec{\nabla}^2\Psi - 4\pi G\left(\rho + 3\frac{p}{c^2}\right) = 0\,. \tag{A.46}$$

The resulting equation for the evolution of the Fourier mode $\delta_{0\vec{k}}$ of the density perturbation is then

$$\ddot{\delta}_{0\vec{k}} + 2\frac{\dot{a}}{a}\dot{\delta}_{0\vec{k}} + \left(c_s^2 k^2 - \frac{32}{3}\pi G\,\rho\right)\delta_{0\vec{k}} = 0\,, \tag{A.47}$$

in which the speed of sound is $c_s = c/\sqrt{3}$. For a flat, radiation dominated, FRW model: $\rho = 3/(32\pi G t^2)$, $a = a_0(t/t_0)^{1/2}$, and $\dot{a}/a = 1/2t$ and thus

$$\ddot{\delta}_{0\vec{k}} + \frac{1}{t}\dot{\delta}_{0\vec{k}} - \frac{1}{t^2}\left(1 - \frac{3c_s^2 k^2}{32\pi G\,\rho}\right)\delta_{0\vec{k}} = 0\,, \tag{A.48}$$

Then, for $k \ll k_J$, there will be two solutions:

- a growing one

$$\delta_+(t) \propto t \propto a^2\,; \tag{A.49}$$

- a decaying one

$$\delta_-(t) \propto t^{-1} \propto a^{-2/3}\,. \tag{A.50}$$

***

B Appendix: The Boltzmann Equations

In this appendix, we briefly present aspects of the Boltzmann equations for photons, neutrinos and cold dark matter, following [261]. The evolution of the phase space distribution function f of a particle species is governed by the Boltzmann equation. The unintegrated form of the Boltzmann equation for a given species relates the time evolution in space-time of its distribution function f to possible collisional terms; and it is given by:

$$\frac{df}{dt} = C[f]\,, \tag{B.1}$$

where C denotes the collision terms. In the absence of collisions, the distribution function follows the law $df/dt = 0$, which means that the number of particles in a given element of phase space does not change with time. When different species interact, the Boltzmann equations which govern the evolution of the different phase space distributions are coupled. The full time derivative in Eq.(B.1) can be written as

$$\frac{df}{dt} = \frac{\partial f}{\partial t} + \frac{\partial f}{\partial x^i}\frac{dx^i}{dt} + \frac{\partial f}{\partial E}\frac{dE}{dt} + \frac{\partial f}{\partial \hat{p}^i}\frac{d\hat{p}^i}{dt}\,, \tag{B.2}$$

that is, the distribution function of these particles depends on the space-time coordinates, x^μ, on the energy E ($E = \sqrt{m^2 + p^2}$, with m the mass of the particle) and on the direction of the momentum vector, $\hat{p}$. Even in the absence of interactions, the evolution might not be simple, since the equations that govern the evolution of the potentials and the overdensities are connected with the Boltzmann equations for photons, neutrinos, ordinary and cold dark matter. The smooth, expanding, FRW Universe is described by a single function: the scale factor $a(t)$. On the other hand, in

order to describe the perturbed, not-that-smooth Universe, it is necessary to introduce two further functions which depend on both space and time: Ψ and Φ. The former corresponds to the pertubations to the metric (the Newtonian potential), while the latter corresponds to the perturbations to the spatial curvature. Without entering into details (we refer the interested reader to [261]), one can rewrite dx^i/dt and dE/dt as

$$\frac{dx^i}{dt} = \frac{\hat{p}^i}{a}\frac{p}{\sqrt{m^2+p^2}} = \frac{\hat{p}^i}{a}\frac{p}{E} \tag{B.3}$$

$$\frac{dE}{dt} = \frac{p}{E}\frac{dp}{dt} = \frac{p^2}{E}\left[-H - \frac{d\Phi}{dt} - \frac{\hat{p}^i}{a}\frac{d\Psi}{dx^i}\right] . \tag{B.4}$$

In order to obtain the Boltzmann equation for photons and neutrinos we set $E = p$ [1]. Using (B.3) and (B.4), the expression (B.2) reads

$$\frac{df}{dt} = \frac{\partial f}{\partial t} + \frac{\hat{p}^i}{a}\frac{\partial f}{\partial x^i} - p\frac{\partial f}{\partial p}\left[H + \frac{d\Phi}{dt} - \frac{\hat{p}^i}{a}\frac{d\Psi}{dx^i}\right] . \tag{B.5}$$

Notice that the last term in Eq. (B.2) has been neglected. The reason for that is the following. Following a perturbative analysis, the 0^{th}-order, unperturbed distribution function, is the usual Bose-Einstein or Fermi-Dirac function:

$$f_0(E) = \frac{g_s}{h^3}\frac{1}{e^{E/k_B T_0} \pm 1} , \tag{B.6}$$

where the sign + is for fermions and the sign − is for bosons. $T_0 = aT$ is the present temperature, the factor g_s is the number of spin degrees of freedom, and k_B and h^3 are the Boltzmann and the Planck constants, respectively. Equation (B.6) does not depend on the momentum vector $\hat{p}^i$ and thus $\partial f/\partial \hat{p}^i$ is a first order term. In addition, since the term $\frac{d\hat{p}^i}{dt}$ changes only in presence of the potential, it is also a first order term and, therefore, the last term in Eq. (B.2) being the product of two first order terms, it can be neglected at first order.

In the case of cold dark matter we plug Eqs. (B.3) and (B.4) in Eq. (B.2); the total derivative of the distribution function reads

$$\frac{df}{dt} = \frac{\partial f}{\partial t} + \frac{\hat{p}^i}{a}\frac{p}{E}\frac{\partial f}{\partial x^i} - \frac{\partial f}{\partial p}\left[\frac{p^2}{E}H + \frac{d\Phi}{dt}\frac{p^2}{E} - \frac{\hat{p}^i}{a}\frac{p^2}{E}\frac{d\Psi}{dx^i}\right] . \tag{B.7}$$

Since cold dark matter does not have interactions, $C[f] = 0$. The Boltzmann equation for cold dark matter is then

$$\frac{\partial f}{\partial t} + \frac{\hat{p}^i}{a}\frac{p}{E}\frac{\partial f}{\partial x^i} - \frac{\partial f}{\partial p}\left[\frac{p^2}{E}H + \frac{d\Phi}{dt}\frac{p^2}{E} - \frac{\hat{p}^i}{a}\frac{p^2}{E}\frac{d\Psi}{dx^i}\right] = 0 . \tag{B.8}$$

[1] That is neutrinos are considered massless particles, see [261].

Integrating (B.8) over the phase space volume, we obtain:

$$\frac{\partial}{dt}\int\frac{d^3p}{(2\pi)^2}\,f+\frac{1}{a}\frac{\partial}{\partial x^i}\int\frac{d^3p}{(2\pi)^2}\,f\,\frac{p\hat{p}^i}{E}+ \\ -\left[H+\frac{d\Phi}{dt}\right]\int\frac{d^3p}{(2\pi)^2}\frac{\partial f}{\partial E}\frac{p^2}{E}-\frac{1}{a}\frac{d\partial\Psi}{\partial x^i}\int\frac{d^3p}{(2\pi)^2}\frac{\partial f}{\partial E}\hat{p}^i p=0\,. \quad \text{(B.9)}$$

We can neglect the last term of Eq. (B.9) since we only consider first order terms. We define the velocity as

$$v^i=\frac{1}{\rho_{dm}}\int\frac{d^3p}{(2\pi)^2}\,f\,\frac{p\hat{p}^i}{E}\,, \quad \text{(B.10)}$$

where ρ_{dm} is the dark matter density defined as

$$\rho_{dm}=\int\frac{d^3p}{(2\pi)^2}\,f\,. \quad \text{(B.11)}$$

We write Eq. (B.9) in terms of (B.10) and (B.11), to obtain

$$\frac{\partial\rho_{dm}}{dt}+\frac{1}{a}\frac{\partial\rho_{dm}v^i}{dx^i}+3\left[H+\frac{d\Phi}{dt}\right]=0\,. \quad \text{(B.12)}$$

We now expand ρ_{dm}:

$$\rho_{dm}=\rho^0_{dm}[1+\delta(\vec{x},t)]\,, \quad \text{(B.13)}$$

where ρ^0_{dm} is the zero-order term of the density and δ is the overdensity $\delta\rho/\rho$ of cold dark matter. The first-order equation for dark matter finally reads

$$\frac{\partial\delta}{\partial t}+\frac{1}{a}\frac{\partial v^i}{dx^i}+3\frac{d\Phi}{dt}=0\,. \quad \text{(B.14)}$$

We need a second equation (or a second set of equations) since we want to describe the evolution of both δ and v^i: this we can achieve by integrating Eq. (B.8) times $(p/E)\hat{p}^j$ over phase space. Skipping intermediate manipulations, one arrives to the following first-order equation

$$\frac{\partial v^j}{\partial t}+Hv^j+\frac{1}{a}\frac{\partial\Psi}{\partial x^j}=0\,. \quad \text{(B.15)}$$

At this point it useful to introduce the *conformal time* η, which is the maximum comoving distance traveled by a photon during the whole life of the expanding Universe, defined as

$$\eta=\int_0^t\frac{dt'}{a(t')}=\int_0^a\frac{da'}{a'}\frac{1}{a'H(a')}\,. \quad \text{(B.16)}$$

We can finally rewrite (B.14) and (B.15) in terms of the conformal time and the scale factor to obtain the equations which govern the evolution of the density and

the velocity of the cold dark matter. We also Fourier transform them, i.e. we rewrite them in terms of the wavenumber k. They read

$$\dot{\delta} + ikv + 3\Phi = 0 \tag{B.17}$$

$$\dot{v} + \frac{\dot{a}}{a}v + ik\Phi = 0\,, \tag{B.18}$$

where overdots represent derivatives with respect to conformal time η.

***

Bibliography

[1] R. Diamanti, S. Ando, S. Gariazzo, O. Mena and C. Weniger, *Cold dark matter plus not-so-clumpy dark relics*, 1701.03128.

[2] R. Diamanti, M. E. C. Catalan and S. Ando, *Dark matter protohalos in a nine parameter MSSM and implications for direct and indirect detection*, *Phys. Rev.* **D92** (2015) 065029, [1506.01529].

[3] R. Diamanti, L. Lopez-Honorez, O. Mena, S. Palomares-Ruiz and A. C. Vincent, *Constraining Dark Matter Late-Time Energy Injection: Decays and P-Wave Annihilations*, *JCAP* **1402** (2014) 017, [1308.2578].

[4] R. Diamanti, E. Giusarma, O. Mena, M. Archidiacono and A. Melchiorri, *Dark Radiation and interacting scenarios*, *Accepted for publication at Phys. Rev. D* (2012) , [1212.6007].

[5] E. Hubble, *A relation between distance and radial velocity among extra-galactic nebulae*, *Proc.Nat.Acad.Sci.* **15** (1929) 168–173.

[6] Planck collaboration, P. A. R. Ade et al., *Planck 2015 results. XIII. Cosmological parameters*, *Astron. Astrophys.* **594** (2016) A13, [1502.01589].

[7] WMAP Collaboration collaboration, E. Komatsu et al., *Five-Year Wilkinson Microwave Anisotropy Probe (WMAP) Observations: Cosmological Interpretation*, *Astrophys.J.Suppl.* **180** (2009) 330–376, [0803.0547].

[8] J. Lesgourgues and S. Pastor, *Massive neutrinos and cosmology*, *Phys.Rept.* **429** (2006) 307–379, [astro-ph/0603494].

[9] M. S. Turner, G. Steigman and L. M. Krauss, *The Flatness of the Universe: Reconciling Theoretical Prejudices with Observational Data*, *Phys.Rev.Lett.* **52** (1984) 2090–2093.

[10] J. Ostriker and P. J. Steinhardt, *The Observational case for a low density universe with a nonzero cosmological constant*, *Nature* **377** (1995) 600–602.

[11] L. M. Krauss and M. S. Turner, *The Cosmological constant is back*, *Gen.Rel.Grav.* **27** (1995) 1137–1144, [astro-ph/9504003].

[12] R. Jimenez, *The Age of the universe*, astro-ph/9701222.

[13] G. Jungman, M. Kamionkowski and K. Griest, *Supersymmetric dark matter*, *Phys. Rept.* **267** (1996) 195–373, [hep-ph/9506380].

[14] D. Hooper and S. Profumo, *Dark matter and collider phenomenology of universal extra dimensions*, *Phys.Rept.* **453** (2007) 29–115, [hep-ph/0701197].

[15] D. J. Schwarz and S. Hofmann, *Small scale structure of cold dark matter*, *Nucl. Phys. Proc. Suppl.* **87** (2000) 93–95, [astro-ph/9912343].

[16] S. Hofmann, D. J. Schwarz and H. Stoecker, *Damping scales of neutralino cold dark matter*, *Phys. Rev.* **D64** (2001) 083507, [astro-ph/0104173].

[17] E. W. Kolb and M. S. Turner, *The Early Universe*, *Front. Phys.* **69** (1990) 1–547.

[18] A. Sakharov, *Violation of CP Invariance, c Asymmetry, and Baryon Asymmetry of the Universe*, *Pisma Zh.Eksp.Teor.Fiz.* **5** (1967) 32–35.

[19] J. C. Mather, E. S. Cheng, D. A. Cottingham, R. E. Eplee, Jr., D. J. Fixsen, T. Hewagama et al., *Measurement of the cosmic microwave background spectrum by the COBE FIRAS instrument*, *Astrophys. J.* **420** (Jan., 1994) 439–444.

[20] E. Wright, S. Meyer, C. Bennett, N. Boggess, E. Cheng et al., *Interpretation of the Cosmic Microwave Background radiation anisotropy detected by the COBE differential microwave radiometer*, *Astrophys.J.* **396** (1992) L13–L18.

[21] D. J. Fixsen, *The Temperature of the Cosmic Microwave Background*, *Astrophys. J.* **707** (2009) 916–920, [0911.1955].

[22] Particle Data Group collaboration, K. A. Olive et al., *Review of Particle Physics*, *Chin. Phys.* **C38** (2014) 090001.

[23] S. Profumo, K. Sigurdson and M. Kamionkowski, *What mass are the smallest protohalos?*, *Phys. Rev. Lett.* **97** (2006) 031301, [astro-ph/0603373].

[24] T. Bringmann, *Particle Models and the Small-Scale Structure of Dark Matter*, *New J. Phys.* **11** (2009) 105027, [0903.0189].

[25] S. Zaroubi, *The Epoch of Reionization*, 1206.0267.

[26] J. E. Gunn and B. A. Peterson, *On the Density of Neutral Hydrogen in Intergalactic Space*, *Astrophys.J.* **142** (1965) 1633.

[27] Supernova Search Team collaboration, A. G. Riess et al., *Observational evidence from supernovae for an accelerating universe and a cosmological constant*, *Astron. J.* **116** (1998) 1009–1038, [astro-ph/9805201].

[28] Supernova Cosmology Project collaboration, S. Perlmutter et al., *Measurements of Omega and Lambda from 42 high redshift supernovae*, *Astrophys.J.* **517** (1999) 565–586, [astro-ph/9812133].

[29] A. H. Guth, *Inflationary universe: A possible solution to the horizon and flatness problems*, *Phys. Rev. D* **23** (Jan, 1981) 347–356.

[30] A. D. Linde, *A New Inflationary Universe Scenario: A Possible Solution of the Horizon, Flatness, Homogeneity, Isotropy and Primordial Monopole Problems*, *Phys.Lett.* **B108** (1982) 389–393.

[31] A. D. Linde, *Chaotic Inflation*, *Phys.Lett.* **B129** (1983) 177–181.

[32] A. Albrecht and P. J. Steinhardt, *Cosmology for Grand Unified Theories with Radiatively Induced Symmetry Breaking*, *Phys.Rev.Lett.* **48** (1982) 1220–1223.

[33] SDSS collaboration, D. J. Eisenstein et al., *Detection of the baryon acoustic peak in the large-scale correlation function of SDSS luminous red galaxies*, *Astrophys. J.* **633** (2005) 560–574, [astro-ph/0501171].

[34] 2dFGRS collaboration, S. Cole et al., *The 2dF Galaxy Redshift Survey: Power-spectrum analysis of the final dataset and cosmological implications*, *Mon. Not. Roy. Astron. Soc.* **362** (2005) 505–534, [astro-ph/0501174].

[35] F. Beutler, C. Blake, M. Colless, D. H. Jones, L. Staveley-Smith, L. Campbell et al., *The 6dF Galaxy Survey: Baryon Acoustic Oscillations and the Local Hubble Constant*, *Mon. Not. Roy. Astron. Soc.* **416** (2011) 3017–3032, [1106.3366].

[36] C. Blake et al., *The WiggleZ Dark Energy Survey: mapping the distance-redshift relation with baryon acoustic oscillations*, *Mon. Not. Roy. Astron. Soc.* **418** (2011) 1707–1724, [1108.2635].

[37] L. Anderson, E. Aubourg, S. Bailey, D. Bizyaev, M. Blanton et al., *The clustering of galaxies in the SDSS-III Baryon Oscillation Spectroscopic Survey: Baryon Acoustic Oscillations in the Data Release 9 Spectroscopic Galaxy Sample*, 1203.6594.

[38] M. Tegmark, *Doppler peaks and all that: cmb anisotropies and what they can tell us*, astro-ph/9511148.

[39] SDSS collaboration, M. Tegmark et al., *Cosmological parameters from SDSS and WMAP*, *Phys. Rev.* **D69** (2004) 103501, [astro-ph/0310723].

[40] K. G. Begeman, A. H. Broeils and R. H. Sanders, *Extended rotation curves of spiral galaxies: Dark haloes and modified dynamics*, *Mon. Not. Roy. Astron. Soc.* **249** (1991) 523.

[41] R. Narayan and M. Bartelmann, *Lectures on gravitational lensing*, in *13th Jerusalem Winter School in Theoretical Physics: Formation of Structure in the Universe Jerusalem, Israel, 27 December 1995 - 5 January 1996*, 1996. astro-ph/9606001.

[42] D. Clowe, A. Gonzalez and M. Markevitch, *Weak lensing mass reconstruction of the interacting cluster 1E0657-558: Direct evidence for the existence of dark matter*, *Astrophys. J.* **604** (2004) 596–603, [astro-ph/0312273].

[43] D. Clowe, M. Bradac, A. H. Gonzalez, M. Markevitch, S. W. Randall, C. Jones et al., *A direct empirical proof of the existence of dark matter*, *Astrophys. J.* **648** (2006) L109–L113, [astro-ph/0608407].

[44] M. Lindner, T. Ohlsson and G. Seidl, *Seesaw mechanisms for Dirac and Majorana neutrino masses*, *Phys. Rev.* **D65** (2002) 053014, [hep-ph/0109264].

[45] E. K. Akhmedov, G. C. Branco and M. N. Rebelo, *Seesaw mechanism and structure of neutrino mass matrix*, *Phys. Lett.* **B478** (2000) 215–223, [hep-ph/9911364].

[46] A. Boyarsky, O. Ruchayskiy and D. Iakubovskyi, *A Lower bound on the mass of Dark Matter particles*, *JCAP* **0903** (2009) 005, [0808.3902].

[47] U. Seljak, A. Makarov, P. McDonald and H. Trac, *Can sterile neutrinos be the dark matter?*, *Phys. Rev. Lett.* **97** (2006) 191303, [astro-ph/0602430].

[48] J. H. Heo and C. S. Kim, *Light Dark Matter and Dark Radiation*, *J. Korean Phys. Soc.* **68** (2016) 715–721, [1504.00773].

[49] G. Mangano, G. Miele, S. Pastor, T. Pinto, O. Pisanti and P. D. Serpico, *Relic neutrino decoupling including flavor oscillations*, *Nucl. Phys.* **B729** (2005) 221–234, [hep-ph/0506164].

[50] P. F. de Salas and S. Pastor, *Relic neutrino decoupling with flavour oscillations revisited*, *JCAP* **1607** (2016) 051, [1606.06986].

[51] R. H. Cyburt, B. D. Fields, K. A. Olive and T.-H. Yeh, *Big Bang Nucleosynthesis: 2015*, *Rev. Mod. Phys.* **88** (2016) 015004, [1505.01076].

[52] B. D. Fields, P. Molaro and S. Sarkar, *Big-Bang Nucleosynthesis*, *Chin. Phys.* **C38** (2014) , [1412.1408].

[53] G. Steigman, *Neutrinos And Big Bang Nucleosynthesis*, *Adv. High Energy Phys.* **2012** (2012) 268321, [1208.0032].

[54] W. Hu, *Structure formation with generalized dark matter*, *Astrophys. J.* **506** (1998) 485–494, [astro-ph/9801234].

[55] M. Archidiacono, S. Gariazzo, C. Giunti, S. Hannestad, R. Hansen, M. Laveder et al., *PseudoscalarâĂŤsterile neutrino interactions: reconciling the cosmos with neutrino oscillations*, *JCAP* **1608** (2016) 067, [1606.07673].

[56] J. F. Navarro, C. S. Frenk and S. D. M. White, *A Universal density profile from hierarchical clustering*, *Astrophys. J.* **490** (1997) 493–508, [astro-ph/9611107].

[57] J. F. Navarro, C. S. Frenk and S. D. M. White, *The Structure of cold dark matter halos*, *Astrophys. J.* **462** (1996) 563–575, [astro-ph/9508025].

[58] B. Moore, T. R. Quinn, F. Governato, J. Stadel and G. Lake, *Cold collapse and the core catastrophe*, *Mon. Not. Roy. Astron. Soc.* **310** (1999) 1147–1152, [astro-ph/9903164].

[59] M. Cirelli, G. Corcella, A. Hektor, G. Hutsi, M. Kadastik, P. Panci et al., *PPPC 4 DM ID: A Poor Particle Physicist Cookbook for Dark Matter Indirect Detection*, *JCAP* **1103** (2011) 051, [1012.4515].

[60] J. F. Navarro, E. Hayashi, C. Power, A. Jenkins, C. S. Frenk, S. D. M. White et al., *The Inner structure of Lambda-CDM halos 3: Universality and asymptotic slopes*, *Mon. Not. Roy. Astron. Soc.* **349** (2004) 1039, [astro-ph/0311231].

[61] J. F. Navarro, A. Ludlow, V. Springel, J. Wang, M. Vogelsberger, S. D. M. White et al., *The Diversity and Similarity of Cold Dark Matter Halos*, *Mon. Not. Roy. Astron. Soc.* **402** (2010) 21, [0810.1522].

[62] D. S. Reed, S. M. Koushiappas and L. Gao, *Non-universality of halo profiles and implications for dark matter experiments*, *Mon. Not. Roy. Astron. Soc.* **415** (2011) 3177–3188, [1008.1579].

[63] A. A. Dutton and A. V. MacciÃš, *Cold dark matter haloes in the Planck era: evolution of structural parameters for Einasto and NFW profiles*, *Mon. Not. Roy. Astron. Soc.* **441** (2014) 3359–3374, [1402.7073].

[64] D. Merritt, J. F. Navarro, A. Ludlow and A. Jenkins, *A Universal density profile for dark and luminous matter?*, *Astrophys. J.* **624** (2005) L85–L88, [astro-ph/0502515].

[65] J. S. Bullock, T. S. Kolatt, Y. Sigad, R. S. Somerville, A. V. Kravtsov, A. A. Klypin et al., *Profiles of dark haloes. Evolution, scatter, and environment*, *Mon. Not. Roy. Astron. Soc.* **321** (2001) 559–575, [astro-ph/9908159].

[66] F. Prada, A. A. Klypin, A. J. Cuesta, J. E. Betancort-Rijo and J. Primack, *Halo concentrations in the standard LCDM cosmology*, *Mon. Not. Roy. Astron. Soc.* **423** (2012) 3018–3030, [1104.5130].

[67] A. Klypin, S. Trujillo-Gomez and J. Primack, *Halos and galaxies in the standard cosmological model: results from the Bolshoi simulation*, *Astrophys. J.* **740** (2011) 102, [1002.3660].

[68] W. H. Press and P. Schechter, *Formation of Galaxies and Clusters of Galaxies by Self-Similar Gravitational Condensation*, *ApJ* **187** (Feb., 1974) 425–438.

[69] J. R. Bond, S. Cole, G. Efstathiou and N. Kaiser, *Excursion set mass functions for hierarchical Gaussian fluctuations*, *Astrophys. J.* **379** (1991) 440.

[70] J. Diemand, M. Kuhlen and P. Madau, *Formation and evolution of galaxy dark matter halos and their substructure*, *Astrophys. J.* **667** (2007) 859–877, [astro-ph/0703337].

[71] J. Diemand, M. Kuhlen, P. Madau, M. Zemp, B. Moore, D. Potter et al., *Clumps and streams in the local dark matter distribution*, *Nature* **454** (2008) 735–738, [0805.1244].

[72] V. Springel, J. Wang, M. Vogelsberger, A. Ludlow, A. Jenkins, A. Helmi et al., *The Aquarius Project: the subhalos of galactic halos*, *Mon. Not. Roy. Astron. Soc.* **391** (2008) 1685–1711, [0809.0898].

[73] A. A. Dutton, C. Conroy, F. C. v. d. Bosch, F. Prada and S. More, *The Kinematic Connection Between Galaxies and Dark Matter Haloes*, *Mon. Not. Roy. Astron. Soc.* **407** (2010) 2–16, [1004.4626].

[74] G. L. Bryan and M. L. Norman, *Statistical properties of x-ray clusters: Analytic and numerical comparisons*, *Astrophys. J.* **495** (1998) 80, [astro-ph/9710107].

[75] D. G. Cerdeno and A. M. Green, *Direct detection of WIMPs*, 1002.1912.

[76] J. D. Lewin and P. F. Smith, *Review of mathematics, numerical factors, and corrections for dark matter experiments based on elastic nuclear recoil*, *Astropart. Phys.* **6** (1996) 87–112.

[77] J. H. Davis, *The Past and Future of Light Dark Matter Direct Detection*, *Int. J. Mod. Phys.* **A30** (2015) 1530038, [1506.03924].

[78] V. Barger, W.-Y. Keung and G. Shaughnessy, *Spin Dependence of Dark Matter Scattering*, *Phys. Rev.* **D78** (2008) 056007, [0806.1962].

[79] M. Klasen, M. Pohl and G. Sigl, *Indirect and direct search for dark matter*, *Prog. Part. Nucl. Phys.* **85** (2015) 1–32, [1507.03800].

[80] LUX collaboration, D. S. Akerib et al., *Results on the Spin-Dependent Scattering of Weakly Interacting Massive Particles on Nucleons from the Run 3 Data of the LUX Experiment*, *Phys. Rev. Lett.* **116** (2016) 161302, [1602.03489].

[81] R. Bartels and S. Ando, *Boosting the annihilation boost: Tidal effects on dark matter subhalos and consistent luminosity modeling*, *Phys. Rev.* **D92** (2015) 123508, [1507.08656].

[82] D. Anderhalden and J. Diemand, *Density Profiles of CDM Microhalos and their Implications for Annihilation Boost Factors*, *JCAP* **1304** (2013) 009, [1302.0003].

[83] M. Kamionkowski, S. M. Koushiappas and M. Kuhlen, *Galactic Substructure and Dark Matter Annihilation in the Milky Way Halo*, *Phys. Rev.* **D81** (2010) 043532, [1001.3144].

[84] A. M. Green, S. Hofmann and D. J. Schwarz, *The First wimpy halos*, *JCAP* **0508** (2005) 003, [astro-ph/0503387].

[85] A. Loeb and M. Zaldarriaga, *The Small-scale power spectrum of cold dark matter*, *Phys. Rev.* **D71** (2005) 103520, [astro-ph/0504112].

[86] E. Bertschinger, *The Effects of Cold Dark Matter Decoupling and Pair Annihilation on Cosmological Perturbations*, *Phys. Rev.* **D74** (2006) 063509, [astro-ph/0607319].

[87] J. M. Cornell and S. Profumo, *Earthly probes of the smallest dark matter halos*, *JCAP* **1206** (2012) 011, [1203.1100].

[88] P. Gondolo, J. Hisano and K. Kadota, *The Effect of quark interactions on dark matter kinetic decoupling and the mass of the smallest dark halos*, *Phys. Rev.* **D86** (2012) 083523, [1205.1914].

[89] L. E. Strigari, S. M. Koushiappas, J. S. Bullock and M. Kaplinghat, *Precise constraints on the dark matter content of Milky Way dwarf galaxies for gamma-ray experiments*, *Phys. Rev.* **D75** (2007) 083526, [astro-ph/0611925].

[90] M. Kuhlen, J. Diemand and P. Madau, *The Dark Matter Annihilation Signal from Galactic Substructure: Predictions for GLAST*, *Astrophys. J.* **686** (2008) 262, [0805.4416].

[91] G. Bertone, D. Hooper and J. Silk, *Particle dark matter: Evidence, candidates and constraints*, *Phys. Rept.* **405** (2005) 279–390, [hep-ph/0404175].

[92] J. Silk et al., *Particle Dark Matter: Observations, Models and Searches*. 2010.

[93] ATLAS collaboration, G. Aad et al., *Search for new phenomena in final states with an energetic jet and large missing transverse momentum in pp collisions at $\sqrt{s}$ =8 TeV with the ATLAS detector*, *Eur. Phys. J.* **C75** (2015) 299, [1502.01518].

[94] G. Busoni, A. De Simone, E. Morgante and A. Riotto, *On the Validity of the Effective Field Theory for Dark Matter Searches at the LHC*, *Phys. Lett.* **B728** (2014) 412–421, [1307.2253].

[95] BOSS collaboration, L. Anderson et al., *The clustering of galaxies in the SDSS-III Baryon Oscillation Spectroscopic Survey: baryon acoustic oscillations in the Data Releases 10 and 11 Galaxy samples*, *Mon. Not. Roy. Astron. Soc.* **441** (2014) 24–62, [1312.4877].

[96] L. Perivolaropoulos, *Six Puzzles for LCDM Cosmology*, 0811.4684.

[97] T. Shanks, *Problems with the current cosmological paradigm*, *Submitted to: ASP Conf. Ser.* (2004) , [astro-ph/0401409].

[98] M. Boylan-Kolchin, J. S. Bullock and M. Kaplinghat, *The Milky Way's bright satellites as an apparent failure of LCDM*, *Mon. Not. Roy. Astron. Soc.* **422** (2012) 1203–1218, [1111.2048].

[99] A. A. Klypin, A. V. Kravtsov, O. Valenzuela and F. Prada, *Where are the missing Galactic satellites?*, *Astrophys. J.* **522** (1999) 82–92, [astro-ph/9901240].

[100] B. Moore, S. Ghigna, F. Governato, G. Lake, T. R. Quinn, J. Stadel et al., *Dark matter substructure within galactic halos*, *Astrophys. J.* **524** (1999) L19–L22, [astro-ph/9907411].

[101] L. Wang, V. Gonzalez-Perez, L. Xie, A. P. Cooper, C. S. Frenk, L. Gao et al., *The galaxy population in cold and warm dark matter cosmologies*, 1612.04540.

[102] M. R. Lovell, V. Gonzalez-Perez, S. Bose, A. Boyarsky, S. Cole, C. S. Frenk et al., *Addressing the too big to fail problem with baryon physics and sterile neutrino dark matter*, 1611.00005.

[103] A. V. Maccio, O. Ruchayskiy, A. Boyarsky and J. C. Munoz-Cuartas, *The inner structure of haloes in Cold+Warm dark matter models*, *Mon. Not. Roy. Astron. Soc.* **428** (2013) 882–890, [1202.2858].

[104] D. Anderhalden, J. Diemand, G. Bertone, A. V. Maccio and A. Schneider, *The Galactic Halo in Mixed Dark Matter Cosmologies*, *JCAP* **1210** (2012) 047, [1206.3788].

[105] D. Anderhalden, A. Schneider, A. V. Maccio, J. Diemand and G. Bertone, *Hints on the Nature of Dark Matter from the Properties of Milky Way Satellites*, *JCAP* **1303** (2013) 014, [1212.2967].

[106] A. Schneider, R. E. Smith and D. Reed, *Halo Mass Function and the Free Streaming Scale*, *Mon. Not. Roy. Astron. Soc.* **433** (2013) 1573, [1303.0839].

[107] M. R. Lovell, V. Eke, C. S. Frenk, L. Gao, A. Jenkins, T. Theuns et al., *The Haloes of Bright Satellite Galaxies in a Warm Dark Matter Universe*, *Mon. Not. Roy. Astron. Soc.* **420** (2012) 2318–2324, [1104.2929].

[108] M. R. Lovell, C. S. Frenk, V. R. Eke, A. Jenkins, L. Gao and T. Theuns, *The properties of warm dark matter haloes*, *Mon. Not. Roy. Astron. Soc.* **439** (2014) 300–317, [1308.1399].

[109] M. R. Lovell, S. Bose, A. Boyarsky, S. Cole, C. S. Frenk, V. Gonzalez-Perez et al., *Satellite galaxies in semi-analytic models of galaxy formation with sterile neutrino dark matter*, *Mon. Not. Roy. Astron. Soc.* **461** (2016) 60–72, [1511.04078].

[110] G. G. Raffelt, *Astrophysical axion bounds*, *Lect. Notes Phys.* **741** (2008) 51–71, [hep-ph/0611350].

[111] S. Gariazzo, C. Giunti, M. Laveder, Y. F. Li and E. M. Zavanin, *Light sterile neutrinos*, *J. Phys.* **G43** (2016) 033001, [1507.08204].

[112] S. Hannestad, I. Tamborra and T. Tram, *Thermalisation of light sterile neutrinos in the early universe*, *JCAP* **1207** (2012) 025, [1204.5861].

[113] S. Dodelson and L. M. Widrow, *Sterile-neutrinos as dark matter*, *Phys. Rev. Lett.* **72** (1994) 17–20, [hep-ph/9303287].

[114] A. D. Dolgov and S. H. Hansen, *Massive sterile neutrinos as warm dark matter*, *Astropart. Phys.* **16** (2002) 339–344, [hep-ph/0009083].

[115] T. Asaka, M. Laine and M. Shaposhnikov, *Lightest sterile neutrino abundance within the nuMSM*, *JHEP* **01** (2007) 091, [hep-ph/0612182].

[116] A. C. Vincent, E. F. Martinez, P. HernÃąndez, M. Lattanzi and O. Mena, *Revisiting cosmological bounds on sterile neutrinos*, *JCAP* **1504** (2015) 006, [1408.1956].

[117] M. Archidiacono, S. Hannestad, A. Mirizzi, G. Raffelt and Y. Y. Y. Wong, *Axion hot dark matter bounds after Planck*, *JCAP* **1310** (2013) 020, [1307.0615].

[118] E. Di Valentino, S. Gariazzo, M. Gerbino, E. Giusarma and O. Mena, *Dark*

Radiation and Inflationary Freedom after Planck 2015, *Phys. Rev.* **D93** (2016) 083523, [1601.07557].

[119] M. Archidiacono, T. Basse, J. Hamann, S. Hannestad, G. Raffelt and Y. Y. Y. Wong, *Future cosmological sensitivity for hot dark matter axions*, *JCAP* **1505** (2015) 050, [1502.03325].

[120] E. Di Valentino, S. Gariazzo, E. Giusarma and O. Mena, *Robustness of cosmological axion mass limits*, *Phys. Rev.* **D91** (2015) 123505, [1503.00911].

[121] E. Giusarma, E. Di Valentino, M. Lattanzi, A. Melchiorri and O. Mena, *Relic Neutrinos, thermal axions and cosmology in early 2014*, *Phys. Rev.* **D90** (2014) 043507, [1403.4852].

[122] E. Di Valentino, A. Melchiorri and O. Mena, *Dark radiation sterile neutrino candidates after Planck data*, *JCAP* **1311** (2013) 018, [1304.5981].

[123] G. Cowan, *Statistical data analysis*. Oxford University Press, 1998.

[124] G. D'Agostini, *Bayesian reasoning in high-energy physics : principles and applications*, *CERN Yellow Report* **99-03** (1999) .

[125] G. D'Agostini, *Bayesian inference in processing experimental data: Principles and basic applications*, *Rept. Prog. Phys.* **66** (2003) 1383–1420, [physics/0304102].

[126] R. Trotta, *Bayes in the sky: Bayesian inference and model selection in cosmology*, *Contemp. Phys.* **49** (2008) 71–104, [0803.4089].

[127] R. Trotta, *Bayesian Methods in Cosmology*, 2017. 1701.01467.

[128] Planck collaboration, P. A. R. Ade et al., *Planck 2015 results. XV. Gravitational lensing*, *Astron. Astrophys.* **594** (2016) A15, [1502.01591].

[129] Planck collaboration, N. Aghanim et al., *Planck 2015 results. XI. CMB power spectra, likelihoods, and robustness of parameters*, *Astron. Astrophys.* **594** (2016) A11, [1507.02704].

[130] S. Das et al., *The Atacama Cosmology Telescope: temperature and gravitational lensing power spectrum measurements from three seasons of data*, *JCAP* **1404** (2014) 014, [1301.1037].

[131] E. M. George et al., *A measurement of secondary cosmic microwave background anisotropies from the 2500-square-degree SPT-SZ survey*, *Astrophys. J.* **799** (2015) 177, [1408.3161].

[132] B. A. Bassett and R. Hlozek, *Baryon Acoustic Oscillations*, 0910.5224.

[133] Ã. Aubourg et al., *Cosmological implications of baryon acoustic oscillation measurements*, *Phys. Rev.* **D92** (2015) 123516, [1411.1074].

[134] A. J. Ross, L. Samushia, C. Howlett, W. J. Percival, A. Burden and M. Manera, *The clustering of the SDSS DR7 main Galaxy sample âĂŞ I. A 4 per cent distance measure at $z = 0.15$*, *Mon. Not. Roy. Astron. Soc.* **449** (2015) 835–847, [1409.3242].

[135] SDSS collaboration, K. N. Abazajian et al., *The Seventh Data Release of the Sloan Digital Sky Survey*, *Astrophys. J. Suppl.* **182** (2009) 543–558, [0812.0649].

[136] SDSS Collaboration collaboration, C. P. Ahn et al., *The Ninth Data Release of the Sloan Digital Sky Survey: First Spectroscopic Data from the SDSS-III Baryon Oscillation Spectroscopic Survey*, 1207.7137.

[137] W. H. Press and P. Schechter, *Formation of galaxies and clusters of galaxies by selfsimilar gravitational condensation*, *Astrophys. J.* **187** (1974) 425–438.

[138] C. G. Lacey and S. Cole, *Merger rates in hierarchical models of galaxy formation*, *Mon. Not. Roy. Astron. Soc.* **262** (1993) 627–649.

[139] A. R. Zentner, *The Excursion Set Theory of Halo Mass Functions, Halo Clustering, and Halo Growth*, *Int. J. Mod. Phys.* **D16** (2007) 763–816, [astro-ph/0611454].

[140] R. Barkana, Z. Haiman and J. P. Ostriker, *Constraints on warm dark matter from cosmological reionization*, *Astrophys. J.* **558** (2001) 482, [astro-ph/0102304].

[141] A. J. Benson, A. Farahi, S. Cole, L. A. Moustakas, A. Jenkins, M. Lovell et al., *Dark Matter Halo Merger Histories Beyond Cold Dark Matter: I - Methods and Application to Warm Dark Matter*, *Mon. Not. Roy. Astron. Soc.* **428** (2013) 1774, [1209.3018].

[142] O. Hahn and A. Paranjape, *The locations of halo formation and the peaks formalism*, *Mon. Not. Roy. Astron. Soc.* **438** (2014) 878–899, [1308.4142].

[143] A. Schneider, *Structure formation with suppressed small-scale perturbations*, *Mon. Not. Roy. Astron. Soc.* **451** (2015) 3117–3130, [1412.2133].

[144] A. Schneider, *Astrophysical constraints on resonantly produced sterile neutrino dark matter*, *JCAP* **1604** (2016) 059, [1601.07553].

[145] C. Giocoli, L. Pieri, G. Tormen and J. Moreno, *A Merger Tree with Microsolar Mass Resolution: Application to γ-ray Emission from Subhalo Population*, *Mon. Not. Roy. Astron. Soc.* **395** (2009) 1620–1630, [0811.2426].

[146] E. Polisensky and M. Ricotti, *Constraints on the Dark Matter Particle Mass from the Number of Milky Way Satellites*, *Phys. Rev.* **D83** (2011) 043506, [1004.1459].

[147] J. Lesgourgues, *The Cosmic Linear Anisotropy Solving System (CLASS) I: Overview*, 1104.2932.

[148] B. Audren, J. Lesgourgues, K. Benabed and S. Prunet, *Conservative Constraints on Early Cosmology: an illustration of the Monte Python cosmological parameter inference code*, *JCAP* **1302** (2013) 001, [1210.7183].

[149] F. Feroz and M. P. Hobson, *Multimodal nested sampling: an efficient and robust alternative to MCMC methods for astronomical data analysis*, *Mon. Not. Roy. Astron. Soc.* **384** (2008) 449, [0704.3704].

[150] F. Feroz, M. P. Hobson and M. Bridges, *MultiNest: an efficient and robust Bayesian inference tool for cosmology and particle physics*, *Mon. Not. Roy. Astron. Soc.* **398** (2009) 1601–1614, [0809.3437].

[151] F. Feroz, M. P. Hobson, E. Cameron and A. N. Pettitt, *Importance Nested Sampling and the MultiNest Algorithm*, 1306.2144.

[152] J. Buchner, A. Georgakakis, K. Nandra, L. Hsu, C. Rangel, M. Brightman et al., *X-ray spectral modelling of the AGN obscuring region in the CDFS: Bayesian model selection and catalogue*, *Astron. Astrophys.* **564** (2014) A125, [1402.0004].

[153] A. Boyarsky, J. Lesgourgues, O. Ruchayskiy and M. Viel, *Lyman-alpha constraints on warm and on warm-plus-cold dark matter models*, *JCAP* **0905** (2009) 012, [0812.0010].

[154] A. Palazzo, D. Cumberbatch, A. Slosar and J. Silk, *Sterile neutrinos as subdominant warm dark matter*, *Phys. Rev.* **D76** (2007) 103511, [0707.1495].

[155] V. Poulin, P. D. Serpico and J. Lesgourgues, *A fresh look at linear cosmological constraints on a decaying dark matter component*, *JCAP* **1608** (2016) 036, [1606.02073].

[156] S. P. Martin, *A Supersymmetry primer*, hep-ph/9709356.

[157] H. E. Haber, "PDG Review of Susy (Theory)."

[158] P. d. J. O. Buchmueller, "PDG Review of Susy (Experiment)."

[159] M. Cabrera, J. Casas and A. Delgado, *Upper Bounds on Superpartner Masses from Upper Bounds on the Higgs Boson Mass*, *Phys.Rev.Lett.* **108** (2012) 021802, [1108.3867].

[160] G. F. Giudice and A. Strumia, *Probing High-Scale and Split Supersymmetry with Higgs Mass Measurements*, *Nucl.Phys.* **B858** (2012) 63–83, [1108.6077].

[161] J. A. Casas, J. M. Moreno, S. Robles, K. Rolbiecki and B. Zaldivar, *What is a Natural SUSY scenario?*, 1407.6966.

[162] U. Ellwanger, C. Hugonie and A. M. Teixeira, *The Next-to-Minimal Supersymmetric Standard Model*, *Phys.Rept.* **496** (2010) 1–77, [0910.1785].

[163] R. Barbieri, L. J. Hall, Y. Nomura and V. S. Rychkov, *Supersymmetry without a Light Higgs Boson*, *Phys.Rev.* **D75** (2007) 035007, [hep-ph/0607332].

[164] P. Batra, A. Delgado, D. E. Kaplan and T. M. Tait, *The Higgs mass bound in gauge extensions of the minimal supersymmetric standard model*, *JHEP* **0402** (2004) 043, [hep-ph/0309149].

[165] A. Brignole, J. Casas, J. Espinosa and I. Navarro, *Low scale supersymmetry breaking: Effective description, electroweak breaking and phenomenology*, *Nucl.Phys.* **B666** (2003) 105–143, [hep-ph/0301121].

[166] T. Goerdt, O. Y. Gnedin, B. Moore, J. Diemand and J. Stadel, *The survival and disruption of CDM micro-haloes: Implications for direct and indirect detection experiments*, *Mon.Not.Roy.Astron.Soc.* **375** (2007) 191–198, [astro-ph/0608495].

[167] A. Arbey, M. Battaglia, A. Djouadi, F. Mahmoudi and J. Quevillon, *Implications of a 125 GeV Higgs for supersymmetric models*, *Phys.Lett.* **B708** (2012) 162–169, [1112.3028].

[168] N. Polonsky and A. Pomarol, *GUT effects in the soft supersymmetry breaking terms*, *Phys.Rev.Lett.* **73** (1994) 2292–2295, [hep-ph/9406224].

[169] ATLAS collaboration, G. Aad et al., *Search for squarks and gluinos with the ATLAS detector in final states with jets and missing transverse momentum using $\sqrt{s} = 8$ TeV proton–proton collision data*, *JHEP* **1409** (2014) 176, [1405.7875].

[170] CMS collaboration, C. Collaboration, *Search for supersymmetry in hadronic final states using MT2 with the CMS detector at sqrt(s) = 8 TeV*, .

[171] C. Strege, G. Bertone, G. J. Besjes, S. Caron, R. Ruiz de Austri, A. Strubig et al., *Profile likelihood maps of a 15-dimensional MSSM*, *JHEP* **09** (2014) 081, [1405.0622].

[172] MasterCode collaboration, K. J. de Vries, *SUSY fits with full LHC Run I data*, in *International Conference on High Energy Physics 2014 (ICHEP 2014) Valencia, Spain, July 2-9, 2014*, 2014. 1410.6755.

[173] K. J. de Vries et al., *The pMSSM10 after LHC Run 1*, 1504.03260.

[174] E. A. Bagnaschi et al., *Supersymmetric Dark Matter after LHC Run 1*, 1508.01173.

[175] P. Grothaus, M. Lindner and Y. Takanishi, *Naturalness of Neutralino Dark Matter*, *JHEP* **1307** (2013) 094, [1207.4434].

[176] C. Cheung, L. J. Hall, D. Pinner and J. T. Ruderman, *Prospects and Blind Spots for Neutralino Dark Matter*, *JHEP* **1305** (2013) 100, [1211.4873].

[177] S. S. AbdusSalam, B. C. Allanach, F. Quevedo, F. Feroz and M. Hobson, *Fitting the Phenomenological MSSM*, *Phys.Rev.* **D81** (2010) 095012, [0904.2548].

[178] S. S. AbdusSalam, *Stop-mass prediction in naturalness scenarios within MSSM-25*, *Int. J. Mod. Phys.* **A29** (2014) 1450160, [1312.7830].

[179] S. S. AbdusSalam, C. P. Burgess and F. Quevedo, *MFV Reductions of MSSM Parameter Space*, *JHEP* **02** (2015) 073, [1411.1663].

[180] J. D. Etienne Auge and J. T. T. Van, *Proceedings of Rencontres de Moriond on QCD and High Energy Interactions*, .

[181] Particle Data Group collaboration, W. Yao et al., *Review of Particle Physics*, *J.Phys.* **G33** (2006) 1–1232.

[182] K. Hagiwara, A. Martin, D. Nomura and T. Teubner, *Improved predictions for g-2 of the muon and alpha(QED) (M**2(Z))*, *Phys.Lett.* **B649** (2007) 173–179, [hep-ph/0611102].

[183] M. E. Cabrera, A. Casas, R. R. de Austri and G. Bertone, *LHC and dark matter phenomenology of the NUGHM*, 1311.7152.

[184] "The LEP Electroweak Working Group." http://lepewwg.web.cern.ch/LEPEWWG.

[185] Heavy Flavor Averaging Group collaboration, Y. Amhis et al., *Averages of B-Hadron, C-Hadron, and tau-lepton properties as of early 2012*, 1207.1158.

[186] LHCb collaboration, R. Aaij et al., *Measurement of the $B_s^0 - \bar{B}_s^0$ oscillation frequency Δm_s in $B_s^0 \to D_s^-(3)\pi$ decays*, *Phys.Lett.* **B709** (2012) 177–184, [1112.4311].

[187] BaBar Collaboration collaboration, B. Aubert et al.*Phys.Rev.Lett.* **100** (2008) 021801, [0709.1698].

[188] FlaviaNet Working Group on Kaon Decays collaboration, M. Antonelli et al., *Precision tests of the Standard Model with leptonic and semileptonic kaon decays*, 0801.1817.

[189] LHCb Collaboration collaboration, R. Aaij et al., *First Evidence for the Decay $B_s^0 \to \mu^+\mu^-$*, *Phys.Rev.Lett.* **110** (2013) 021801, [1211.2674].

[190] Heavy Flavor Averaging Group (HFAG) collaboration, Y. Amhis et al., *Averages of b-hadron, c-hadron, and τ-lepton properties as of summer 2014*, 1412.7515.

[191] Belle collaboration, T. Saito et al., *Measurement of the $\bar{B} \to X\_s\gamma$ Branching Fraction with a Sum of Exclusive Decays*, *Phys. Rev.* **D91** (2015) 052004, [1411.7198].

[192] BaBar collaboration, J. P. Lees et al., *Exclusive Measurements of $b \to s\gamma$ Transition Rate and Photon Energy Spectrum*, *Phys. Rev.* **D86** (2012) 052012, [1207.2520].

[193] LHCb, CMS collaboration, V. Khachatryan et al., *Observation of the rare $B^0\_s \to \mu^+\mu^-$ decay from the combined analysis of CMS and LHCb data*, *Nature* **522** (2015) 68–72, [1411.4413].

[194] ATLAS Collaboration collaboration, G. Aad et al., *Observation of a new particle in the search for the Standard Model Higgs boson with the ATLAS detector at the LHC*, *Phys.Lett.* **B716** (2012) 1–29, [1207.7214].

[195] CMS Collaboration collaboration, S. Chatrchyan et al., *Observation of a new boson at a mass of 125 GeV with the CMS experiment at the LHC*, *Phys.Lett.* **B716** (2012) 30–61, [1207.7235].

[196] XENON100 Collaboration collaboration, E. Aprile et al., *Dark Matter Results from 225 Live Days of XENON100 Data*, *Phys.Rev.Lett.* **109** (2012) 181301, [1207.5988].

[197] Planck collaboration, P. Ade et al., *Planck 2013 results. XVI. Cosmological parameters*, *Astron.Astrophys.* **571** (2014) A16, [1303.5076].

[198] G. Bertone, D. G. Cerdeno, M. Fornasa, R. R. de Austri and R. Trotta, *Identification of Dark Matter particles with LHC and direct detection data*, *Phys.Rev.* **D82** (2010) 055008, [1005.4280].

[199] *http://lepewwg.web.cern.ch/LEPEWWG*.

[200] Heavy Flavor Averaging Group collaboration, Y. Amhis et al., *Averages of b-hadron, c-hadron, and tau-lepton properties as of early 2012*, 1207.1158.

[201] BABAR collaboration, B. Aubert et al., *Measurement of Branching Fractions and CP and Isospin Asymmetries in $B \to K^*\gamma$*, 0808.1915.

[202] Planck collaboration, P. Ade et al., *Planck 2013 results. XVI. Cosmological parameters*, *Astron.Astrophys.* **571** (2014) A16, [1303.5076].

[203] R. R. de Austri, R. Trotta and L. Roszkowski, *A Markov chain Monte Carlo analysis of the CMSSM*, *JHEP* **0605** (2006) 002, [hep-ph/0602028].

[204] XENON100 collaboration, E. Aprile et al., *Dark Matter Results from 225 Live Days of XENON100 Data*, *Phys.Rev.Lett.* **109** (2012) 181301, [1207.5988].

[205] XENON100 collaboration, E. Aprile et al., *Limits on spin-dependent WIMP-nucleon cross sections from 225 live days of XENON100 data*, *Phys. Rev. Lett.* **111** (2013) 021301, [1301.6620].

[206] XENON100 collaboration, E. Aprile et al., *XENON100 Dark Matter Results from a Combination of 477 Live Days*, *Phys. Rev.* **D94** (2016) 122001, [1609.06154].

[207] B. Allanach, *SOFTSUSY: a program for calculating supersymmetric spectra*, *Comput.Phys.Commun.* **143** (2002) 305–331, [hep-ph/0104145].

[208] G. Belanger, F. Boudjema, A. Pukhov and A. Semenov, *MicrOMEGAs: A Program for calculating the relic density in the MSSM*, *Comput.Phys.Commun.* **149** (2002) 103–120, [hep-ph/0112278].

[209] P. Gondolo, J. Edsjo, L. Bergstrom, P. Ullio and E. A. Baltz, *DarkSUSY: A Numerical package for dark matter calculations in the MSSM*, astro-ph/0012234.

[210] J. R. Ellis, K. A. Olive and C. Savage, *Hadronic Uncertainties in the Elastic Scattering of Supersymmetric Dark Matter*, *Phys.Rev.* **D77** (2008) 065026, [0801.3656].

[211] G. Degrassi, P. Gambino and P. Slavich, *SusyBSG: A Fortran code for BR[B -¿ X(s) gamma] in the MSSM with Minimal Flavor Violation*, *Comput.Phys.Commun.* **179** (2008) 759–771, [0712.3265].

[212] F. Mahmoudi, *SuperIso v2.3: A Program for calculating flavor physics observables in Supersymmetry*, *Comput.Phys.Commun.* **180** (2009) 1579–1613, [0808.3144].

[213] A. Sommerfeld, *Annalen der Physik*, *Annalen der Physik* **403** (1931) 257.

[214] J. Hisano, S. Matsumoto, M. Nagai, O. Saito and M. Senami, *Non-perturbative*

effect on thermal relic abundance of dark matter, *AIP Conf.Proc.* **957** (2007) 401–404.

[215] T. R. Slatyer, *The Sommerfeld enhancement for dark matter with an excited state*, *JCAP* **1002** (2010) 028, [0910.5713].

[216] S. Cassel, *Sommerfeld factor for arbitrary partial wave processes*, *J.Phys.* **G37** (2010) 105009, [0903.5307].

[217] R. Iengo, *Sommerfeld enhancement: General results from field theory diagrams*, *JHEP* **0905** (2009) 024, [0902.0688].

[218] L. Visinelli and P. Gondolo, *An integral equation for distorted wave amplitudes*, 1007.2903.

[219] A. Hryczuk, R. Iengo and P. Ullio, *Relic densities including Sommerfeld enhancements in the MSSM*, *JHEP* **1103** (2011) 069, [1010.2172].

[220] A. Hryczuk, *The Sommerfeld enhancement for scalar particles and application to sfermion co-annihilation regions*, *Phys.Lett.* **B699** (2011) 271–275, [1102.4295].

[221] A. M. Green, S. Hofmann and D. J. Schwarz, *The power spectrum of SUSY - CDM on sub-galactic scales*, *Mon.Not.Roy.Astron.Soc.* **353** (2004) L23, [astro-ph/0309621].

[222] A. M. Green and S. P. Goodwin, *On mini-halo encounters with stars*, *Mon.Not.Roy.Astron.Soc.* **375** (2007) 1111–1120, [astro-ph/0604142].

[223] S. Hofmann, D. Schwarz and H. Stoecker, *Formation of small-scale structure in SUSY CDM*, astro-ph/0211325.

[224] V. Berezinsky, V. Dokuchaev and Y. Eroshenko, *Small - scale clumps in the galactic halo and dark matter annihilation*, *Phys.Rev.* **D68** (2003) 103003, [astro-ph/0301551].

[225] N. Arkani-Hamed, A. Delgado and G. Giudice, *The Well-tempered neutralino*, *Nucl.Phys.* **B741** (2006) 108–130, [hep-ph/0601041].

[226] "LHC SUSY Cross Section Working Group." https://twiki.cern.ch/twiki/bin/view/LHCPhysics/SUSYCrossSections#SUSY_Cross_Sections_using_8_TeV.

[227] T. Sjostrand, S. Mrenna and P. Z. Skands, *PYTHIA 6.4 Physics and Manual*, *JHEP* **0605** (2006) 026, [hep-ph/0603175].

[228] T. Sjostrand, S. Mrenna and P. Z. Skands, *A Brief Introduction to PYTHIA 8.1*, *Comput.Phys.Commun.* **178** (2008) 852–867, [0710.3820].

[229] ATLAS collaboration, G. Aad et al., *Measurements of the Higgs boson production and decay rates and coupling strengths using pp collision data at $\sqrt{s} = 7$ and 8 TeV in the ATLAS experiment*, 1507.04548.

[230] ATLAS, CMS collaboration, G. Aad et al., *Measurements of the Higgs boson production and decay rates and constraints on its couplings from a combined ATLAS and CMS analysis of the LHC pp collision data at $\sqrt{s} = 7$ and 8 TeV*, *JHEP* **08** (2016) 045, [1606.02266].

[231] A. Djouadi, M. Muhlleitner and M. Spira, *Decays of supersymmetric particles: The Program SUSY-HIT (SUspect-SdecaY-Hdecay-InTerface)*, *Acta Phys.Polon.* **B38** (2007) 635–644, [hep-ph/0609292].

[232] ATLAS collaboration, G. Aad et al., *Search for direct top-squark pair production in final states with two leptons in pp collisions at $\sqrt{s} = 8$TeV with the ATLAS detector*, *JHEP* **1406** (2014) 124, [1403.4853].

[233] ATLAS collaboration, G. Aad et al., *Search for direct pair production of the top squark in all-hadronic final states in proton-proton collisions at $\sqrt{s} = 8$ TeV with the ATLAS detector*, *JHEP* **1409** (2014) 015, [1406.1122].

[234] ATLAS collaboration, G. Aad et al., *Search for pair-produced third-generation squarks decaying via charm quarks or in compressed supersymmetric scenarios in pp collisions at $\sqrt{s} = 8$ TeV with the ATLAS detector*, *Phys.Rev.* **D90** (2014) 052008, [1407.0608].

[235] ATLAS collaboration, G. Aad et al., *Search for strong production of supersymmetric particles in final states with missing transverse momentum and at least three b-jets at $\sqrt{s}$= 8 TeV proton-proton collisions with the ATLAS detector*, *JHEP* **1410** (2014) 24, [1407.0600].

[236] ATLAS collaboration, G. Aad et al., *Search for direct production of charginos, neutralinos and sleptons in final states with two leptons and missing transverse momentum in pp collisions at $\sqrt{s} = 8$ TeV with the ATLAS detector*, *JHEP* **1405** (2014) 071, [1403.5294].

[237] J. Edsjo, *Aspects of neutrino detection of neutralino dark matter*, hep-ph/9704384.

[238] ATLAS collaboration, G. Aad et al., *Summary of the searches for squarks and gluinos using $\sqrt{s} = 8$ TeV pp collisions with the ATLAS experiment at the LHC*, 1507.05525.

[239] K. Griest and D. Seckel, *Three exceptions in the calculation of relic abundances*, *Phys.Rev.* **D43** (1991) 3191–3203.

[240] P. Cushman, C. Galbiati, D. McKinsey, H. Robertson, T. Tait et al., *Working Group Report: WIMP Dark Matter Direct Detection*, 1310.8327.

[241] D. Malling, D. Akerib, H. Araujo, X. Bai, S. Bedikian et al., *After LUX: The LZ Program*, 1110.0103.

[242] LUX Collaboration collaboration, D. Akerib et al., *First results from the LUX dark matter experiment at the Sanford Underground Research Facility*, 1310.8214.

[243] LUX collaboration, D. S. Akerib et al., *Results from a search for dark matter in the complete LUX exposure*, *Phys. Rev. Lett.* **118** (2017) 021303, [1608.07648].

[244] S. R. Golwala, *Exclusion limits on the WIMP nucleon elastic scattering cross-section from the Cryogenic Dark Matter Search*, .

[245] R. J. Hill and M. P. Solon, *WIMP-nucleon scattering with heavy WIMP effective theory*, *Phys.Rev.Lett.* **112** (2014) 211602, [1309.4092].

[246] R. J. Hill and M. P. Solon, *Standard Model anatomy of WIMP dark matter direct detection II: QCD analysis and hadronic matrix elements*, *Phys.Rev.* **D91** (2015) 043505, [1409.8290].

[247] J. Diemand, M. Kuhlen and P. Madau, *Dark matter substructure and gamma-ray annihilation in the Milky Way halo*, *Astrophys.J.* **657** (2007) 262–270, [astro-ph/0611370].

[248] J. F. Navarro, C. S. Frenk and S. D. White, *Simulations of x-ray clusters*, *Mon.Not.Roy.Astron.Soc.* **275** (1995) 720–740, [astro-ph/9408069].

[249] S. Ando, *Gamma-ray background anisotropy from galactic dark matter substructure*, *Phys.Rev.* **D80** (2009) 023520, [0903.4685].

[250] T. Cohen, M. Lisanti, A. Pierce and T. R. Slatyer, *Wino Dark Matter Under Siege*, *JCAP* **1310** (2013) 061, [1307.4082].

[251] J. Fan and M. Reece, *In Wino Veritas? Indirect Searches Shed Light on Neutralino Dark Matter*, *JHEP* **1310** (2013) 124, [1307.4400].

[252] A. Hryczuk, I. Cholis, R. Iengo, M. Tavakoli and P. Ullio, *Indirect Detection Analysis: Wino Dark Matter Case Study*, 1401.6212.

[253] M. E. C. Catalan, S. Ando, C. Weniger and F. Zandanel, *Indirect and direct detection prospect for TeV dark matter in the MSSM-9*, 1503.00599.

[254] S. Ambrosanio and B. Mele, *Supersymmetric scenarios with dominant radiative neutralino decay*, *Phys.Rev.* **D55** (1997) 1399–1417, [hep-ph/9609212].

[255] M. A. Diaz, B. Panes and P. Urrejola, *Radiative Neutralino Decay in Split Supersymmetry*, *Eur.Phys.J.* **C67** (2010) 181–190, [0910.1554].

[256] N. Desai, J. Ellis, F. Luo and J. Marrouche, *Closing in on the Tip of the CMSSM Stau Coannihilation Strip*, *Phys.Rev.* **D90** (2014) 055031, [1404.5061].

[257] S. P. Martin, *Exploring compressed supersymmetry with same-sign top quarks at the Large Hadron Collider*, *Phys.Rev.* **D78** (2008) 055019, [0807.2820].

[258] S. Bornhauser, M. Drees, S. Grab and J. Kim, *Light Stop Searches at the LHC in Events with two b-Jets and Missing Energy*, *Phys.Rev.* **D83** (2011) 035008, [1011.5508].

[259] A. Delgado, G. F. Giudice, G. Isidori, M. Pierini and A. Strumia, *The light stop window*, *Eur.Phys.J.* **C73** (2013) 2370, [1212.6847].

[260] P. Coles and F. Lucchin, *Cosmology: The Origin and evolution of cosmic structure*, .

[261] S. Dodelson, *Modern Cosmology*. Academic Press, Amsterdam, 2003.

Acknowledgements

Me gustaría agredecer a todas las personas que me han apoyado en la realización de esta tesis. Antes de todo, muchas gracias a mis co-directores, por haberme enseñado a entender como se hace investigación, no obstante las "dificultades" encontradas durante ese camino. Gracias a Shin'ichiro y a Christoph, quienes creyeron que podía salir adelante con mi proyecto y desearon mi éxito final. Gracias también a María, por haberme guiado, enseñado y ayudado al principio. Gracias a todos ellos por su enorme paciencia, sobre todo al final de mi doctorado.

Gracias también a mi director Jan de Boer y a todos los miembros de mi tribunal por su atento trabajo en la lectura de mi tesis.

Querría agradecer a Gianfranco Bertone, por sus indispensables y amables consejos que me han guiado durante todo este tiempo.

Gracias a todo mi grupo, a todo el GRAPPA. Gracias a mis compañeros de despacho: Hamish, Michael, Sebastian, Niki, Richard, Thomas y Suraj. Niki querida, muchísimas gracias por ayudarme en la traducción del resumen de la tesis. Gracias también a Richard por ello. Sois maravillosos! Un gracias de corazón lo doy a Hamish, Michael y Sebastian, por no haberme dejado nunca, nunca y nunca sola, y por haberme enseñado un montón sobre estadística y computación. Gracias a Michael, por su perpetuo cariño y paciencia conmigo, especialmente cuando yo empecé y hablaba un inglés rudimentario: nunca olvidaré los esfuerzos que hizo en hablar en español conmigo. Hamish, que bien que ha estado compartir casa contigo! Aunque yo era la mayor, y tu hermana me agradeció haberte "cuidado", yo sigo sosteniendo que eres tú el que me ha "baby-sitted" todo el tiempo! Moltes gràcies!!

Un grazie enorme alle segretarie dell'istituto di fisica: Natalie ed Anne-Marieke. In particolare voglio ringraziare Natalie per avermi accolta e sostenuta sempre con tutta la gentilezza e la grande professionalità che la caratterizzano.

Un grazie di cuore ai miei collaboratori "esterni": Olga e Stefano. Olga è sempre stata una guida importante per me, coinvolgendomi e facendomi sempre sentire importante, anche grazie al suo inesauribile entusiasmo per la fisica. Conosciuto alla scuola ISAAP 2014 a Belgirate, Stefano è prima di tutto un amico meraviglioso, della cui amicizia mi sento fortunata, poi collega e scienziato eccezionale che, (mooolto) pazientemente, mi ha insegnato tanto, tanto e tanto. Grazie per avermi sempre sostenuta. Mi sento profondamente debitrice con voi.
Voglio ringraziare con tutto il cuore Miguel Escudero: grazie Miguel per avermi sempre sostenuto con la persona bellissima che sei, con tutta la tua genialità e con tutta la passione per fisica.

No instituto conheci uma das pessoas que defino fantástica: Francesca Calore. Ela tem sido para mim muito boa amiga e uma boa conselheira. Aprecio a paciência muito grande que ela teve comigo e nunca esqueço o tempo que passamos juntas, especialmente quando vivíamos no mesmo apartamento. Foi uma das lembranças que eu guardarei em o meu coração para sempre. Obrigada a Francesco (agora seu marido), obrigada a vocês "Franceschi", por todos os bons momentos passados juntos! Graças a eles que conheci Alessandro Mirizzi, uma pessoa muito bonita que me ajudou muito no meu trabalho. Foi fantàstico ter periodicamente e-mails com ele (e não apenas sobre fisica!)

In questi anni ho fatto parecchie conoscenze, alcune delle quali sono state significative sia dal punto di vista scientifico che dal punto di vista umano. Voglio ringraziare in particolare un amico-collaboratore dal quale ho imparato "un monton" sulla dark matter: Sergio Palomares. Grazie per la sua grande pazienza nel rispondere alle mie infinite domande di fisica, tutte le volte che facevo capolino a Lisbona. È grazie a Sergio che ho conosciuto Nicolás Bernal, che ringrazio tantissimo per tutte le sue spiegazioni e bei momenti trascorsi in quel di Lisbona, e poi Ángeles, allora sua dottoranda, ed attualmente un'eccezionale "investigatora" di Astroparticelle a Lisbona. Ángeles è stata per me un'amica incredibile prima di tutto, e poi - come l'ho sempre definita - "l'Oracolo di Delphi" della fisica! Gracias por todo tu apoyo, paciencia y cariño conmigo Angie querida!

I want to thank all my family: my Papino and my Mammina (who always has lovely encouraged me to move on and never give up). Thanks to my brother Marco, who has always been a brilliant example to follow. Thanks to him and his wonderful family: the beautiful and "cuddly" new entry in our family, Viola, and her smart and beautiful mum, Lucrezia. Thanks a lot to my grandma Gianna, and thanks a lot, a lot to my aunt Anna, whose advices were for me rays of sunshine and positivity. Thanks to my cousin Andrea.

Voglio ringraziare tutti i miei amici che mi hanno sostenuto durante tutti questi anni. Vorrei prima di tutto ringraziare la mia migliore amica Loredana che, nonostante la lontananza, mi è sempre stata vicina. Grazie Lory che hai sempre creduto in me. Grazie ad Enrico (a breve suo marito).
Grazie infinite alla coppia più bella dell'Universo: Ilaria ed Antonio. In particolare, ringrazio di cuore Ilaria: la sua gioia perpetua e la sua positività mi hanno guidato tutti i giorni di questo percorso.

Grazie di cuore a Lalletta&Luchino, il loro sostegno ed energia sono stati per me il carburante per andare avanti anche nei momenti meno "soft".
Muito obrigada a Edo e Stefy (Edo, muito obrigada por ter sempre acreditado em mim). Obrigada ao meu "Gemellino" Dario e ao meu querido amigo Danilo (Jimbo). Obrigada a todos vocês, pelo vosso amàvel apoio.
Gracias a Giulietta, quien sempre ha sido un punto de referencia para mí. Gracias a Danielone quien sempre ha creido en mí (definiéndome una buena "darkmattara"). Gracias a Valerietto e Stefania por vuestro amable apoyo. Gracias a Francesca A., cuyas palabras y consejos llevo siempre dentro de mi corazón. Gracias a Valerione, a Andrea L., a Cecilietta, a Tommaso. Gracias a mi querida amiga Federica. Gracias a todos vosotros que me habéis dado siempre la fuerza con vuestras sonrisas.

Grazie infinite ai miei bellissimi, simpaticissimi, in "gambissimi" e (soprattutto) pazientissimi coinquilini Antonio e Lorenzo. Antonio, grazie per la pazienza che hai avuto con me, e per le chiacchierate super interessanti, in quel della cucina, sui massimi sistemi di economia. Grazie a Lorenzo che, da ottimo "particellaro", mi ha sempre aiutato quando ne avevo bisogno (nulla togliendo alla sua infinita pazienza). Grazie ragazzi!!

Gracias a toda la familia Nebot: a Mariángeles, a Fernando, a Cuca y Sergio el pequeñito, a Ruth (con la cual he pasado unos días maravillosos aquí en Amsterdam), a Fernan, a Isabel, a Miguelito, a María, a la Yaya Nieves, a tía Mariajosé, a Mandi y a Carla. Mil gracias por vuestro cariño.

Finalment, però no menys important, vull agrair a la persona a la qual aquesta tesi s'ha dedicat: la meva estrella, el meu llum que sempre m'ha guiat, tots els dies de la meva vida. Ell és el la cosa més bella que he tingut en la meva vida. Ell és el meu amor Miguel. Gràcies per estar sempre amb mi. Gràcies pel teu Amor incondicional.

Ao, se me so dimenticata de qualcuno, abbiate pazienza, è che nun je la faccio più. D'artronde, so' du' ore che sto seduta a scrive 'sti ringraziamenti! Che, per carità, me fa piacere, ma s'è fatta 'na certa e c'ho voja de andamme a fa' du' passi, visto che mo è uscito pure er sole.

Arigatou Gozaimasu!